nature physics

Article

https://doi.org/10.1038/s41567-023-02271-5

Size-dependent transition from steady contraction to waves in actomyosin networks with turnover

Received: 13 July 2022

Accepted: 25 September 2023

Published online: 3 January 2024

Check for updates

Ashwini Krishna[1], Mariya Savinov[2], Niv Ierushalmi[1], Alex Mogilner[2,3] & Kinneret Keren[1,4]

Actomyosin networks play essential roles in many cellular processes, including intracellular transport, cell division and cell motility, and exhibit many spatiotemporal patterns. Despite extensive research, how the interplay between network mechanics, turnover and geometry leads to these different patterns is not well understood. We focus on the size-dependent behaviour of contracting actomyosin networks in the presence of turnover, using a reconstituted system based on cell extracts encapsulated in water-in-oil droplets. We show that the system can self-organize into different global contraction patterns, exhibiting persistent contractile flows in smaller droplets and periodic contractions in the form of waves or spirals in larger droplets. The transition between continuous and periodic contraction occurs at a characteristic length scale that is inversely dependent on the network contraction rate. These dynamics are captured by a theoretical model that considers the coexistence of different local density-dependent mechanical states with distinct rheological properties. The model shows how large-scale contractile behaviours emerge from the interplay between network percolation, which is essential for long-range force transmission, and rearrangements due to advection and turnover. Our findings thus demonstrate how varied contraction patterns can arise from the same microscopic constituents, without invoking specific biochemical regulation, merely by changing the system geometry.

Active networks composed of actin filaments and motor proteins are ubiquitous in cells, displaying a rich spectrum of dynamic behaviours (reviewed in refs. 1–3). In general, actomyosin networks have a clear bias towards contraction[4,5], which can be local or extend throughout the system with sustained or pulsatile temporal dynamics (for example, refs. 6–10). These diverse contractile patterns play a central role in driving the dynamic behaviours of living cells and tissues[3,5], often exhibiting abrupt transitions along the cell cycle or during development (for example, refs. 6–8). Despite extensive research, the respective roles of the intrinsic self-organized dynamics of the actomyosin cytoskeleton versus upstream regulation by various signalling pathways (for example, Rho GTPases) in shaping these large-scale patterns and the transitions between them often remain unclear[11].

[1]Department of Physics, Technion – Israel Institute of Technology, Haifa, Israel. [2]Courant Institute of Mathematical Sciences, New York University, New York, NY, USA. [3]Department of Biology, New York University, New York, NY, USA. [4]Network Biology Research Laboratories and Russell Berrie Nanotechnology Institute, Technion – Israel Institute of Technology, Haifa, Israel. e-mail: mogilner@cims.nyu.edu; kinneret@physics.technion.ac.il

In vitro realizations of systems containing actin filaments, crosslinkers and myosin motors have been instrumental for uncovering the properties of actomyosin networks and relating their large-scale dynamics to the underlying molecular composition[12–16]. Most of the work on reconstituted actomyosin networks has focused on systems with limited turnover, in which contraction is typically a 'one-shot' process[12–16]. Extensive work has shown that the contractile behaviour in these systems is primarily dependent on two effective parameters: the network connectivity and motor activity[12,13,17,18]. The structure and connectivity of the network are crucial for long-range transmission of the motor-generated forces and, hence, dramatically influence the stress distribution within the network. Moreover, these forces generate flows and modulate the network structure. This feedback between force generation and network architecture can generate different large-scale behaviours including contracting states and quiescent states in which the motor-generated forces are balanced by the rigidity of the network[18].

The introduction of continuous turnover, with rapid actin assembly and disassembly, in addition to motor activity, further complicates the interplay between network architecture and force generation, facilitating a richer spectrum of dynamic behaviours[19–21]. Importantly, actomyosin networks in vivo are typically characterized by rapid turnover rates, which can be two orders of magnitude higher than the turnover rates of purified actin filaments, thanks to a host of auxiliary proteins involved in stimulating debranching, filament severing and depolymerization[22]. Theoretical work indicates that the presence of continuous turnover makes contraction more sustainable[19–21], facilitating large-scale connectivity and force transmission even when the network is continuously flowing and rupturing. This can lead to a steady state of contraction[23], but under some conditions, pulsatile contractions are also predicted[19]. Despite their importance, our understanding of the behaviour of actomyosin networks with rapid turnover is still rather limited. In particular, what determines the characteristic length scales for contraction (local versus global contraction) as well as its temporal dynamics (continuous versus pulsatile) in the presence of turnover is still not well understood.

In this Article, we study the contractile behaviour of bulk actomyosin networks with rapid turnover using a reconstituted system based on cell extracts[23–26]. Previous work has shown that bulk actomyosin networks can exhibit a steady state of contraction in the presence of turnover[23] or periodic contraction in the form of large-scale waves[27–30], but what determines the observed mode of contraction remained unclear. Our reconstituted system enables us to explore the behaviour of actomyosin networks across a wide range of conditions and geometries, and we show that these two apparently distinct modes of global contraction can arise from the same microscopic constituents and interactions, merely by changing the system size. We find that for different biochemical compositions, the system generically exhibits a transition from continuous contraction in smaller cells to periodic contraction in the form of waves or spirals in larger cells. The characteristic length scale for this transition varies between the different conditions and increases in conditions exhibiting slower contraction.

The size-dependent transition from continuous to periodic contraction, which we observe under various conditions, was not predicted by any of the previous theoretical models or agent-based simulations[19–21,23,31,32]. To account for this phenomenology, we, thus, propose a new theoretical model that considers the interplay between the network percolation required for long-range force transmission and the advection due to the contractile flows driven by the motor-generated forces. Within this model, we take into account the heterogeneities that develop in the system due to network assembly, disassembly and advection, and we consider the coexistence of different density-dependent mechanical states with distinct rheological properties in different regions of the system. The contractile behaviour emerges from the self-organized dynamics of these coexisting local mechanical states. Importantly, the rapid rates of actin turnover allow the system to efficiently bridge disjoint network regions and contract globally even when the contraction initiates locally. We show that our model accounts for the observed size-dependent transition in the contraction patterns, with a steady-state continuous contraction predicted in smaller systems and periodic contractions developing when the system size exceeds a threshold. Altogether, our experimental and theoretical results show how elaborate self-organized spatiotemporal patterns can emerge from the interplay between network structure, internal force generation and geometry, without necessitating additional regulation through specific signalling processes.

Contraction patterns in actin networks with rapid turnover

Contracting actin networks are generated in cell-like compartments by encapsulating cytoplasmic *Xenopus* egg extract in water-in-oil emulsion droplets[23–26,29,33]. The extract contains actin as well as crosslinking proteins and myosin II motors[34], which have been shown to drive network contraction[13,25,28]. Due to the rapid actin turnover rates (~1 min^{-1})[23,25], the system can sustain contracting network flows for hours. Interestingly, we observed two qualitatively different patterns of global contraction: (1) continuous contraction and (2) pulsatile, periodic contraction (Fig. 1 and Supplementary Video 1). In the continuous regime, observed in smaller droplets, the system was essentially in a steady state, as previously reported[23]. In this case, the network exhibited a smooth density distribution that decreased towards the droplet periphery and a radial velocity profile in which the inward network flow speed increased linearly as a function of the distance from the contraction centre (Fig. 1a and Supplementary Video 2)[23]. In the pulsatile regime, observed in larger droplets, the system exhibited a periodic variation in the form of concentric waves in both network density and flow speed (Fig. 1c and Supplementary Video 3)[27–29]. Wavefronts of higher actin density appeared regularly near the periphery of the droplet and contracted inward towards the contraction centre (where an aggregate of cellular debris formed, whose size scaled with the size of the droplet[23,29]) (Extended Data Fig. 1).

The shape of the contracting wavefronts reflects the shape of the boundaries of the system[28]; for example, circular wavefronts formed in round pancake-shaped droplets (Fig. 1c and Supplementary Video 3), whereas in elongated channels, the wavefronts were straight and parallel to the channel walls (Extended Data Fig. 2a–c and Supplementary Video 4). In spherical droplets, the contracting wavefronts formed concentric spherical shells (Extended Data Fig. 2d and Supplementary Video 5). The pulsatile contractions had a characteristic time period of ~1 min, as is evident in the radial kymographs of the network density and velocity (Fig. 1d). We observed qualitatively similar behaviour in different extract batches, but quantitatively there was some variation (for example, in wave period and the contraction rate) between different extracts and also depending on the extract concentration used (60–100%; Methods).

Global, periodic contractions to a single contraction centre were observed, even when the system size became macroscopic (Supplementary Video 6), as previously reported[27,28]. What maintains the efficient recycling of network components in this case? Although in smaller droplets diffusive transport can be sufficient, in larger droplets, diffusion would be prohibitively slow, resulting in the accumulation of network components at the centre due to the continuous inward convection by the contracting network. A potential mechanism for enhancing the outward recycling of network components is centrifugal fluid flow[15,35–37]. To study fluid-mediated transport in the system, we introduced 0.5-µm-diameter fluorescent beads, which were sufficiently small not to be permanently trapped by the contracting network yet large enough so that they could be followed by single particle tracking. We observed coherent non-diffusive bead movements directed both inwards and outwards (Extended Data Fig. 3 and Supplementary Video 7).

https://doi.org/10.1038/s41567-023-02271-5

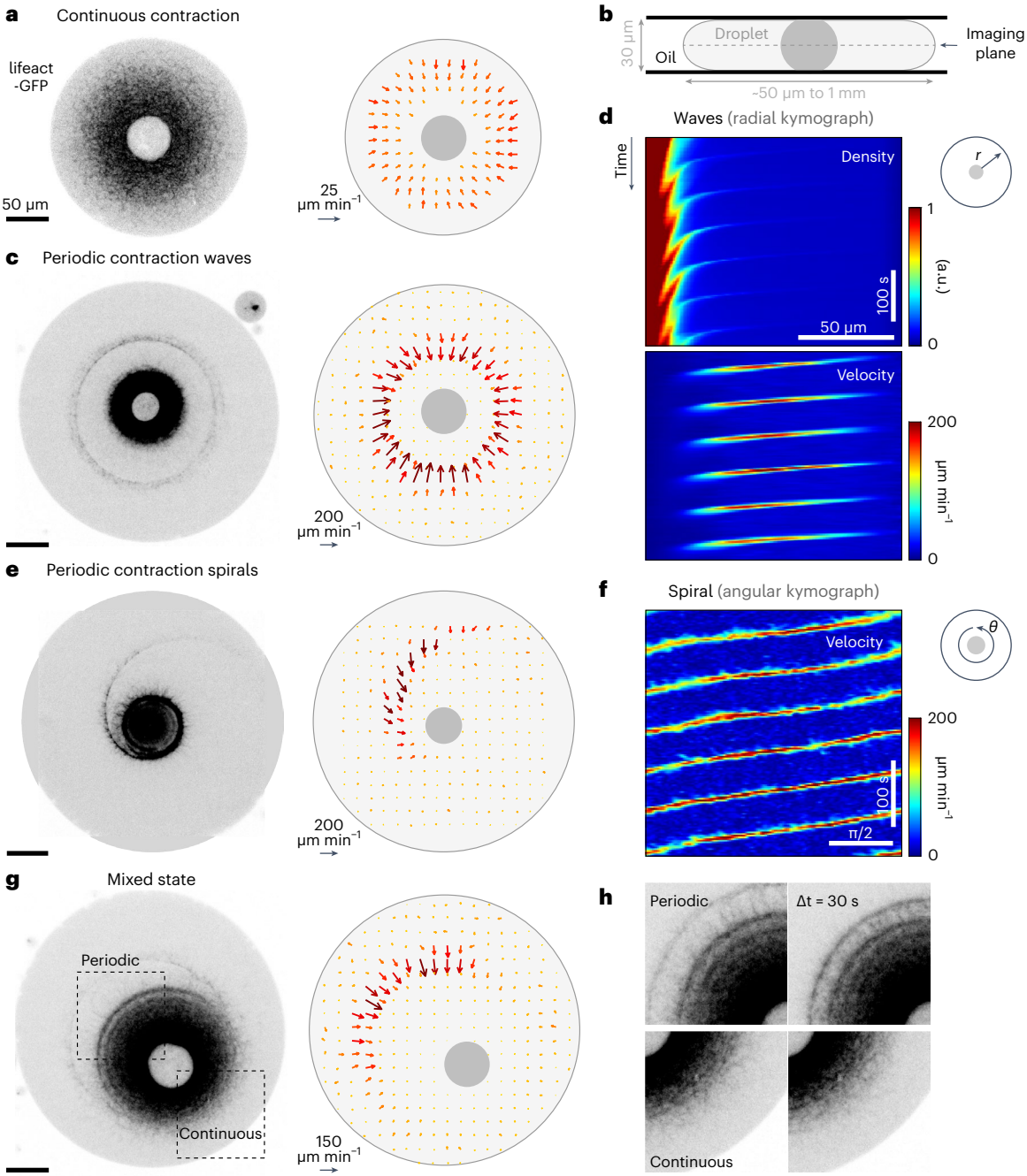

Fig. 1 | Examples of continuous and periodic contraction patterns in actin networks with rapid turnover. a,**c**, Spinning-disc confocal images (left; inverted contrast) and the corresponding velocity fields extracted using optical flow (right; Methods) of water-in-oil droplets exhibiting continuous contraction (**a**; Supplementary Video 2) or periodic contraction in the form of concentric waves (**c**; Supplementary Video 3). **b**, The droplets are sandwiched between two coverslips in a pancake-like geometry, and the images are taken at the droplet midplane (Methods). The solid grey disc at the middle of the droplet represents an aggregate of particulates, which forms an exclusion zone around the contraction centre[23]. **d**, Radial kymographs showing the periodic variation in density (top) and network flow velocity (bottom) over time in the droplet shown in **c**. **e**, Spinning-disc confocal image (left) and the corresponding velocity field (right) of a water-in-oil droplet exhibiting periodic contraction in the form of a clockwise spiral (Supplementary Video 8). **f**, Kymograph showing the angular variation in velocity over time for the spiral shown in **e**. The linearly varying phase of the spiral wavefront as a function of angle generates periodically spaced parallel diagonal lines in the angular kymograph. **g**, Spinning-disc confocal image (left) and the corresponding velocity field (right) of a water-in-oil droplet in which the contraction centre is off-centre. The actin network exhibits different contractile behaviours in different regions of the droplet (Supplementary Video 9). **h**, Subsequent images from different regions of the droplet shown in **g** depicting the contraction of a wavefront on the far side of the droplet (upper left box in **g**) and continuous contraction on the opposite side (lower right box in **g**). The droplets shown contain 95–98% *Xenopus* cell extract supplemented with lifeact-GFP to visualize the actin network (Methods).

The inward-moving beads appeared to be transiently trapped within the network, being found at higher density near the crest of wavefronts where the network density was higher and moving radially inwards with the same velocity as the contracting network. Interestingly, we observed inward bead movements even in regions where the actin network density was low and comparable to the background signal levels, for example near the droplet periphery and in between wavefronts, indicating that there was a connected network that was flowing there even though we were unable to directly detect the network there. Importantly, we also observed transient waves of collective outward bead motion, with comparable speeds, which we believe reflect the motion of the cytosolic fluid phase (Extended Data Fig. 3). The outward fluid flow exhibited the same periodicity as the contracting network (Extended Data Fig. 3c), suggesting that the fluid flow was driven by the contraction of the porous actin network[37]. Such an outward fluid flow could promote efficient large-scale transport of network components even in larger droplets. Additional details on the interpretation of the bead-tracking experiments can be found in Supplementary Information.

Interestingly, the periodic contractions can also take the form of spirals (Fig. 1e and Supplementary Video 8). In this case, the local network density and velocity exhibited periodic modulations, as with circular concentric waves, but the wavefront formed a spiral. The contractile flow was primarily directed inwards, but there was also a non-zero tangential component along the spiral wavefront (Fig. 1e). We observed spirals rotating both clockwise and anticlockwise with similar probabilities (Extended Data Fig. 4), suggesting that the chiral patterns arose from spontaneous angular symmetry breaking. The spirals could be stable for multiple rotations (Fig. 1f), but occasionally we observed transitions between concentric waves and spirals (Extended Data Fig. 4c,d). The transition into a spiral was typically preceded by an angular variation in the network density distribution that persisted at the same location over multiple consecutive wave periods (Extended Data Fig. 4d). These spontaneous angular variations appeared sufficient for driving the transition between the two types of periodic contraction patterns, namely concentric waves and spirals.

The continuous and periodic contraction regimes were sometimes observed together within a single droplet in which the contraction centre was located asymmetrically (Fig. 1g and Supplementary Video 9). In such cases, the periodic contractions occurred on the side of the droplet where the distance between the contraction centre and the droplet periphery reached a maximum, whereas the continuous contraction was apparent on the opposite side (Fig. 1h). These observations indicate that the pulsatile contractions in larger droplets were not caused by the scaling of biochemical concentrations with droplet size, but rather that the transition between continuous and periodic contraction behaviour directly depended on the system geometry, specifically on the distance between the boundary of the system and the contraction centre.

Transition from continuous to periodic contraction

To characterize the size-dependent transition between continuous and periodic contraction, we observed droplets of different sizes (which naturally formed in the emulsion-generating process) and assessed their global contractile behaviour by looking for periodic density modulations in the radial kymographs (Fig. 2a and Methods). The properties of the reconstituted actomyosin networks could be modulated by adding different components of the actin machinery or pharmacological drugs that modified their activity[23]. Interestingly, although the network appearance and properties changed substantially, we observed a qualitatively similar transition from a continuous contraction in smaller droplets to periodic contractions in larger droplets under a range of conditions (Fig. 2 and Supplementary Video 10). The characteristic length scale for the transition from continuous to periodic contraction, however, shifted depending on the system composition (Fig. 2b,d). All comparative analyses between different conditions were done with the same batch of extract, but qualitatively the observed trends were similar in different extracts. For our standard conditions (80% extract), the characteristic length scale for the transition between continuous and periodic contraction was ~150 μm (Methods). Enhancing actin assembly by adding nucleation-promoting factors, such as mDia1, which nucleates unbranched actin filaments, or ActA, which activates the Arp2/3 complex to nucleate branched actin filaments, decreased the contraction rate[23] and shifted the transition length to larger values (Fig. 2b,d,e). Conversely, adding capping protein, which caps growing actin filaments, increased the contraction rate[23] and shifted the transition length to smaller values. Within the periodic regime, the wave period varied between different conditions (Fig. 2c,g) but did not have a strong dependence on system size (Fig. 2c; see also ref. 29). The concentrations of added proteins were chosen to have an appreciable effect on the dynamics of the network and were comparable to the endogenous concentrations of these actin-related proteins in the extract[34].

We have previously shown that in the continuous contracting regime, the network undergoes telescopic contraction with nearly homogeneous, density-independent contraction[23]. As such, the contraction of these spatially inhomogeneous networks can be characterized by a single characteristic contraction rate. Although this contraction rate is an emerging property of the system that depends in a non-trivial manner on the internal force generation and architecture of the network, as well as on the system size (Extended Data Fig. 5), it can nonetheless be measured in a straightforward manner from the slope of the radial velocity profile (Fig. 2e inset). Interestingly, we found that for the different conditions examined, the transition length was inversely correlated with the contraction rate (Fig. 2f).

The characteristic time period in the periodic regime also varied between different conditions but did not appear to be correlated with the contraction rate (Fig. 2e,g). Notably, the wave period was of the same order of magnitude as the duration of the actin turnover cycle in the system (~1 min; ref. 23). We hypothesize that the wave period is primarily dependent on the actin assembly dynamics. To test this idea, we introduced a high concentration of phalloidin, which is a small actin filament-binding molecule that stabilizes filamentous actin and prevents its disassembly (Fig. 3a,b). In the presence of 20 μM of phalloidin (a concentration comparable to that of the actin subunits in the system[34]), the amount of actin monomers available for assembly was expected to gradually decrease (as phalloidin binds essentially irreversibly to filaments and sequesters more and more actin subunits), leading to a slowing down of actin assembly. Indeed, initially, we observed pulsatile contractions in larger droplets as we did in samples with a rapid turnover. However, over time, the intensity of the wavefronts diminished, until eventually the contraction died out and all the filamentous actin accumulated around the contraction centre (Fig. 3a,b and Supplementary Video 11), illustrating the importance of actin turnover for persistent contraction. Similar behaviour has been observed in a reconstituted actomyosin network with limited turnover[15]. Importantly, we observed that the time period between subsequent wavefronts increased whereas the rate of contraction remained similar (Fig. 3b), indicating that the period depended primarily on the actin assembly rates. Overall, these observations indicate that although the quantitative characteristics of the transition from continuous to periodic contraction vary depending on the system properties, the appearance of such a transition is a generic, self-organized feature of contracting actin networks that does not depend on any fine-tuning of the system parameters but crucially depends on the continuous network turnover.

The nature of the transition between continuous and periodic contraction can be visualized by following individual droplets over extended timescales. The extract is a complex mixture of components,

https://doi.org/10.1038/s41567-023-02271-5

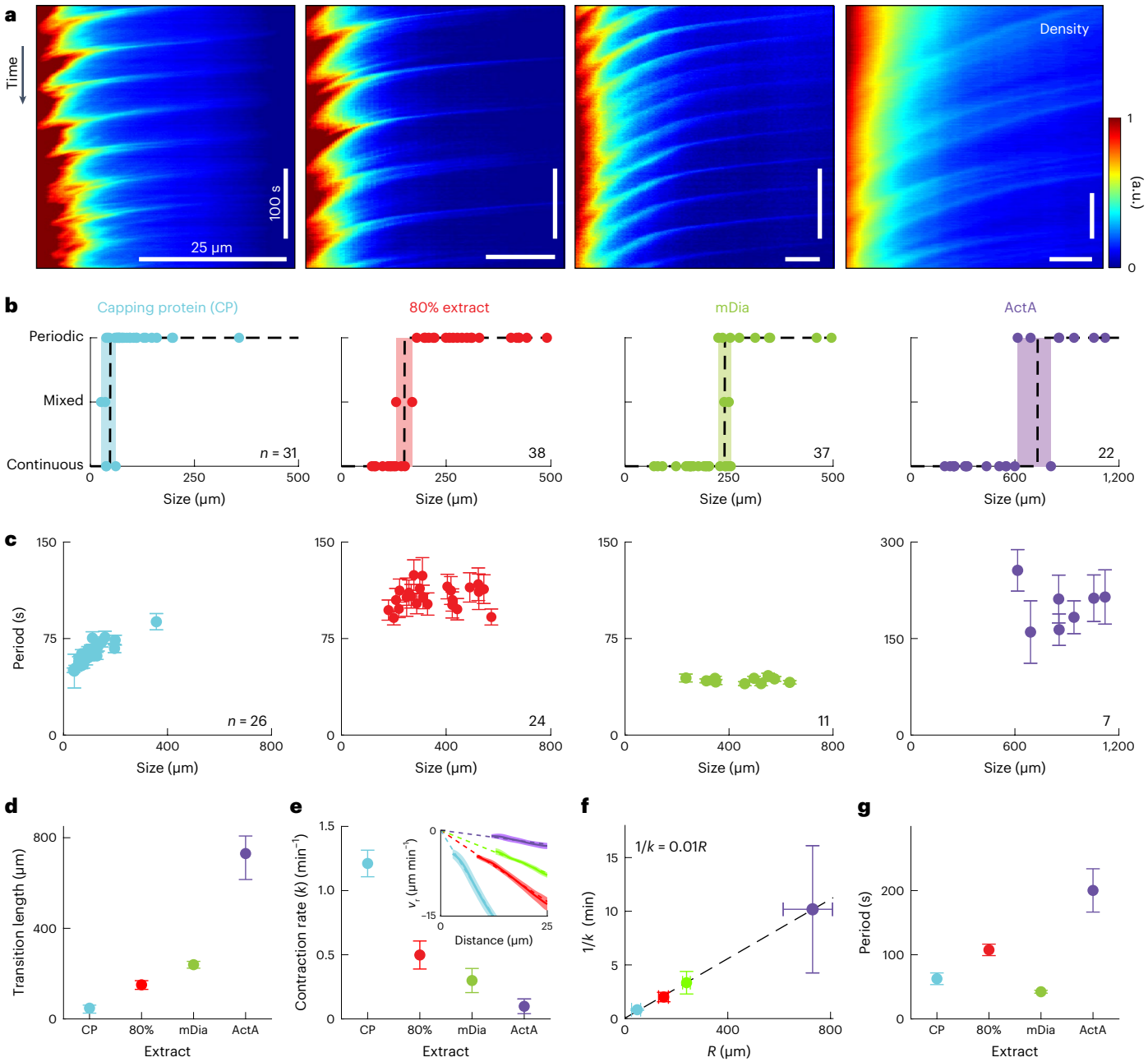

Fig. 2 | Transition from continuous to periodic contraction depends on system size and contraction rate. a, Radial kymographs showing the periodic variation in network density over time for droplets with different compositions (Supplementary Video 10). The droplets contain 80% *Xenopus* cell extract supplemented with lifeact-GFP to visualize the actin network and auxiliary proteins, from left to right: 1 µM capping protein, none, 0.5 µM mDia or 1.5 µM ActA. **b**, The global contractile behaviour of droplets with different compositions was determined as a function of the distance between the contraction centre and the droplet boundary. For each condition, large droplets exhibit periodic contractions, small droplets exhibit continuous contraction and the transition length varies as indicated (dashed line). The shaded region corresponds to the range between the smallest droplet exhibiting periodic behaviour and the largest droplet showing continuous contraction. **c**, Graphs depicting the wave period as a function of size for populations of droplets above the transition length for the different compositions (as in **a**). The error bars indicate the uncertainty in determining the wave period in each droplet (defined as the width of the best-fitting Gaussian to the peak in the Fourier spectrum; Methods). **d**, Transition length estimated from the data shown in **b** for the different compositions. The error bars depict the width of the shaded region in **b**. **e**, The contraction rate in the continuous regime for the different compositions. The contraction rate was measured in small droplets ($R < 70$ µm) from the slope of the radial velocity (v_r) as a function of distance from the contraction centre[23] (Inset; Methods). Error bars and shaded regions in the inset depict the standard deviation (std) between droplets. **f**, Inverse contraction rate plotted as a function of the transition length for the different conditions (data and error bars from **d** and **e**). The line depicts a linear fit. **g**, The mean wave period ± std for a population of droplets in the periodic regime for the different conditions (data from **c**). $n = 31, 38, 37$ or 22 in **b** and **d**; $n = 26, 24, 11$ or 7 in **c** and **g**; and $n = 7, 7, 5$ and 5 in **e** for samples with capping protein, none, mDia or ActA, respectively.

which can evolve over time. We typically observed a slow upwards drift in the contraction rate over time that was more pronounced in some extracts. Although the source of this time-dependent behaviour was not characterized well, we could nevertheless harness this gradual variation in system properties to follow the transition between continuous and periodic contraction and characterize the onset of periodic contraction in a single droplet (Fig. 3c,d and Supplementary Video 12). As the contraction rate increased over time (Fig. 3d, right), the

https://doi.org/10.1038/s41567-023-02271-5

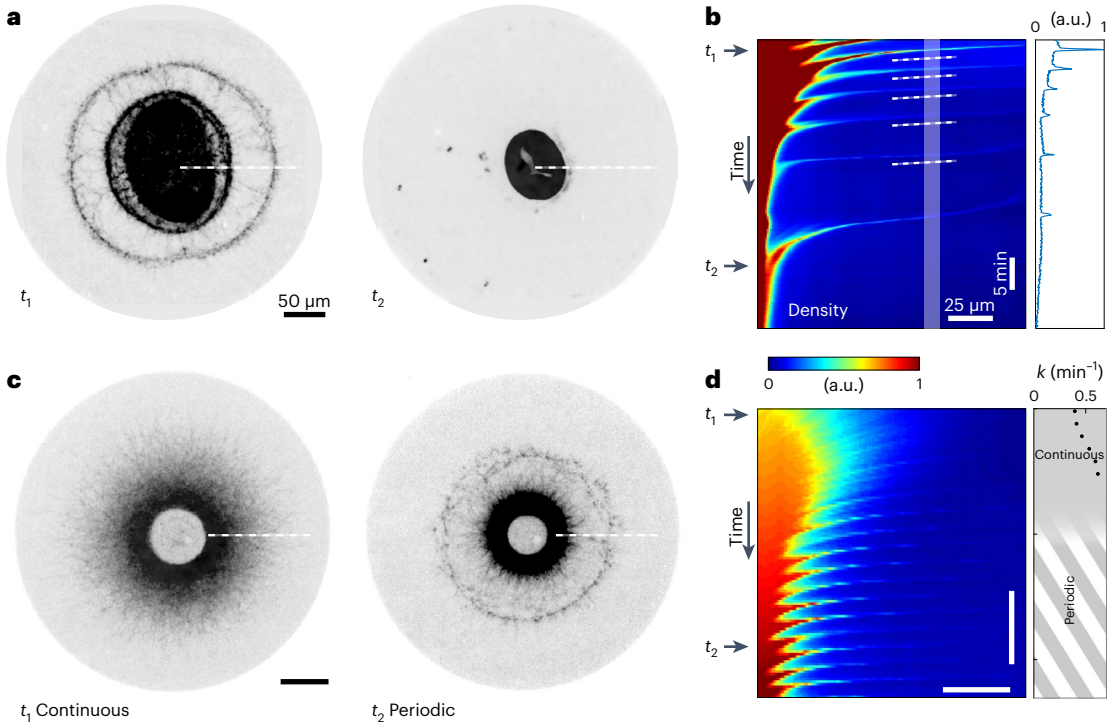

Fig. 3 | Dynamics of droplets with changing actin turnover or contraction rates. a, Spinning-disc confocal images of a droplet containing 85% *Xenopus* cell extract supplemented with 20 μM phalloidin to limit actin turnover (Methods). The droplet exhibits several waves of contraction (left) until eventually most of the filamentous actin accumulates around the contraction centre (right; Supplementary Video 11). **b**, Radial kymograph showing the network density over time for the droplet shown in **a**. Multiple wavefronts separated by increasing time intervals can be seen contracting inwards with similar rates. The dashed lines denote the mean wavefront velocity. Right, network density along the vertical shaded region in the kymograph plotted over time showing the decrease in the intensity of subsequent wavefronts. **c**, Spinning-disc confocal images of a droplet exhibiting a transition from continuous contraction (left) to periodic contractions (right). The droplet contains 98% *Xenopus* cell extract and was imaged over 25 min, during which time the contractile behaviour of the droplet changed gradually (Supplementary Video 12). **d**, Radial kymograph showing the variation in density over time for the droplet shown in **c**. Right, the increasing contraction rate in the continuous regime is plotted as a function of time. The appearance of periodic modulations in the density is indicated. The arrows in **b** and **d** indicate the time points corresponding to the images shown in **a** and **c**, respectively, and the dashed lines in **a** and **c** depict the range of the radial kymographs.

characteristic transition length to the periodic regime decreased, in agreement with our observations with varying system composition (Fig. 2b). As a result, individual droplets that were initially just below the transition length and exhibited continuous contraction changed their global contractile behaviour and transitioned into the periodic regime (Fig. 3c,d). Over time, the continuous network flow first broke into short intermittent arcs that were not synchronized well in space or time. These local modulations became more spatially synchronized, turning into well-defined wavefronts that increased in amplitude as the system moved further away from the transition point.

Modelling contraction of actomyosin networks with turnover

To understand the observed contractile behaviours and how the system can switch from continuous contraction to periodic waves, we turn to theoretical modelling. The simplest description of a dynamic contractile actomyosin network, as introduced in ref. 23, posits that the network assembles and disassembles, behaving effectively as a highly viscous fluid on long timescales, with an active contractile (myosin-powered) stress that drives network contraction against its internal viscous resistance. Although this simple model can account for the continuous steady-state contraction observed in smaller droplets[23], it cannot generate periodic contractions.

An obvious limitation of this simple formulation is that both the contractile stress and the effective network viscosity are assumed to be finite for any density. Previous work has shown that contractions in actomyosin networks occur only above a minimal threshold for network connectivity and motor activity[12,13], implying that the network behaviour at low densities must be qualitatively different. Theoretically, this transition has been described in terms of percolation models that consider network connectivity and its interplay with motor activity (reviewed in ref. 18): the network must be connected (percolated) for myosin motors to generate long-range contractile forces and at the same time, the motor activity modulates the network structure. With continuous actin turnover, this picture must be further modified to include the effects of network disassembly and reassembly and advection generated by persistent network flows.

Here we introduce density dependencies of the contractility and viscosity into the active fluid model and consider the coexistence of different local mechanical regimes. At low filament density, the network is not percolated, and hence, we assume that its effective viscosity will be negligible and that force propagation in space is limited. Taking this into account, qualitatively, waves could arise through cycles of contraction and gelation as previously suggested[27,28]: after a contractile wave sweeps the network inwards, unconnected filaments and network fragments reassemble at the droplet periphery. After some time, a new wave is triggered when the local density increases beyond the contraction threshold. To generate periodic global waves in this scenario, one must assume that there is also an intermediate regime where the network is percolated but not yet contractile. Consider the wake of a contracting front. As the unconnected network reassembles, the density will first reach the contraction threshold near the periphery and furthest from the previous wavefront (since the network there had the longest time to reassemble). When this happens, the nascent network in the middle

(between the centre and the periphery) must be percolated to provide a mechanical connection between the network near the boundary and the previous wavefront.

The presence of an interconnected network between subsequent wavefronts is supported by our experiment with tracer beads, which were observed to move centripetally inwards, even in the low-density regions between wavefronts (Extended Data Fig. 3). There is also a possibility that a contractile shell develops near the periphery and contracts inwards due to the contribution of tangential stresses along the curved wavefront, without a direct mechanical connection to the centre[29]. However, this contractile shell mechanism would not explain the contraction of flat wavefronts as found in the one-dimensional (1D) capillaries (Extended Data Fig. 2a–c), which is why we focus the discussion below on the former mechanism. Nevertheless, in Supplementary Information, we consider the contractile shell model and show that it explains several features of the data. Notably, in two dimensions (2D) or three dimensions (3D), these two mechanisms are not mutually exclusive; rather, it is likely that the contractile behaviour in higher dimensions arises from a combination of the contraction of the curved wavefronts inwards and their mechanical link to the contraction centre (see Supplementary Information for details).

The cyclic gelation-contraction mechanism also provides an intuitive explanation for the observed size-dependence of the transition from continuous to periodic contraction. Since the contractile network elements are connected in series, their contractions add up across the droplet, so the contractile flow at the periphery increases with droplet size. In smaller droplets, the inward flow at the periphery is slow enough for assembly to replenish the receding network continuously. In larger droplets, however, the inward flow wipes out the network so rapidly that a finite period of reassembly (without flow) is necessary before another cycle of contraction can initiate. Note that this intuitive explanation for the size-dependent contractile behaviour is also relevant for the contractile shell model; in fact, it works for any model that displays telescopic contraction coupled with a finite network assembly rate.

To test this picture, one needs simulations of a quantitative model. We based our model on the previously suggested state diagram for actomyosin networks (reviewed in ref. 18), with some notable differences (Fig. 4a). That state diagram[18], depicted as a function of two parameters—network connectivity (an effective measure that depends on network density, filament lengths, as well as the concentration and properties of crosslinking proteins) and motor activity—includes four states: an unconnected 'gas', a percolated but non-contracting network, a globally contracting network and a locally contracting network. It is reasonable to assume that the connectivity is an increasing function of actin density, whereas the motor activity is an increasing function of myosin density. We, thus, employed a simplified state diagram that depends on a single network density field (assuming that both actin and myosin densities are proportional to this network density) and considered three density-dependent mechanical regimes (Fig. 4a): (I) a 'gas-like' state with unconnected network fragments, (II) a connected but not contracting state and (III) a contracting state. The fourth local contraction regime emerges as a small-scale instability in our model (see below).

Importantly, the state diagram in ref. 18 is for networks with negligible turnover that are primarily elastic with an irreversible contraction from an initial state. The network turnover induces qualitative changes and allows connected network clusters to dynamically form and break, implying that the network must fluidize at long timescales (compared to the turnover timescale). Moreover, the different mechanical regimes can coexist in different regions of the system, and the boundaries between these regions can be dynamic over time. We, thus, rely on the different mechanical states identified previously, but, in contrast to previous work, we assume that the network is primarily viscous on the long timescales considered. (We argue in Supplementary Information that a purely elastic 2D or 3D network would be incompatible with our data.) Most importantly, we examine how the three mechanical regimes play out dynamically in space and time in the presence of continuous network turnover and advection.

Our model is based on the conceptually simple hydrodynamic model of actomyosin networks introduced in ref. 23 that invokes (1) mass conservation in the presence of network turnover and (2) force balance. We consider a network with density ρ flowing with a velocity $\mathbf{u}$. Mass conservation implies that the network density ρ changes due to assembly with rate α, disassembly with rate β and drift with velocity $\mathbf{u}$: $\frac{\partial \rho}{\partial t} = \alpha - \beta\rho - \nabla \cdot (\mathbf{u}\rho)$. We use the force-balance equation: $\mu\nabla^2\mathbf{u} + \left(\frac{1}{3}\mu + \lambda\right)\nabla(\nabla \cdot \mathbf{u}) + \nabla\sigma_{\mathrm{contr}} = 0$, for which we assume that the total internal stress in the network is the sum of an active isotropic contractile stress σ_{contr} and a passive viscous stress of an isotropic compressible Newtonian viscous fluid. In the force-balance equation, the first two terms account for the divergence of this viscous stress, where μ and λ are the effective shear and bulk viscosities of the actin network. The friction due to movement of the actin mesh relative to the surrounding fluid is negligible[33]. We explore this model in 2D to approximate the pancake-like geometry of our experimental system and in 1D to approximate the capillary geometry and to gain analytical insight (see the additional discussion of the mechanics of the network in Supplementary Information).

We describe the different mechanical regimes of the network at three density ranges by defining the local network viscosity and active stress (Fig. 4a): (I) At low density, the network is disconnected, consisting of a gas-like solution of unconnected filaments and small network fragments diffusing in the solute, so we assume negligible viscosity and no active force generation. (II) At intermediate densities, the network crosses a percolation transition and becomes interconnected but not yet contracting. In this regime, the network resists deformation, so we assume its viscosity is finite but that the contractile stress is negligible. Note that in Supplementary Information, we consider the possibility of a solid-like (elastic), rather than a fluid-like (viscous), interconnected network, and explain that the predicted behaviour then is essentially the same in 1D and very different in 2D or 3D, unless the network is elastoplastic or has a very low Young's modulus[37,38]. Moreover, the likely reason that the network is non-contracting in this regime is that the active myosin stresses are balanced by elastic stresses (generating a prestressed state); this is simplified here by ignoring the elastic stress and assuming negligible active stress. (III) At higher densities, the network is both interconnected and contracting. Mathematically, we characterize the different regimes as follows: $\mu = \lambda = 0$ if $\rho < \rho_{12}$, $\mu, \lambda > 0$ if $\rho > \rho_{12}$; $\sigma_{\mathrm{contr}} = 0$ if $\rho < \rho_{23}$, and $\sigma_{\mathrm{contr}} = \sigma_0 > 0$ if $\rho > \rho_{23}$, where ρ_{12} and ρ_{23} are the critical densities for network percolation and contractility, respectively. Note that $\rho_{12} < \rho_{23}$, since the network must be percolated to contract. The contractile regime can be characterized by a contraction rate k, which is the ratio of the active stress σ_0 and an effective viscosity η_0, $k = \sigma_0/\eta_0$, where η_0 is a function of μ, λ and a geometric parameter (Supplementary Information). This rate, which has dimensions of inverse time, determines the spatial gradient of the contractile velocity and inverse characteristic time of the network contraction. In general, the viscosities and contractile stress are functions of the density within regions II and III of the state diagram, but for simplicity we approximate them as piece-wise-constant functions of the density. The contraction rate can also be density-dependent, but because of this approximation and based on our observations (Fig. 2e), we take the contraction rate to be a density-independent constant[23].

To account for the boundary conditions in the system, we assume no flow at the dense innermost boundary, where the network sticks to the aggregate at the droplet centre[23,33]. We further assume that actin filaments at the outer boundary of the interconnected network polymerize with an effective rate v_0, so the free boundary of the network grows outwards normally to the boundary with rate $\mathbf{v}_0$. Thus, if the mechanical forces move the material points near this boundary with

https://doi.org/10.1038/s41567-023-02271-5

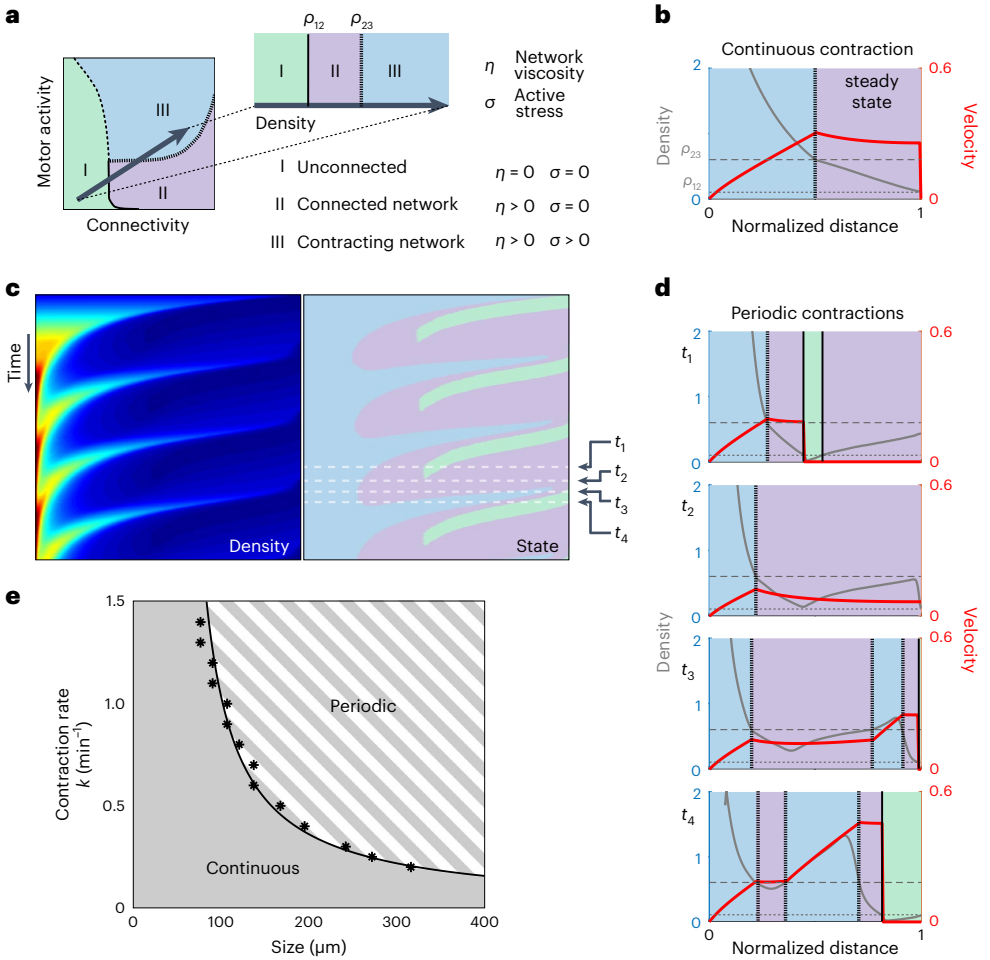

Fig. 4 | Modelling the transition between continuous and periodic contraction. a, Schematic state diagram of the local contractile state as a function of network connectivity and motor activity adapted from[18] (left), and the simplified state diagram as a function of network density used in our model (right). **b**, Graph showing the simulated steady-state density (grey) and velocity (red) distributions as a function of distance from the contraction centre determined from 2D simulations in the continuous contraction regime. The results are shown for the non-dimensionalized variables (Supplementary Information). **c**, Kymographs showing the modulation of network density (left) and the corresponding local network state (right) along a radial cross section as a function of time in the periodic contraction regime, determined from 2D simulations. **d**, Graphs showing the density (grey) and velocity (red) distributions at different time points, as indicated by the arrows in **c** during a wave cycle in the periodic contraction regime (Supplementary Video 13). In **b** and **d**, the dotted and dashed horizontal lines indicate the percolation and contraction density thresholds, respectively. The colours demarcate the regions with unconnected (green), percolated (purple) and contractile (blue) network. The vertical dotted lines show the percolated-contractile region boundaries, and vertical solid lines show the unconnected-percolation region boundaries. **e**, State diagram of the global contractile behaviour of the system as a function of the contraction rate (k) and the system size (R). The system behaviour was simulated for different values of k and R. For each value of k, the transition radius for which periodic behaviour was first observed is indicated (asterisks). The line separating the continuous and periodic contraction regimes was determined from a best fit to the transition length for different values of the contraction rate ($R_{tr} \approx 1.8v_0/k + 1.5v_0/\beta$).

velocity $\mathbf{u}$, the network boundary moves with a net velocity $(\mathbf{u} + \mathbf{v}_0)$. The parameter v_0 reflects the rate of elongation of actin filaments at the network boundary and is, thus, proportional to the actin assembly rate $\alpha \approx nv_0$, where n is the local number of growing filaments per unit length (in 1D) or area (in 2D), providing the density is measured in units of filament length per unit length (1D) or area (2D), respectively.

We solve the model equations numerically in 2D (Fig. 4) and in 1D (Extended Data Fig. 6; details in Supplementary Information). In the simulations, we take experimentally measured values or estimated realistic values for model parameters, such as the polymerization rate v_0 and network disassembly rate β, and varied two key parameters, namely the radius of the droplet R and the contraction rate k. The model makes a simple prediction: if the droplet size is smaller than a critical size, $R < R_{tr} = cv_0/k$, where c is a dimensionless parameter of order unity, then a continuous steady centripetal network flow is maintained (Fig. 4b,e), as described previously[23]. However, if the droplet radius exceeds the critical transition length R_{tr}, then pulsatile contraction waves emerge (Fig. 4c,e and Supplementary Video 13). Snapshots from the simulation (Fig. 4d) illustrate the key events in a wave cycle: (1) Time t_1: the contracting network recedes away from the droplet boundary until the periphery of the interconnected network stabilizes at a position r_{12} where the network density is equal to ρ_{12} (left boundary of the green region in Fig. 4d) and the network flows centripetally with speed v_0, balancing the network growth. The position of the boundary between the inner interconnected network and the unconnected network (purple–green boundary) remains stationary whereas the network density increases over time due to net assembly. (2) Time t_2: the connectivity threshold density is reached everywhere, and a new wave initiates as a mechanical bridge is formed between the contracting network near the core and the newly assembled region extending to the droplet periphery. (3) Time t_3: the network density reaches the contractile regime in a region near the periphery (outer blue region),

accelerating the wave. (4) Time t_4: inward contraction of the network results in a region that is transiently unconnected near the droplet boundary (green region). Note that the outer contractile region (outer blue region) is flanked at both sides by narrow percolated but non-contractile regions (purple) at this time. The same model can also be used to simulate the dynamics of the system when the contraction rate is gradually increased over time. In this case, a droplet of a given size can transition from continuous to periodic contraction (Extended Data Fig. 7b and Supplementary Video 14), as observed experimentally (Fig. 3c,d).

The global contractile behaviour of the system can, thus, be characterized as a function of two important factors: the system size R and the contraction rate k. These can be used to predict a state diagram for steady/periodic contractile behaviour in the k–R parameter space (Fig. 4e). The transition length (R_{tr}) is predicted to be inversely proportional to the contraction rate as observed experimentally (Fig. 2f), which is easy to understand as follows. In the continuously contracting case, the interconnected network boundary is stationary and, hence, flowing inwards with a velocity equal to the growth rate of the network boundary, v_0. Near the transition length, the radial position of the contracting network boundary is approximately v_0/k, whereas the radial position of the outward interconnected network boundary, which is a little farther outwards, is cv_0/k where $c \approx 1$. The outward interconnected network boundary must be near the droplet interface, otherwise the unconnected fragments at the droplet periphery will periodically assemble and generate periodic contractions. Thus, $R_{tr} \approx cv_0/k$ (see the detailed analysis in Supplementary Information). This argument further suggests that the wave period should be determined by the time interval required for the network to assemble from scratch at the periphery up to the critical density, which is of the order of the network turnover timescale or the inverse disassembly rate β (Supplementary Information). Indeed, model simulations show the wave period is a few-fold $1/\beta$ and is largely insensitive to the system size R and the contraction rate k (Extended Data Fig. 8), as observed experimentally (Fig. 2c,g). Furthermore, simulations in which the actin assembly rate is gradually decreased directly show that the time interval between subsequent wavefronts becomes larger as assembly slows down (Extended Data Fig. 7a), as observed experimentally when actin subunits are sequestered over time with phalloidin (Fig. 3a,b).

The importance of the assumption that the interconnected network edge grows due to actin polymerization becomes clear: without it, the contractile network would recede at an ever slowing but finite speed towards the centre, leaving a small gap with an unconnected region just behind it. This gap would never allow the growing density at the periphery to connect to the central contracting core, thus generating a local contraction at the periphery rather than a global contraction towards the centre. Alternative mechanisms that could generate a global contraction are also possible. One possibility is that there are long non-contractile actin bundles permeating the active network and creating a non-stretchable but easily compressible cable net, which connects all the actively contractile local domains of the actomyosin network to ensure global contractions. Another possibility that could explain the global inward contraction in droplets, but not the waves in flat capillaries (Extended Data Fig. 2), requires neither global interconnections nor network edge growth. This possibility is the contraction of closed actomyosin shells from the periphery due to the net contribution of tangential stresses along a curved wavefront (Extended Data Fig. 9)[29]. We discuss these and additional alternative models in the Discussion and in Supplementary Information.

Transition from a global to a local contraction

Previous work on actomyosin networks in the absence of turnover identified a transition from global contraction that spans the system size to local contraction, during which the network breaks down into multiple discrete clusters[12,15,16]. This transition has been shown to occur at high motor activity accompanied by limited network connectivity[18,19]. Importantly, in the absence of continuous actin assembly, the initiation of contraction is an irreversible step; any local contraction event leads to the failure of the network, which breaks into separate clusters that cannot be reconnected[16,18]. Continuous actin assembly can facilitate the reformation of mechanical links between distinct contracting regions, changing the percolation dynamics in the system in a qualitative manner, and hence, can lead to richer spatiotemporal contractile dynamics.

When actin turnover is rapid, the continuous model exhibits short-range instabilities making the contraction local (see the details in Supplementary Information). These instabilities are difficult to simulate in the continuous framework, which is why we turn to a discrete agent-based model that allows us to better explore the transition between local and global contraction in the presence of rapid turnover (see details in Supplementary Information). As the connectivity is decreased (or the contraction rate is increased), we find a transition from global contraction to local contraction clusters (Extended Data Fig. 10), as previously reported for systems lacking turnover[12,13,17,18]. At high connectivity, the system exhibits global contraction, forming a single system-spanning contracting cluster, which due to the rapid turnover exhibits a steady state with a continuous centripetal flow[23]. At low connectivity, the system breaks into local high-density 'asters' characterized by small size and rapid centripetal flow. These appear at random locations, with large spaces between them that are devoid of an interconnected network. However, interestingly, we also find an intermediate regime in which the contraction pattern alternates repeatedly between a local and a global contraction; the system exhibits recurrent cycles of contraction into local clusters that subsequently get connected with a dense central and steadily contracting core cluster (Extended Data Fig. 10). Thus, in this intermediate regime, the contraction occurs on a range of length scales. Initially, local contracting asters emerge in a similar manner as in the locally contracting regime. However, since the intercluster regions can reassemble and repeatedly reach the percolation threshold, neighbouring clusters can connect and subsequently merge with each other. Due to the random fluctuations of the connectivity, the intermediate contraction regime can be irregular.

Experimentally, we were able to induce a local contraction either by increasing the myosin activity (hence, increasing the contraction rate) or by limiting the filament length (hence, diminishing the network connectivity) (Fig. 5). This was done using either calyculin A, which enhanced myosin activity by inhibiting myosin-light-chain phosphatase from dephosphorylating myosin, or by adding capping protein, which capped the barbed ends of free-growing actin filaments. Adding calyculin generated an intermediate state such that within the same region we saw alternating behaviours, with local contraction to a nearby contraction centre, which subsequently merged with other clusters to generate overall a global contraction pattern (Fig. 5a and Supplementary Video 15). The contraction pattern became more irregular at higher calyculin concentrations. Similar behaviour, with repeated transitions between local and global contractile behaviour, was seen upon the addition of intermediate levels of capping protein, which reduced network connectivity (Fig. 5b, left, and Supplementary Video 16). At an even higher capping protein concentration, the system broke into local clusters (Fig. 5b, right). Although these clusters could dynamically interact with each other and sometimes even merge, under these conditions, the contraction remained local, and we did not observe any substantial coarsening or global contraction to a central cluster.

Discussion

Contracting actin networks exhibit a myriad of dynamic behaviours in vivo, including large-scale persistent flows, pulsatile contractions and local contractions[1–3]. Many of these behaviours have been reconstituted in vitro, with systems exhibiting global contraction in the form of continuous flows[23,24] or periodic waves[13,15,27–30], as well as local

https://doi.org/10.1038/s41567-023-02271-5

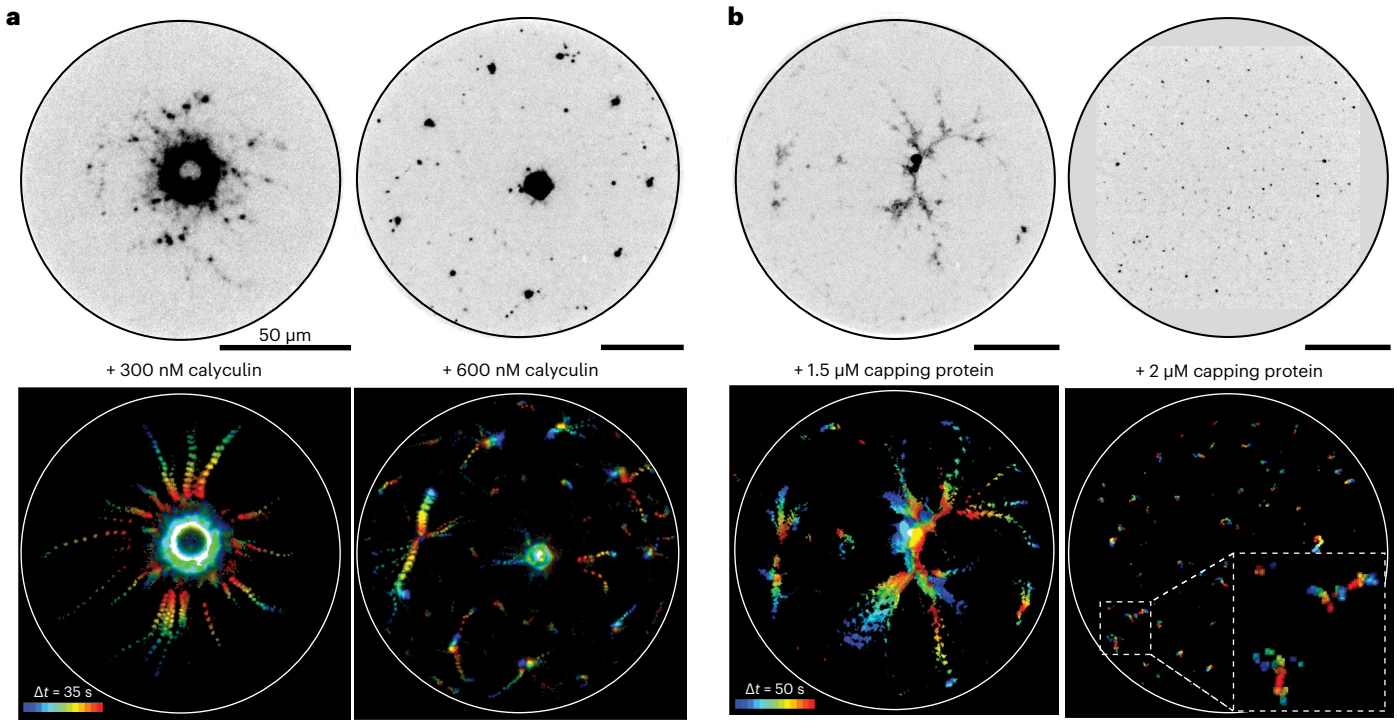

Fig. 5 | Transition from a global to a local contraction. a,**b**, Spinning-disc confocal images of water-in-oil droplets containing 80% extract supplemented with calyculin A (Supplementary Video 15) (**a**) or capping protein (Supplementary Video 16) (**b**). The dynamic contractile behaviour is displayed by overlaying consecutive frames colour-coded for time (bottom). The addition of calyculin A or capping protein leads to the formation of local contraction clusters. In some cases, the local clusters eventually contract to a global contraction centre, except at a high enough concentration of capping protein (**b**, right).

contraction into clusters[12,16,39]. Here we use a reconstituted system based on cell extracts that exhibits rapid, physiological actin turnover rates to explore a wide range of conditions and geometries and reveal a size-dependent transition from continuous to periodic contraction.

The appearance of global contraction with different spatiotemporal patterns highlights the subtle interplay between network structure, contractile force generation and geometry. As discussed previously[18,40], to generate and transmit forces across the system, the network must be percolated, yet these internal forces, in turn, also modulate the network structure and connectivity. In the presence of rapid turnover, the extent of connected clusters within which forces are efficiently transmitted becomes a dynamic variable. Local clusters can form and contract but they can also join into an interconnected network, as actin assembly can form bridges between previously unconnected clusters. In this context, one has to consider a more dynamic version of the percolation problem that includes internally generated large-scale advection as well as network assembly and disassembly. The contractile behaviour of the system can no longer be summarized by a state diagram depending on the overall motor activity and network connectivity[12,13,18,41,42]. Rather, one has to consider the geometry of the system and the spatial inhomogeneities that develop within the system. Our results suggest that the previously characterized state diagram is still relevant for describing the local contractile behaviour at the mesoscale. However, to account for the emergent global behaviour of the system, one has to consider the dynamic evolution of the system into a collection of regions with distinct mechanical properties. Interestingly, our work shows that the system size becomes an important factor in regulating the self-organized patterns that emerge; in particular, our work reveals a previously unappreciated transition whereby the same molecular components can self-organize into a persistent flow pattern or exhibit periodic waves, depending on the overall size of the system.

Recent work shows that similar contraction patterns containing distinct regions with different rheological properties emerge in cortical actomyosin networks of living cells. These patterns provide the basis for a novel motility mechanism in disordered 3D environments[43]. The unconnected gas-like state allows for the formation of protrusions at the leading edge of a cell that can penetrate a disordered environment. The subsequent actin assembly generates a rigid, percolated cortical network, which is pulled rearwards by myosin-generated contractile forces at the cell rear. The suggested motility mechanism uses these rigid cortical regions, which assemble within the irregularly shaped protrusions, to generate normal forces on the cell environment as the network is pulled rearwards, thus providing an efficient mechanism for momentum transfer to propel the cell forwards.

The observed phenomenology in the cortex of these motile cells[43], with large-scale self-organized contractile patterns arising from a percolation transition in an active network undergoing continuous advection and turnover, is strikingly similar to our observations in bulk networks in vitro. In both cases the interconnected network formed above the rigidity-percolation transition facilitates long-range force transmission across the system (which is essential for global contraction) and at the same time is modulated by the internal advection generated by these forces. However, the geometry of the system has an important influence on the properties of the network. In the effective 1D geometry of the cortical networks on the surface of a cylindrical cell or bleb, the network can flow rearwards as a solid, experiencing negligible stress, before fluidizing at the rear due to myosin-generated forces. However, in a 2D or 3D radially symmetric contracting network, the converging flow necessarily generates stress and, hence, the percolated network must be primarily viscous rather than solid (see more details in Supplementary Information).

The appearance of pulsatile modulation in actomyosin contraction is a common theme seen across many cell types in different contexts (for example, refs. 6,8,10,44). Although in some cases the function of the pulsatile dynamics is unclear, in other cases the pulsatile dynamics are essential, enabling large-scale force generation while maintaining tissue integrity[8,9] and facilitating cellular functions

such as active transport and motility[6]. Typically, these periodic or aperiodic waves emerge from complex nonlinear reactions in coupled mechano-chemical systems involving regulators of the actomyosin machinery such as Rho GTPases[10,11,42,45,46]. Our work shows that waves can also emerge in essentially mechanical systems with turnover but without complex biochemical regulation. In this case, the periodic dynamics reflect an emerging spatiotemporal pattern that depends on the interplay between network contraction and turnover, rather than biochemical modulation of the actomyosin machinery. The period of the waves is comparable to the actin turnover timescale, which allows the network in the wake of a wavefront to reassemble and generate subsequent contracting wavefronts (Supplementary Information). Whether such mechanically generated waves naturally arise in living systems and are functionally relevant remains to be seen.

Theoretically, actomyosin contraction has been studied extensively using microscopic agent-based simulations as well as continuum hydrodynamic approaches. Several studies have explicitly simulated microscopic models of actin filaments, myosin motors and crosslinkers (both motors and linkers stochastically bind to and unbind from filaments). Even without turnover, pulsed, geometrically irregular contraction can emerge because of the positive feedback between the local network density and the effective contractile stress (due to more motors binding to denser actin arrays)[19,41]. Note that repeated irregular contractions in such systems depend on the stochastic unbinding of motors and crosslinkers, which effectively dissolves transient network aggregates and allows contractions to start elsewhere. Large-scale geometrically irregular pulsed contractions of similar nature appear in models with actin turnover[21,47]. Interestingly, a couple of models have shown that such pulsed contractions can, in fact, be suppressed by actin turnover[20,48].

Other models, albeit not microscopic, have demonstrated that not just irregular but also periodic contractions can develop in actomyosin networks. First, such periodic contractions can be generated by an effective relaxation oscillator based on the coupling of network turnover with a highly nonlinear stress–density relation characterized by both a contractile phase at low network density and a relatively exotic swelling phase at high density[31,32]. Second, travelling contraction waves appear in dense actomyosin structures with myosin strain-dependent binding/unbinding kinetics[49], so in effect, some additional nonlinear kinetics has to be added to facilitate the existence of such waves. Third, one can build a spatial-temporal oscillator by coupling not just viscous but also elastic elements to a contractile actomyosin network with turnover[50], which could be more relevant to supracellular than cellular systems. Last, but not least, spatial-temporal instabilities in a highly contractile actomyosin network with turnover, like those predicted by our model for large contraction rates (Supplementary Information), were predicted in ref. 51. None of these models, however, addressed the relationship between the contraction pattern and the geometry of the system, as done in this work.

Interestingly, our system also exhibits contraction in the form of spiral wave patterns (Fig. 1e, Extended Data Fig. 4 and Supplementary Video 8). Dynamic spiral patterns have been observed in several physiological systems, including the actin cortex, and are usually associated with highly nonlinear excitable systems[44] or intrinsic chirality at the molecular scale, which is propagated to cellular scales[52,53]. Although we have not yet attempted to quantitatively model spiral formation (our current model is limited to radially symmetric 2D patterns), we hypothesize that the spiral contraction waves we observe originate from a different and somewhat simpler mechanism. Along each radial direction, we have shown that the periodic waves are triggered, effectively, by an 'integrate-and-fire' oscillator[54]: at the beginning of each cycle, the network density assembles to the percolation/contraction threshold ('integrate' part), which triggers a contraction that wipes out the density from the periphery ('fire' part) and resets the cycle. Each oscillator is characterized by a phase, namely the timing of the start of the cycle. There are lateral mechanical connections in the network between neighbouring radial directions, so effectively we can consider them as coupled oscillators. Mathematical models have demonstrated that such coupling leads, most frequently, to two possible patterns[54]: (1) synchronization of the oscillator phases, which geometrically corresponds to periodic waves in the form of concentric contracting circles, which is most often the case, or (2) an incremental phase shift between nearest-neighbour oscillators, which geometrically corresponds to a spiral pattern arising from some initial conditions. Note that such models predict that the spiral will develop so that along each radial direction the new wave starts at the periphery exactly when the previous wave crest merges with the dense network near the centre, which seems to be the case in our system (Fig. 1e,f and Extended Data Fig. 4). Further research will show whether this coupled oscillator mechanism is behind the spiral contraction waves and whether these waves have a physiological significance.

Living systems exhibit patterns at different length scales depending on the mechanism driving their organization. The most prevalent mechanisms are diffusion-based biochemical pattern formation, such as Turing patterns, and various mechano-chemical patterns[55]. Here, we demonstrate the existence of an emergent length scale based on coupling between mechanics, turnover and geometry. This characteristic length scale defines the transition length above which the contractile behaviour of the system changes in a qualitative manner so that periodic behaviour develops. The size-dependent contractile behaviour that emerges from the interplay between network advection, percolation and force generation was not appreciated before and highlights the importance of the system geometry on its self-organized dynamics: the geometry of the system is not only reflected in the shape of the contracting wavefront but also in its temporal dynamics. More generally, this work provides an example of the profound impact that geometry and boundary conditions can have on pattern formation processes in cells and tissues.

Online content

Any methods, additional references, Nature Portfolio reporting summaries, source data, extended data, supplementary information, acknowledgements, peer review information; details of author contributions and competing interests; and statements of data and code availability are available at https://doi.org/10.1038/s41567-023-02271-5.

References

1. Field, C. M. & Lenart, P. Bulk cytoplasmic actin and its functions in meiosis and mitosis. *Curr. Biol.* **21**, R825–R830 (2011).
2. Salbreux, G., Charras, G. & Paluch, E. Actin cortex mechanics and cellular morphogenesis. *Trends Cell Biol.* **22**, 536–545 (2012).
3. Munjal, A. & Lecuit, T. Actomyosin networks and tissue morphogenesis. *Development* **141**, 1789–1793 (2014).
4. Koenderink, G. H. & Paluch, E. K. Architecture shapes contractility in actomyosin networks. *Curr. Opin. Cell Biol.* **50**, 79–85 (2018).
5. Murrell, M., Oakes, P. W., Lenz, M. & Gardel, M. L. Forcing cells into shape: the mechanics of actomyosin contractility. *Nat. Rev. Mol. Cell Biol.* **16**, 486–498 (2015).
6. Munro, E., Nance, J. & Priess, J. R. Cortical flows powered by asymmetrical contraction transport PAR proteins to establish and maintain anterior–posterior polarity in the early *C. elegans* embryo. *Dev. Cell* **7**, 413–424 (2004).
7. Lenart, P. et al. A contractile nuclear actin network drives chromosome congression in oocytes. *Nature* **436**, 812–818 (2005).
8. Martin, A. C., Kaschube, M. & Wieschaus, E. F. Pulsed contractions of an actin–myosin network drive apical constriction. *Nature* **457**, 495–499 (2009).
9. Jodoin, J. N. et al. Stable force balance between epithelial cells arises from F-actin turnover. *Dev. Cell* **35**, 685–697 (2015).
10. Nishikawa, M., Naganathan, S. R., Julicher, F. & Grill, S. W. Controlling contractile instabilities in the actomyosin cortex. *eLife* **6**, e19595 (2017).

11. Agarwal, P. & Zaidel-Bar, R. Principles of actomyosin regulation in vivo. *Trends Cell Biol.* **29**, 150–163 (2019).
12. Backouche, F., Haviv, L., Groswasser, D. & Bernheim-Groswasser, A. Active gels: dynamics of patterning and self-organization. *Phys. Biol.* **3**, 264 (2006).
13. Bendix, P. M. et al. A quantitative analysis of contractility in active cytoskeletal protein networks. *Biophys. J.* **94**, 3126–3136 (2008).
14. Reymann, A.-C. et al. Actin network architecture can determine myosin motor activity. *Science* **336**, 1310–1314 (2012).
15. Kohler, S. & Bausch, A. R. Contraction mechanisms in composite active actin networks. *PLoS ONE* **7**, e39869 (2012).
16. Alvarado, J., Sheinman, M., Sharma, A., MacKintosh, F. C. & Koenderink, G. H. Molecular motors robustly drive active gels to a critically connected state. *Nat. Phys.* **9**, 591–597 (2013).
17. Ennomani, H. et al. Architecture and connectivity govern actin network contractility. *Curr. Biol.* **26**, 616–626 (2016).
18. Alvarado, J., Sheinman, M., Sharma, A., MacKintosh, F. C. & Koenderink, G. H. Force percolation of contractile active gels. *Soft Matter* **13**, 5624–5644 (2017).
19. Belmonte, J. M., Leptin, M. & Nedelec, F. A theory that predicts behaviors of disordered cytoskeletal networks. *Mol. Syst. Biol.* **13**, 941 (2017).
20. McFadden, W. M., McCall, P. M., Gardel, M. L. & Munro, E. M. Filament turnover tunes both force generation and dissipation to control long-range flows in a model actomyosin cortex. *PLoS Comput. Biol.* **13**, e1005811 (2017).
21. Hiraiwa, T. & Salbreux, G. Role of turnover in active stress generation in a filament network. *Phys. Rev. Lett.* **116**, 188101 (2016).
22. Brieher, W. Mechanisms of actin disassembly. *Mol. Biol. Cell* **24**, 2299–2302 (2013).
23. Malik-Garbi, M. et al. Scaling behaviour in steady-state contracting actomyosin networks. *Nat. Phys.* **15**, 509–516 (2019).
24. Pinot, M. et al. Confinement induces actin flow in a meiotic cytoplasm. *Proc. Natl Acad. Sci. USA* **109**, 11705–11710 (2012).
25. Abu-Shah, E. & Keren, K. Symmetry breaking in reconstituted actin cortices. *eLife* **3**, e01433 (2014).
26. Tan, T. H. et al. Self-organization of stress patterns drives state transitions in actin cortices. *Sci. Adv.* **4**, eaar2847 (2018).
27. Ezzell, R. M., Brothers, A. J. & Cande, W. Z. Phosphorylation-dependent contraction of actomyosin gels from amphibian eggs. *Nature* **306**, 620–622 (1983).
28. Field, C. M. et al. Actin behavior in bulk cytoplasm is cell cycle regulated in early vertebrate embryos. *J. Cell Sci.* **124**, 2086–2095 (2011).
29. Sakamoto, R. et al. Tug-of-war between actomyosin-driven antagonistic forces determines the positioning symmetry in cell-sized confinement. *Nat. Commun.* **11**, 1–13 (2020).
30. Sakamoto, R., Miyazaki, M. & Maeda, Y. T. State transitions of a confined actomyosin system controlled through contractility and polymerization rate. *Phys. Rev. Res.* **5**, 013208 (2023).
31. Pohl, T. in *Lecture Notes in Biomathematics: Biological Motion*, Vol. 89 (eds Alt, W. & Hoffmann, G.) 85–94 (Springer, 1990).
32. Alt, W. & Dembo, M. Cytoplasm dynamics and cell motion: two-phase flow models. *Math. Biosci.* **156**, 207–228 (1999).
33. Ierushalmi, N. et al. Centering and symmetry breaking in confined contracting actomyosin networks. *eLife* **9**, e55368 (2020).
34. Wuhr, M. et al. Deep proteomics of the *Xenopus laevis* egg using an mRNA-derived reference database. *Curr. Biol.* **24**, 1467–1475 (2014).
35. Zicha, D. et al. Rapid actin transport during cell protrusion. *Science* **300**, 142–145 (2003).
36. Keren, K., Yam, P. T., Kinkhabwala, A., Mogilner, A. & Theriot, J. A. Intracellular fluid flow in rapidly moving cells. *Nat. Cell Biol.* **11**, 1219–1224 (2009).
37. Ideses, Y. et al. Spontaneous buckling of contractile poroelastic actomyosin sheets. *Nat. Commun.* **9**, 2461 (2018).
38. Sadhukhan, P., Schumann, O. & Heussinger, C. Elasto-plastic response of reversibly crosslinked biopolymer bundles. *Eur. Phys. J. E* **37**, 1–9 (2014).
39. Wollrab, V. et al. Polarity sorting drives remodeling of actin-myosin networks. *J. Cell Sci.* **132**, jcs219717 (2019).
40. Bueno, C., Liman, J., Schafer, N. P., Cheung, M. S. & Wolynes, P. G. A generalized Flory-Stockmayer kinetic theory of connectivity percolation and rigidity percolation of cytoskeletal networks. *PLoS Comput. Biol.* **18**, e1010105 (2022).
41. Freedman, S. L., Hocky, G. M., Banerjee, S. & Dinner, A. R. Nonequilibrium phase diagrams for actomyosin networks. *Soft Matter* **14**, 7740–7747 (2018).
42. Banerjee, S., Gardel, M. L. & Schwarz, U. S. The actin cytoskeleton as an active adaptive material. *Annu. Rev. Condens. Matter Phys.* **11**, 421–439 (2020).
43. García-Arcos, J. M. et al. Advected percolation in the actomyosin cortex drives amoeboid cell motility. Preprint at https://www.biorxiv.org/content/10.1101/2022.07.14.500109v1.abstract (2022).
44. Bement, W. M. et al. Activator-inhibitor coupling between Rho signalling and actin assembly makes the cell cortex an excitable medium. *Nat. Cell Biol.* **17**, 1471–1483 (2015).
45. Allard, J. & Mogilner, A. Traveling waves in actin dynamics and cell motility. *Curr. Opin. Cell Biol.* **25**, 107–115 (2013).
46. Staddon, M. F., Munro, E. M. & Banerjee, S. Pulsatile contractions and pattern formation in excitable actomyosin cortex. *PLoS Comput. Biol.* **18**, e1009981 (2022).
47. Mak, M., Zaman, M. H., Kamm, R. D. & Kim, T. Interplay of active processes modulates tension and drives phase transition in self-renewing, motor-driven cytoskeletal networks. *Nat. Commun.* **7**, 1–12 (2016).
48. Yu, Q., Li, J., Murrell, M. P. & Kim, T. Balance between force generation and relaxation leads to pulsed contraction of actomyosin networks. *Biophys. J.* **115**, 2003–2013 (2018).
49. Banerjee, D. S., Munjal, A., Lecuit, T. & Rao, M. Actomyosin pulsation and flows in an active elastomer with turnover and network remodeling. *Nat. Commun.* **8**, 1121 (2017).
50. Dierkes, K., Sumi, A., Solon, J. E. O. & Salbreux, G. Spontaneous oscillations of elastic contractile materials with turnover. *Phys. Rev. Lett.* **113**, 148102 (2014).
51. Hannezo, E., Dong, B., Recho, P., Joanny, J.-F. C. & Hayashi, S. Cortical instability drives periodic supracellular actin pattern formation in epithelial tubes. *Proc. Natl Acad. Sci. USA* **112**, 8620–8625 (2015).
52. Naganathan, S. R., Fürthauer, S., Nishikawa, M., Julicher, F. & Grill, S. W. Active torque generation by the actomyosin cell cortex drives left-right symmetry breaking. *eLife* **3**, e04165 (2014).
53. Tee, Y. H. et al. Cellular chirality arising from the self-organization of the actin cytoskeleton. *Nat. Cell Biol.* **17**, 445–457 (2015).
54. Bressloff, P. C. Mean-field theory of globally coupled integrate-and-fire neural oscillators with dynamic synapses. *Phys. Rev. E* **60**, 2160 (1999).
55. Bailles, A. I., Gehrels, E. W. & Lecuit, T. Mechanochemical principles of spatial and temporal patterns in cells and tissues. *Annu. Rev. Cell Dev. Biol.* **38**, 321–347 (2022).

Methods

Cell extracts, proteins and reagents

Concentrated M-phase extracts were prepared from freshly laid *Xenopus laevis* eggs as previously described[25,56,57]. Briefly, *Xenopus* frogs were injected with hormones to induce ovulation and the laying of unfertilized eggs for extract preparation. The eggs from different frogs were pooled together and washed with 1× MMR (100 mM NaCl, 2 mM KCl, 1 mM $MgCl_2$, 2 mM $CaCl_2$, 0.1 mM EDTA and 5 mM Na-Hepes, pH 7.8), at 16 °C. The jelly envelope surrounding the eggs was dissolved using 2% cysteine solution (in 100 mM KCl, 2 mM $MgCl_2$ and 0.1 mM $CaCl_2$, pH 7.8). Finally, the eggs were washed with CSF-XB (10 mM K-Hepes pH7.7, 100 mM KCl, 1 mM $MgCl_2$, 5 mM EGTA, 0.1 mM $CaCl_2$ and 50 mM sucrose) containing protease inhibitors (10 μg ml^{-1} each of leupeptin, pepstatin and chymostatin). The eggs were then packed using a clinical centrifuge and crushed by centrifugation at 15,000*g* for 15 min at 4 °C. The crude extract (the middle yellowish layer out of three layers) was collected, supplemented with 50 mM sucrose containing protease inhibitors (10 μg ml^{-1} each of leupeptin, pepstatin and chymostatin), snap-frozen as 10 μl aliquots in liquid N_2 and stored at −80 °C. Typically, for each extract batch, a few hundred aliquots were made. Different extract batches exhibited similar behaviour qualitatively, but the contraction rate and transition length exhibited some variation. All comparative analyses between conditions were done using the same batch of extract, but similar trends were observed in all extracts examined. The protein composition of *Xenopus* egg extracts was previously analysed by quantitative mass spectrometry[34]. Based on this analysis, the concentrations of actin and related proteins in our extracts can be estimated as follows: ~33 μM of actin subunits (including cytoplasmic-Gamma, alpha smooth and alpha cardiac isoforms), ~2.0 μM myosin IIA, ~0.2 μM myosin IIB, ~1.4 μM capping protein and ~0.4 μM Arp2/3 complex.

ActA–His was purified from strain JAT084 of *Listeria monocytogenes* (a gift from J. Theriot, Stanford University) that expresses a truncated *actA* gene encoding amino acids 1–613 with a COOH-terminal six-histidine tag replacing the transmembrane domain, as described in refs. 25,57. The capping protein of actin filaments, Capz, which contains two subunits, α-1 and β-1, was purified to a final concertation of 66 μM in 10 mM Tris8, 50 mM NaCl, 0.5 mM dithiothreitol (DTT) and 20% sucrose. GST-mDia was purified to a final concertation of 45 μM in 10 mM Tris7.5, 50 mM KCl, 1 mM EGTA, 1 mM $MgCl_2$, 1 mM DTT, 20 mM glutathione and 15% sucrose. Purified proteins were aliquoted, snap-frozen in liquid N_2 and stored at −80 °C until use. Calyculin A (Sigma) was added at 0–600 nM to the extract mix. Phalloidin (Invitrogen) was added at 20 μM to the extract mix. For tracking the cytoplasmic flow, red fluorescent 0.5-μm-diameter carboxylate modified polystyrene beads (Sigma) were used. The beads were passivated by incubating with 0.5 mg ml^{-1} BSA in XB buffer before use. Actin networks were labelled with lifeact-green fluorescent protein (GFP) (the construct was a gift from C. Field, Harvard Medical School). Lifeact-GFP was purified and concentrated to a final concentration of 252 μM in 100 mM KCl, 1 mM $MgCl_2$, 0.1 mM $CaCl_2$, 1 mM DTT and 10% sucrose and stored at −80 °C until use.

Sample preparation

For samples with 80% extract, an aqueous mix was prepared by mixing the following: 8 μl crude extract, 0.5 μl ×20 ATP regenerating mix (150 mM creatine phosphate, 20 mM ATP and 20 mM $MgCl_2$), 0.5 μl of 10 μM lifeact-GFP and any additional proteins as indicated. The final volume was adjusted to 10 μl by adding XB buffer (10 mM Hepes, 5 mM EGTA, 100 mM KCl, 2 mM $MgCl_2$ and 0.1 mM $CaCl_2$ at pH 7.8). For samples with a higher extract concentration (85–98%), the crude extract was supplemented with a ×50 concentrated mix containing ATP regenerating system and lifeact-GFP to generate the same final concentrations.

Emulsions were made by adding 3% (v/v) extract mix to degassed mineral oil (Sigma) containing 4% cetyl PEG/PPG-10/1 dimethicone (Abil EM90, Evnok Industries) and stirring for 1 min at 4 °C. The mix was then incubated for an additional 10 min on ice to allow the emulsions to settle.

Samples were made in chambers assembled from two passivated coverslips separated by 10-μm or 30-μm-thick double stick tape (3M), sealed with wax (vaseline:lanolin:paraffin in a 1:1:1 ratio) and attached to a glass slide. For samples with spherical droplets, we used a thicker 400 μm spacer made from multiple layers of 100-μm-thick double-sided sticky tape (3M). When generating macroscopic droplets (~1 cm), 10 μl of the extract mix (without emulsification) was sandwiched between passivated coverslips with a 100-μm-thick spacer. Passivation was done by incubating cleaned coverslips in a silanization solution (5% dichlorodimethylsilane in heptane) for 20 min, washing in heptane, and sonicating twice in doubled-distilled water for 5 min and once in ethanol for 5 min. For the capillary experiments, the extract mix (without making an emulsion) was introduced into a 50 × 500 μm rectangular capillary (CM Scientific) through capillary action, and the capillary ends were sealed with VALAP. Samples were typically imaged 10–60 min after sample preparation.

Microscopy

Emulsions were imaged at room temperature on a Zeiss Observer Z1 confocal microscope fitted with a Yokogawa CSU-X1 spinning disc using Slidebook software for acquisition (Intelligent Imaging Innovations). Samples were illuminated with a 488 nm laser, and images were captured at the midplane of the sample so that the network velocity was mostly within the imaging plane. 3D images of spherical droplets were captured by acquiring a Z-stack of the droplet and deconvolving the 3D image using FIJI followed by 3D median filtering. To characterize the network properties, images with a high temporal resolution were obtained with ×10 air (numerical aperture (NA) = 0.5), ×20 air (NA = 0.75) or ×40 oil (NA = 1.3) objectives with or without an optovar (×1.6), depending on the size of the droplets. Images were acquired onto a 512 × 512 EM-CCD camera (QuantEM; Photometrix) at 0.5 s time resolution.

Low time resolution images for characterizing the global contractile behaviour in a population of droplets were acquired using a 2048 × 2048 CMOS camera (Zyla, Andor) with a ×20 air (NA = 0.5) objective. Images were acquired with 2 × 2 binning at 15 s time interval for a duration of 8 min.

Analysis

Network properties of bulk actin network in emulsions. High time resolution time-lapse videos were acquired at the midplane of a sample to obtain the bulk actin network flows as in ref. 23. Time-lapse videos were background-corrected, corrected for uneven illumination by normalizing with flat field corrections and bleach corrected using an exponential fit to the total image intensity as a function of time.

The velocity fields were extracted from the corrected time-lapse videos using either an optical flow with a reaction term to account for network turnover using the code adapted from ref. 58 and modified as described below or particle image velocimetry (PIV) as described previously[23]. The optical flow analysis used videos with a 0.5 s time interval, whereas the PIV analysis was done at 2.5–10.0 s time interval with additional averaging of the spatiotemporal correlation function over 3–40 consecutive frames[23]. For continuous contraction, both methods yielded similar results. However, for the non-steady contraction, only the optical flow method could be used because the temporal changes in the velocity field were fast compared to the timescales used for averaging the spatiotemporal correlation function in the PIV method (which are essential for obtaining a reasonable velocity field).

The optical flow analysis was performed on 15 × 15 pixel window. Consecutive pairs of images were first smoothed with a Gaussian filter (σ = 1.5 pixels) and subsequently analysed with a reaction term using the Matlab code provided in[58]. The velocity fields were subsequently

averaged over five consecutive frames (2.5 s) using a 15 × 15 median filter to reduce noise. For continuous contraction, the velocity field was further down-sampled to a final resolution of 12.5 s and 15 × 15 pixels by averaging. The contraction rate in the continuous contraction regime was determined from the slope of the linear fit to the radial velocity as a function of distance to the contraction centre[23].

Radial kymographs of the density and the velocity fields as a function of distance from the contraction centre were obtained by angular averaging. The averaging was done over all angles for droplets with a symmetric contraction or over a smaller manually selected angular range otherwise. Angular kymographs (for spiral videos) were determined by considering the angular variation in a specified radial range.

Population statistics. The population statistics were acquired from time-lapse images of droplets with varying sizes at 15 s time intervals (to capture at least two frames per period in the periodic regime). For each droplet, radial intensity kymographs were obtained as above. The state of contraction in each droplet was categorized as continuous or periodic based on manual inspection of the radial kymographs. For droplets exhibiting periodic density modulations (that is, parallel diagonal lines in the radial kymograph), the time period was determined from analysing the time-dependent intensity variation for a small radial region (that is, along a vertical line in the kymograph) using the built-in Matlab function 'periodogram'. The periodicity was determined from the position of the most prominent peak in the Fourier spectrum, estimated from the location of the centre of a best-fitting Gaussian. The width of the best-fitting Gaussian was used to estimate the error in the periodicity. The period was determined only for droplets that remained stationary throughout the video. Droplets that exhibited irregular density modulations rather than a clear periodic pattern were characterized to be in a mixed state.

The transition length was determined for various conditions by considering the contraction state versus size (Fig. 2b). For conditions with a size range in which droplets were found exhibiting both continuous and periodic contraction, the transition length (R_{tr}) was defined to minimize the number of droplets exhibiting periodic contraction with $R < R_{tr}$ and continuous contraction with $R > R_{tr}$. If there was no overlap, the transition length was reported as the mean of the sizes of the smallest droplet exhibiting periodic contraction and the largest droplet exhibiting continuous contraction.

Tracking tracer beads. The beads were tracked from videos acquired at 1.2 s time resolution using a Matlab code adapted from the code by Daniel Blair and Eric Dufresne https://site.physics.georgetown.edu/matlab/code.html. As the network is flowing inwards, we assumed that the inward-moving beads were transiently trapped within the network, whereas the outward-moving beads reflected the motion of the fluid phase within the droplets. To separately analyse the network movement and the fluid flow, the trajectories of the beads were classified as inward moving, outward moving or stationary based on thresholding the radial displacements over a 6 s time interval. Since the network flow was telescopic, the threshold was taken to be a linearly increasing function of the distance from the contraction centre (threshold = $0.005 \times r$). The instantaneous velocity of each bead was directly extracted from its trajectory and averaged over five consecutive frames. The radial profile of the velocity of the inward- and outward-moving beads as a function of distance from the contraction centre was determined by averaging the velocities of all the inward- and outward-moving beads detected within a concentric ring of width 1 µm at each radius (typically 1–5 beads). If there were no beads in a given frame and ring, the local velocity was set to NaN. The radial inward and outward velocity kymographs were then smoothed by convolving with a 2D Gaussian filter (ignoring NaN's) with $\sigma = 0.8$ s in the time domain and $\sigma = 2$ µm in the radial direction.

Analysis of contraction patterns. The spectral time-lapse (STL) images for different concentrations of added capping protein and calyculin (Fig. 5) were obtained using the STL algorithm[59]. The time-lapse images were masked with either a moments binary mask from Fiji or a manual intensity threshold, and time was colour-coded using the STL algorithm over 35–50 s as indicated, depending on the rate of network displacements.

Modelling

To model the actomyosin network, we used a system of transport (assembly, disassembly and drift) and force-balance (balancing myosin-generated contractile and crosslinked-actin viscous stresses) equations. These two partial differential equations, with boundary conditions specified in Supplementary Information, determine the network density and drift velocity, which are both functions of space and time. In the continuous model, the effective contractile stress and viscosity are functions of the network density as specified in Supplementary Information. We solved the model numerically, with parameters obtained from the data, in 1D and in a radially symmetric 2D case. We also simulated numerically a 1D stochastic agent-based model in which material nodes of the network appeared and disappeared at random times and locations with constant rates. Neighbouring node pairs did not interact if the distance between them was greater than the percolation length. They stayed at a constant distance from each other if this distance was less than the percolation length but greater than the contraction length, and they converged with a constant rate if their mutual distance was less than the contraction length. Further details are provided in Supplementary Information.

Reporting summary

Further information on the research design is available in Nature Portfolio Reporting Summary linked to this article.

Data availability

All the data used to support the findings of this paper are included in the plots and Supplementary Information. Any further details are available from K.K. upon request.

Code availability

The codes used for data analysis are publicly available as follows: Particle image velocimetry (PIV): https://github.com/nivieru/dropletsRhoV; Optical flow: https://ars.els-cdn.com/content/image/1-s2.0-S0006349516300339-mmc7.txt; Tracer bead tracking: https://site.physics.georgetown.edu/matlab/code.html; Spectral time-lapse (STL): https://zenodo.org/record/7663. The Matlab codes used for solving the 1D and 2D partial differential model equations as well as the the 1D discrete stochastic code are available at: https://github.com/mariyasavinov/SizeDependentWaves.git.

References

56. Field, C. M., Nguyen, P. A., Ishihara, K., Groen, A. C. & Mitchison, T. J. in *Methods in Enzymology*, Vol. 540 (ed. Vale, R. D.) 399–415 (Elsevier, 2014).
57. Abu-Shah, E., Malik-Garbi, M. & Keren, K. *Building a Cell from Its Component Parts* (eds Ross, J. & Marshall, W.) Ch. 15 (Elsevier, 2014).
58. Vig, D. K., Hamby, A. E. & Wolgemuth, C. W. On the quantification of cellular velocity fields. *Biophys. J.* **110**, 1469–1475 (2016).
59. Madan, C. R. & Spetch, M. L. Visualizing and quantifying movement from pre-recorded videos: the spectral time-lapse (STL) algorithm. *F1000Research* **3**, 19 (2014).

Acknowledgements

We thank L. Garion for the help with extract preparation. We thank M. Piel, R. Voituriez and Juan Manuel García-Arcos for stimulating discussions and sharing unpublished results. We thank J.-F.C. Joanny

for the helpful advice on the modelling. We thank P. Lenart, G. Bunin, A. Tayar, A. Frishman and S. Ro for comments on the paper. This work was supported by a grant from the United States–Israel Binational Science Foundation to K.K. and B. Goode (grant no. 2017158). M.S. and A.M. are supported by National Science Foundation grants DMS 1953430 and DMS 2052515.

Author contributions

A.K., N.I. and K.K. designed the experiments. A.K. and N.I. performed the experiments. A.K., N.I. and K.K. analysed the data. A.M., M.S., K.K. and A.K. developed the model. A.K., M.S., A.M. and K.K. wrote the paper. All co-authors discussed the results and commented on the paper.

Competing interests

The authors declare no competing interests.

Additional information

Extended data Extended data are available for this paper at https://doi.org/10.1038/s41567-023-02271-5.

Supplementary information The online version contains supplementary material available at https://doi.org/10.1038/s41567-023-02271-5.

Correspondence and requests for materials should be addressed to Alex Mogilner or Kinneret Keren.

Peer review information *Nature Physics* thanks Anne Bernheim-Groswasser, Patrick McCall and the other, anonymous, reviewer(s) for their contribution to the peer review of this work.

Supplementary Information

Size-dependent transition from steady contraction to waves in actomyosin networks with turnover

Ashwini Krishna, Mariya Savinov, Niv Ierushalmi, Alex Mogilner and Kinneret Keren

Supplementary Text

Continuous model

To model the actomyosin network, we turn to the basic transport (1) and force-balance (2) equations that have been used previously [1-4]:

$$\frac{\partial \rho}{\partial t} = \alpha - \beta\rho - \nabla \cdot \left(\vec{u}\rho\right) \quad (1)$$

$$\nabla \cdot \sigma = 0 \quad (2)$$

Here ρ is the network density, α is the assembly rate of the network, β is the disassembly rate, and $\vec{u}$ is the network velocity. The first equation is the mass conservation law for the drifting and turning over network. The velocity here is a dynamic variable that is a function of the spatial coordinate and time and must be found using Eq. 2. Also, the assembly and disassembly rates need not be constant and can be functions of the density.

In the second equation, σ is the total internal network stress tensor. Usually, the force balance equation is written in the form: $\nabla \cdot \sigma = \zeta \vec{u}$, where ζ is the effective drag between the network and the fluid in which the network is immersed. However, we demonstrated earlier [2, 3] that the friction between the network and fluid is much smaller than the effective contractile and internal viscous forces within the network, so we use the approximate Eq. 2 instead. For simplicity and in the absence of rheological measurements, we assume that the network is a very viscous isotropic Newtonian fluid [5], albeit compressible (which is obvious from the variable network density). To be clear, the combination of the network and solute that it is immersed in is incompressible, but by neglecting the solute fraction we may consider the network as a simple compressible fluid.

Thus, the components of the total stress tensor are:

$$\sigma_{ij} = \underbrace{\mu\left(\frac{\partial u_i}{\partial x_j} + \frac{\partial u_j}{\partial x_i}\right) - \left(\frac{2}{3}\mu - \lambda\right)\left(\nabla \cdot \vec{u}\right)\delta_{ij}}_{viscous} + \underbrace{\sigma_{contr}\delta_{ij}}_{contractile} \quad (3)$$

Here, the last term represents the active myosin-powered contraction, where the scalar σ_{contr} is the magnitude of the contractile stress. The other terms describe the passive stress of the actin network deformations. μ and λ are the effective shear and bulk viscosities, respectively. Taking the divergence of the total stress provides us with the force-balance equation:

$$\mu\nabla^2\vec{u} + \left(\frac{1}{3}\mu + \lambda\right)\nabla\left(\nabla \cdot \vec{u}\right) + \nabla\sigma_{contr} = 0 \quad (4)$$

The density dependencies of the viscosities and the contractile stress are crucial for large-scale network dynamics. A central feature of our model is the consideration of the coexistence of distinct mechanical regimes characterized by different viscosities and active stress in different regions of the system.

We adopt the state diagram from [6] in the following interpretation to describe the local state in each region (Fig. 3a). The state of the network in [6] is determined by two factors – connectivity and contractility. We make the following simplifications: 1) the connectivity is proportional to the local actin network density, ρ; 2) the contractile stress is an increasing function of the local myosin density; 3) the myosin density is an increasing function of the actin network density; 4) myosin kinetics is fast compared to actin turnover, meaning that the local myosin density adjusts rapidly to the local actin density. This fourth assumption allows us to describe the system by considering a single network density field. The behavior of the system is then restricted to a straight line (or a curve) on the state diagram (Fig. 3a) – passing through the unconnected (I), interconnected (II) and contractile (III) states, as this single density varies. This assumption is not necessarily true in our experimental system – myosin kinetics may not be fast – but qualitatively this would not change the system's behavior. The main point is that locally the system is in one of these three distinct mechanical states. Making the simplification of the fast myosin kinetics allows to consider only one density field explicitly (instead of two) and describe the local state of the system as a function of the local density.

We assume that the network in the unconnected state has zero viscosities and contractility, in the interconnected/non-contractile, state – non-zero viscosities and zero contractility, and in the interconnected/contractile state – non-zero viscosities and contractility. More specifically,

$$\mu = \begin{cases} 0 & \rho < \rho_{12} \\ \mu_0 & \rho > \rho_{12} \end{cases}, \lambda = \begin{cases} 0 & \rho < \rho_{12} \\ \lambda_0 & \rho > \rho_{12} \end{cases}, \sigma_{contr} = \begin{cases} 0 & \rho < \rho_{23} \\ \sigma_0 & \rho > \rho_{23} \end{cases} \quad (5)$$

where ρ_{12} and ρ_{23} are the density thresholds for interconnectedness and contractility, respectively (Fig. 3a) and $\rho_{12} < \rho_{23}$. Note that we assume that above the interconnected/contractile threshold, the viscosities and contractility are constants. This assumption is not crucial, but greatly simplifies the model. This density independence also leads to the telescopic character of the contraction [2]: the inward velocity increases almost linearly as a function of the distance from the contraction center. Note also that from now on, the force balance equations are applicable only to the interconnected network, for $\rho > \rho_{12}$. Wherever $\rho < \rho_{12}$, the velocity is equal to zero, and the transport equation becomes an ordinary differential equation as a function of time.

We discuss the boundary conditions for the model in detail below; here, we mention briefly that the boundary conditions for the force balance equation (Eq. 4) are: 1) zero velocity at the inner boundary of the interconnected network (at the boundary of the aggregate / exclusion zone that forms at the contraction center [3]); 2) zero normal component of the total stress (Eq. 3) at the outer boundary of the interconnected network.

We consider two geometries: 1) one-dimensional (1D) or, 2) radially symmetric two-dimensional (2D). In the 1D case, the force balance equation after integration simply states that the total internal network stress tensor is equal to a constant. Because of the boundary condition of zero total stress at the outer boundary of the network, this constant is equal to zero. Thus, in 1D, Eqs. 1 and 4 reduce to:

$$\frac{\partial \rho}{\partial t} = \alpha - \beta\rho - \frac{\partial}{\partial x}(u\rho) \quad (6)$$

$$\eta_0 \frac{\partial u}{\partial x} + \sigma_{contr} = 0 . \quad (7)$$

Here $\eta_0 = \frac{4}{3}\mu_0 + \lambda_0$ is the effective viscosity coefficient in the 1D model, x is the 1D coordinate, u is the 1D network velocity.

For $\rho > \rho_{23}$, Eq. 7 becomes: $\frac{\partial u}{\partial x} = -k \rightarrow u = u_0 - kx$, where u_0 is a constant and $k = \frac{\sigma_0}{\eta_0}$. The parameter k is the observable contraction rate. In the unconnected phase, the velocity is simply equal to zero. In the interconnected/non-contractile state, $\rho_{12} < \rho < \rho_{23}$, where the viscosity is non-zero but the contractility is zero, Eq. 7 becomes: $\frac{\partial u}{\partial x} = 0 \rightarrow u = u_0$. To summarize, the 1D model becomes:

$$\frac{\partial \rho}{\partial t} = \alpha - \beta\rho - \frac{\partial}{\partial x}(u\rho), u = \begin{cases} 0 & \rho < \rho_{12} \\ const & \rho_{12} < \rho < \rho_{23} \\ const - kx & \rho > \rho_{23} \end{cases} \quad (8)$$

The constants are found from the boundary condition near the center of the droplet, $u(0) = 0$, and the condition of the continuity of the velocity.

For example, when $\rho > \rho_{23}$ at $0 < x < r_{23}$, $\rho_{12} < \rho < \rho_{23}$ at $r_{23} < x < r_{12}$, and $\rho_{12} > \rho$ at $r_{12} < x < R$ (where r_{23} and r_{12} are defined such that $\rho(r_{23}) = \rho_{23}$ and $\rho(r_{12}) = \rho_{12}$, respectively), then $u = -kx$ at $0 < x < r_{23}$, $u = -kr_{23}$ at $r_{23} < x < r_{12}$, and $u = 0$ at $r_{12} < x < R$. In principle, there could be multiple regions of interspersed contractile and interconnected/non-contractile network (see the general formulas for the 2D case below). In these cases, the extension of Eq. 8 is straightforward.

In 2D, for the radially symmetric case, the transport equation becomes:

$$\frac{\partial \rho}{\partial t} = \alpha - \beta\rho - \frac{1}{r}\frac{\partial}{\partial r}(ru\rho), \quad (9)$$

while the force balance equation is:

$$\mu_0\left(\frac{1}{r}\frac{\partial}{\partial r}\left(r\frac{\partial u}{\partial r}\right) - \frac{u}{r^2}\right) + \left(\frac{\mu_0}{3} + \lambda_0\right)\frac{\partial}{\partial r}\left(\frac{1}{r}\frac{\partial (ru)}{\partial r}\right) + \frac{\partial \sigma_0}{\partial r} = 0 . \quad (10)$$

Here r is the radial coordinate in a polar coordinate system (centered at the center of the exclusion zone within the droplet), and $u(r,t)$ is the radial component of the velocity. The radial component of the stress tensor in this case has the form:

$$\sigma_{rr} = 2\mu_0 \frac{\partial u}{\partial r} - \left(\frac{2}{3}\mu_0 - \lambda_0\right)\frac{1}{r}\frac{\partial}{\partial r}(ru) + \sigma_0 . \quad (11)$$

In 2D, as the active stress is assumed to be piece-wise constant, $\sigma_{contr} = const$ if $\rho \neq \rho_{12}, \rho_{23}$, the force balance (Eq. 10) within each region becomes:

$\mu_0\left(\frac{1}{r}\frac{\partial}{\partial r}\left(r\frac{\partial u}{\partial r}\right)-\frac{u}{r^2}\right)+\left(\frac{\mu_0}{3}+\lambda_0\right)\frac{\partial}{\partial r}\left(\frac{1}{r}\frac{\partial(ru)}{\partial r}\right)=0$. Simple calculations allow to re-write the left-hand side in a particularly convenient form: $\eta_0\left(\frac{\partial^2 u}{\partial r^2}+\frac{1}{r}\frac{\partial u}{\partial r}-\frac{u}{r^2}\right)=0$, where $\eta_0=\frac{4}{3}\mu_0+\lambda_0$. The general solution of this equation has the form: $u=ar+b/r$, where a and b are arbitrary constants (for any given time moment) to be found from the boundary conditions. This general form of the velocity profile is applicable both in the contractile $\rho>\rho_{23}$ and in the interconnected/non-contractile $\rho_{12}<\rho<\rho_{23}$ states. In the unconnected phase the velocity is simply zero. Substituting this expression for the radial velocity into Eq. 11, we obtain the general formula for the radial stress:

$\sigma_{rr}=\left(\frac{2\mu_0}{3}+2\lambda_0\right)a-2\mu_0 b/r^2+\sigma_0$.

To summarize, the 2D model becomes:

$$\frac{\partial\rho}{\partial t}=\alpha-\beta\rho-\frac{1}{r}\frac{\partial}{\partial r}(ru\rho),\quad u=\begin{cases}0 & \rho<\rho_{12}\\ (const)r+const/r & \rho_{12}<\rho<\rho_{23}\\ (const)r+const/r & \rho>\rho_{23}\end{cases}\qquad(12)$$

Note that the constants in the expression for the velocities are different in each region (as described below, they are determined by stitching the results in the different regions while taking into account the boundary conditions).

Here are the remaining model assumptions and boundary conditions, after which the particular solution for the 2D velocity profile is outlined further:

1. A boundary condition for the velocity: $u(0)=0$ in 1D or $u(r_0)=0$ in 2D, meaning that at its innermost boundary (of the exclusion zone) the network sticks to the aggregate that forms at the contraction center [3].
2. A second boundary condition: no-stress at the outer interconnected network boundary $x=r_{12}$ in 1D or $r=r_{12}$ in 2D, where r_{12} is the point at which the interconnected network ends (so that $\rho(r_{12})=\rho_{12}$). This is already applied in Eq. 8 for 1D. In 2D, this appears as zero radial stress at the outer interconnected network boundary: $\sigma_{rr}(r_{12})=0$.
3. A continuity condition for the velocity: $u(x)$ in 1D or $u(r)$ in 2D are continuous functions for $\rho>\rho_{12}$. Additionally, in 2D, a continuity condition for the radial stress: $\sigma_{rr}(r)$ is a continuous function for $\rho>\rho_{12}$. In 2D, this boundary condition, namely the continuity condition for the velocity, looks very natural mathematically. However, it is not the only possible boundary condition from a physical viewpoint. Consider, for example, a situation in which the inner interconnected/non-contractile network is static; with this continuity condition a contractile ring enveloping the non-contractile network would not be able to contract, as its centripetal velocity at the interface with the static non-contractile network has to be zero. Physically, this means that the non-contractile network mechanically resists contraction, and the centripetal wave movement is limited by the rate at which the actin density grows and non-contractile network becomes contractile. Below, we examine a different boundary condition which allows the contractile ring to contribute to the centripetal wave.

4. At the outer boundary of the interconnected network ($\rho = \rho_{12}$), if this network is not in contact with the droplet's edge, the network boundary grows at constant rate equal to v_0. Mathematically, the boundary moves with a velocity: $u(x) + v_0$ in 1D or $u(r) + v_0$ in 2D for x and r such that $\rho(x) = \rho_{12}$ or $\rho(r) = \rho_{12}$, respectively. Physically, the growth of the network boundary can be explained by the polymerization and elongation of filaments connected to the network at the edge of the network.
5. α, the network assembly rate, is assumed to be density dependent, so that the rate saturates to a constant at larger densities and decreases to a smaller constant at lower densities. Such density dependent assembly could arise e.g., from the contribution of autocatalytic, Arp2/3-dependent assembly [7]. We use the expression: $\alpha = \alpha_0 + (\bar{\alpha} - \alpha_0)(1 - \exp(-\rho / \rho_0))$. The density dependency of the assembly rate is not critical. Qualitatively, the model works well without this assumption, but the results are more numerically robust with the assumed density dependence.
6. β, the network disassembly rate, is assumed to be a density-independent, scalar, which agrees with the fit to the data in our previous study [2]. Simulations showed that the model-predicted behavior is insensitive to the disassembly rate becoming a linearly increasing function of density (which could be the case due to myosin-driven disassembly).
7. We solve the equations in 1D on the domain $0 < x < R$, where R is the droplet radius, and in 2D on $r_0 < r < R$.
8. In point 4 above, we assume that at the boundary between the interconnected network and the unconnected 'gas'-like phase, the network grows with the free polymerization rate v_0. However, when the interconnected network is in contact with the droplet's edge, the physics changes: the polymerization is against a physical boundary (the water-oil interface). We make the simplest assumption – that filaments pushing against this physical boundary generate a force which is too small to overcome the effective Darcy friction between the network and fluid (and this friction by itself is neglected compared to internal stresses in the network). Thus, the tips of the filaments remain in contact with the droplet's edge, so the growth rate of the network boundary against the droplet's boundary is not v_0, but a variable that perfectly balances the centripetal network's flow.

The particular solution for the velocity profile in 2D depends on the breakdown of the domain $r_0 < r < R$ into the different regimes: contractile, interconnected/non-contractile, and unconnected. We consider the solution in the part of the domain where $r_0 < r < r_{12}$, having defined r_{12} as the first point from $r = r_0$ where $\rho \leq \rho_{12}$ (the first point where the network is no longer connected). In principle, there can be a situation in which two interconnected and/or contractile network regions are separated by an unconnected region. In that case, one must analyze each interconnected region separately. In our simulations, we encountered cases in which an interconnected but not contractile network is separated by an unconnected region from another interconnected and contractile region. In this case, the situation is simple: the velocity in the interconnected/non-contractile region, separated by the unconnected region from the contractile network, is equal to zero. The analysis becomes nontrivial if there are multiple contractile networks separated by unconnected networks. In our simulations, we have not encountered such cases, and so we omit such analysis here.

We consider the case of one interconnected domain $r_0 < r < r_{12}$. We divide this domain into regions with distinct mechanical states. In region i ($i = 1, 2, \ldots, n$), which includes the part of the domain $r^{i-1,i} \leq r < r^{i,i+1}$, the velocity profile is $u_i(r) = a_i r + b_i/r$. Note that when $i = 1$, $r^{0,1} = r_0$ and when $i = n$, $r^{n,n+1} = r_{12}$. Numerical solutions show that region $i = 1$ is always contractile, as the density is always greater than ρ_{23} near the inner boundary of the domain.

The linear system for the coefficients $\{a_i, b_i\}_{i=1}^{n}$ (total $2n$-many) requires $2n$ equations to be solved. Two come from the boundary conditions:

$$u_1(r_0) = a_1 r_0 + b_1/r_0 = 0 \tag{13}$$

(zero velocity at the inner boundary) and

$$\sigma_{rr}\left(r_{12}\right) = 0 = \begin{cases} \left(\frac{2\mu_0}{3} + 2\lambda_0\right) a_n - 2\mu_0 b_n / r_{12}^2, & n \text{ even} \\ \left(\frac{2\mu_0}{3} + 2\lambda_0\right) a_n - 2\mu_0 b_n / r_{12}^2 + \sigma_0, & n \text{ odd} \end{cases} \tag{14}$$

(no radial stress at the outer boundary). Note that when n is even, the final region is non-contractile and when n is odd, the final region is contractile.

The remaining equations come from the continuity conditions applied across each point $r^{i,i+1}$. For each $i = 1, 2, \ldots, n-1$, velocity continuity requires that

$$a_i r^{i,i+1} + b_i/r^{i,i+1} = a_{i+1} r^{i,i+1} + b_{i+1}/r^{i,i+1} \tag{15}$$

and continuity of σ_{rr} requires that

$$\begin{cases} \left(\frac{1}{3} + \frac{\lambda_0}{\mu_0}\right) a_i - b_i / \left(r^{i,i+1}\right)^2 = \left(\frac{1}{3} + \frac{\lambda_0}{\mu_0}\right) a_{i+1} - b_{i+1} / \left(r^{i,i+1}\right)^2 + k, & i \text{ even} \\ \left(\frac{1}{3} + \frac{\lambda_0}{\mu_0}\right) a_i - b_i / \left(r^{i,i+1}\right)^2 + k = \left(\frac{1}{3} + \frac{\lambda_0}{\mu_0}\right) a_{i+1} - b_{i+1} / \left(r^{i,i+1}\right)^2, & i \text{ odd} \end{cases} \tag{16}$$

Here $k = \sigma_0 / 2\mu_0$ is the approximate contraction rate for the 2D model (which turns out to be the same as that in the 1D case; see below). These make up in total the $2n$ equations necessary to solve for the $2n$-many coefficients for the piece-wise continuous velocity profile. Numerical solutions demonstrate two interesting features of this system (see Supplementary Video 13 and snapshots from the simulations in Fig. 3): 1) in the interconnected/non-contractile regions, the velocity profile is relatively close to being flat. 2) in the contractile regions, the velocity profile is relatively close to being linear, with a slope equal to $k = \sigma_0 / 2\mu_0$ multiplied by two factors, both of which are on the order of unity. The first factor is a function of the two viscosities, λ_0 and μ_0 (it is of order unity if λ_0 and μ_0 are of the same order of magnitude). In what follows, we consider a specific case that gives the simplest result and choose $\lambda_0 = \frac{2}{3}\mu_0$. Then, the factor $\left(\frac{1}{3} + \frac{\lambda_0}{\mu_0}\right)$ in Eq. 16 and in the first factor for the contraction rate become equal to unity. In this specific case, also $\eta_0 = 2\mu_0$, and the contraction rates in 1D and 2D are defined in the same way. The second factor is geometric, explained in the following example:

Suppose there are only two regions: a contractile regime for $r_0 \le r < r_{23}$ and a connected regime for $r_{23} \le r < r_{12}$ (with the remainder of the domain being unconnected). The velocity profile, for the case where $\lambda_0 = \frac{2}{3}\mu_0$, is:

$$u(r) = \begin{cases} a_1 r + b_1/r, & r_0 \le r < r_{23} \\ a_2 r + b_2/r, & r_{23} \le r < r_{12} \end{cases}$$

The linear system outlined previously can be solved to yield the unique coefficient solution:

$$a_1 = -\frac{k}{2}\left(\frac{r_{12}^2 + {r_{23}}^2}{r_0^2 + r_{12}^2}\right), \qquad b_1 = +r_0^2 \frac{k}{2}\left(\frac{{r_{23}}^2 + r_{12}^2}{r_0^2 + r_{12}^2}\right)$$

$$a_2 = +\frac{k}{2}\left(\frac{r_0^2 - {r_{23}}^2}{r_0^2 + r_{12}^2}\right), \qquad b_2 = +r_{12}^2 \frac{k}{2}\left(\frac{r_0^2 - {r_{23}}^2}{r_0^2 + r_{12}^2}\right)$$

Interestingly, since r_0 is small compared to *R*, generally b_1 will also be small – so the velocity profile in the contractile regime is nearly linear (moreover, exactly linear as $r_0 \to 0$). Numerical solutions confirm that this is the general case in our system. Thus, a_1 is the contraction rate. Note that it is equal to k multiplied by the geometric factor $\frac{1}{2}\left(\frac{r_{12}^2 + {r_{23}}^2}{r_0^2 + r_{12}^2}\right)$. As $r_0^2 \ll r_{12}^2$, and usually $r_{12}^2 \sim {r_{23}}^2$, this factor is on the order of unity. This turns out to be the case in general. In the numerical simulations in 2D, we use the exact expressions for the velocity profile obtained from the solutions of Eqs. 13-16 for the case where $\lambda_0 = \frac{2}{3}\mu_0$

We scale the model equations as follows. The droplet's radius, R, provides a natural length scale; the turnover time, $1/\beta$, is the natural time scale; and the natural density scale is $\bar{\alpha}/\beta$. We solve the model equations numerically after non-dimensionalizing the model by using these scales. In 1D, the non-dimensional model becomes (using the same notations we had for the dimensional variables for the non-dimensional ones):

$$\frac{\partial \rho}{\partial t} = \left(\varepsilon + \left(1-\varepsilon\right)\exp\left(-\rho/\rho_0\right)\right) - \rho - \frac{\partial}{\partial x}\left(u\rho\right); u = \begin{cases} 0 & \rho < \rho_{12} \\ const & \rho_{12} < \rho < \rho_{23} \\ const - kx & \rho > \rho_{23} \end{cases} \tag{17}$$

and in 2D:

$$\frac{\partial \rho}{\partial t} = \left(\varepsilon + \left(1-\varepsilon\right)\exp\left(-\rho/\rho_0\right)\right) - \rho - \frac{1}{r}\frac{\partial}{\partial r}\left(ru\rho\right); u = \begin{cases} 0 & \rho < \rho_{12} \\ \left(const\right)r + const/r & \rho_{12} < \rho < \rho_{23} \\ \left(const\right)r + const/r & \rho > \rho_{23} \end{cases} \tag{18}$$

The model has six non-dimensional parameters (for which we retain the same notations as for the dimensional parameters):

$\beta \underbrace{\rho_{12}}_{\text{dim}} / \bar{\alpha} \to \underbrace{\rho_{12}}_{\text{non-dim}}$ is the gas-connected threshold density (boundary between states I and II);

$\beta \underbrace{\rho_{23}}_{\text{dim}} / \bar{\alpha} \to \underbrace{\rho_{23}}_{\text{non-dim}}$ is the connected-contractile threshold density (between states II and III);

$\underbrace{k}_{\text{dim}} / \beta \to \underbrace{k}_{\text{non-dim}}$ (where dimensional parameter $k = \sigma_0/\eta_0$) is the contraction rate;

$\underbrace{\varepsilon}_{\text{dim}} / \bar{\alpha} \to \underbrace{\varepsilon}_{\text{non-dim}}$ is the low-density gas assembly rate;

$\underbrace{\rho_0}_{\text{dim}}\beta/\bar{\alpha}\to\underbrace{\rho_0}_{\text{non-dim}}$ is the density parameter at which the low assembly rate turns into high one;

$\underbrace{v_0}_{\text{dim}}/(R\beta)\to\underbrace{v_0}_{\text{non-dim}}$ is the effective growth rate of the percolated network boundary.

We solve the model drift-reaction equations numerically using standard numerical methods [8]. The results are relatively robust to variations of the model parameters. Specifically, we fix several non-dimensional parameters: $\varepsilon=0.1$, $\rho_0=0.5$, $\rho_{12}=0.1$, $\rho_{23}=0.6$. The rationale for these choices is as follows: as mentioned above, the density dependence of the assembly rate is not critical, but a reduction in assembly at low density benefits the robustness of the results: the slower assembly ensures that the contractile density is not reached prematurely before the network interconnects globally, hence the smallness of parameter ε. We want the assembly rate to saturate to a constant at relatively low densities, comparable to the characteristic density scale, hence the choice of parameter ρ_0. Our previous results [2] indicate that the network is interconnected at relatively low densities, so we chose parameter ρ_{12} to be small. We are assuming that the network becomes contractile at densities comparable to the characteristic density scale, which means choosing parameter ρ_{23} on the same order of magnitude as that of parameter ρ_0. Varying the system size in the non-dimensionalized model is equivalent to changing v_0, which is inversely proportional to the radius. To study the behavior of the model as a function of the contraction rate and system size, we thus varied the remaining model parameters, k and v_0. The results (Fig. 3), indicate that at small contraction rates and droplet's radii (i.e. larger v_0), the density and velocity evolve to yield stable steady distributions, while at greater contraction rates and droplet's radii, periodic waves emerge. The model displays an instability at very high contraction rates (k on the order of 5 and above), which are indicative of the local contractile instabilities that are discussed in detail below. The simulations predict that the centripetal velocity has telescopic character – the velocity of the wave crest is a roughly linear function of the radial distance.

We can numerically solve the same model equations in 1D, to emulate the effective 1D conditions in flat, elongated capillaries or along cylindrical shells. The numerical 1D solutions (Fig. S9) are qualitatively similar to the 2D model solutions shown in Fig. 3, with some minor changes in the velocity and density profiles. Importantly, these results show that unlike the contractile ring model (see below), our model can adequately explain the periodic contraction observed in flat capillaries (Fig. S2; Supplementary Video 4) and in the cylindrical cortex of motile cells [9]. In 1D, the stress is just $\sigma = (4\mu/3 + \lambda)\, du/dx + \sigma_{contr}$. This yields a governing equation in 1D which is just $d^2u/dx^2 + d\sigma_{contr}/dx = 0$ that has general solution $u(x) = ax + b$ when σ_{contr} is a constant. Then, the scalar stress in 1D is $\sigma = (4\mu/3 + \lambda)\, a + \sigma_0$. The solution for the velocity profile in the 1D case is simple – in contractile regimes, $u = -kx + c$, where c is some constant and $k = \sigma/(4\mu/3 + \lambda)$. In connected, non-contractile regimes, the velocity is just a constant. Recall that we also require that the velocity profile is continuous in connected regimes, the velocity is zero at x = 0, and stress is zero at the free boundary of the connected network. Necessarily, the stress must be zero both in the contractile regime, and in the connected, non-contractile regime. The main difference is that in the contractile regimes, a nonzero viscous stress identically balances the nonzero contractile stress. Fig. S9 shows how this would look throughout the wave cycle.

Analytical estimates for the transition length

We can make the following useful rough estimates (in 1D, but they work in 2D as well). Let us consider the case of the steady flow in a relatively small droplet of a certain radius (to be estimated), for which the free boundary of the interconnected network is exactly at the droplet's boundary. We will call the special radius at which this condition is achieved R_{tr}, and show below that it is equal to the transition length above which we obtain periodic waves. The network density is decreasing with distance away from the droplet's center (x=0). The centripetal velocity profile for this case is such that the velocity increases linearly from the x=0 to a distance r_{23}, where the density reaches the threshold contractile density: $\rho\left(r_{23}\right)=\rho_{23}$. In the region $x<r_{23}$, where the density is above the contractile threshold, the centripetal velocity profile has a slope equal to the contraction rate k, and so the centripetal velocity there is equal to $v=kx$ (with a negative sign, directed to the left), and the maximal value of the centripetal speed is reached at $x=r_{23}$ and is equal to $v_{\max}=kr_{23}$. At greater distances, $x>r_{23}$, the velocity plateaus: $v\left(x\right)=v_{\max}=kr_{23}$, because at such distances, the network is interconnected but does not contract.

If the free boundary of the interconnected network is stationary and positioned exactly at the droplet's boundary $x=R_{tr}$, two conditions must be satisfied at that boundary: first, the density there has to be equal to the threshold interconnected density, $\rho\left(R_{tr}\right)=\rho_{12}$. Second, the centripetal network velocity there has to exactly balance the growth rate of the network: $v_{\max}=v_0$. Thus, $v_{\max}=kr_{23}=v_0$, and as such $r_{23}=v_0/k$. Let us now find the network density profile in the interval $r_{23}<x<R_{tr}$. The equation for the density there is: $\frac{\partial\rho}{\partial t}=\alpha-\beta\rho+v_{\max}\frac{\partial\rho}{\partial x}$. For simplicity, we will neglect the density dependence of the assembly rate and consider it constant. Also, in this outer region the density is well below the equilibrium density α/β, so the disassembly term in the density equation can be approximately neglected: $\frac{\partial\rho}{\partial t}\approx\alpha+v_{\max}\frac{\partial\rho}{\partial x}$. At steady state, $\alpha+v_{\max}\frac{d\rho}{dx}=0$, thus $\frac{d\rho}{dx}=-\frac{\alpha}{v_{\max}}$. Considering that $\rho\left(r_{23}\right)=\rho_{23}$, after integrating, we have: $\rho=\rho_{23}-\frac{\alpha}{v_{\max}}\left(x-r_{23}\right)$. We use $\rho\left(R_{tr}\right)=\rho_{12}$ to obtain the following formula: $\rho_{12}=\rho_{23}-\frac{\alpha}{v_{\max}}\left(R_{tr}-r_{23}\right)$. This formula then allows us to calculate the special droplet's radius R_{tr}:

$R_{tr}=r_{23}+\frac{v_{\max}}{\alpha}\left(\rho_{23}-\rho_{12}\right)$. Considering that $v_{\max}=kr_{23}=v_0$, $r_{23}=v_0/k$, this equality can be rewritten as $R_{tr}=\frac{v_0}{k}+\frac{v_0}{\alpha}\left(\rho_{23}-\rho_{12}\right)$. Finally, based on the assumption that $\rho_{23}>>\rho_{12}$ and $\rho_{23}=c\frac{\alpha}{\beta}$, where c is a dimensionless number on the order of unity, we arrive at the very useful estimate:

$R_{tr} = \frac{v_0}{k} + c\frac{v_0}{\beta}$. This estimate predicts that the transition radius R_{tr} is inversely proportional to the contraction rate k and is proportional to the free boundary growth rate v_0 of the interconnected network. Fig. 3e shows that the numerical estimate of the transition radius exhibits the predicted scaling.

Let us now show that the transition length, R_{tr}, estimated above is the characteristic length scale separating the steady contracting flow from the periodic contraction waves. First, we show that if the droplet's radius is smaller than the transition radius, $R < R_{tr}$, then a steady centripetal flow persists. Simulations show that the smaller the droplet, the closer the contractile boundary, r_{23}, is to the droplet's center. This means that the maximal centripetal velocity, equal to kr_{23}, is smaller than v_0 in such droplets, and so the free interconnected network boundary is propped up against the droplet's boundary and is able to grow as fast as the centripetal retraction and to keep at the boundary. On the other hand, if the droplet's radius is greater than the transition radius, $R > R_{tr}$, then the contractile boundary moves farther away from the droplet's center. This means that the maximal centripetal velocity, equal to kr_{23}, is greater than v_0 in such droplets, and so the free interconnected network boundary moves inward. As soon as the retreating interconnected network boundary leaves a gap between its edge and the droplet's boundary, the unconnected network fragments start to appear in this gap. Their density grows, until the interconnected density is achieved, and then after a finite time, a new centripetal drift begins, generating periodic contraction waves. Simulations confirm this intuition (Fig S10, Supplementary Video 14).

Period of the pulsatile contraction

The period of the wave is on the order of the turnover time, $\sim 1/\beta$, which is clear from the simulations: after the previous wave of contraction moves centripetally from the periphery, there is a waiting period until the next pulse of contraction equal to the time needed to assemble the network density equal to the critical density threshold. This waiting period is equal to a fraction of the equilibrium density $\sim \alpha/\beta$ divided by the assembly rate: $\sim (\alpha/\beta)/\alpha \sim 1/\beta$. Numerical simulations show that the wave period is weakly dependent on the droplet's radius (Fig. S11), as observed experimentally under most conditions (Fig. S7).

These estimates and numerical results are further supported by simulations with decreasing actin assembly rates (Fig. S12), designed to mimic the experiments with high concentration with phalloidin (Fig. 2g,h). In these experiments, filamentous actin is slowly taken out of the circulation (due to binding of phalloidin to filaments, which inhibits their disassembly), which is best modeled by a gradual decrease of the assembly rate with time. When we simulated this case, we found that the time intervals between the consecutive waves increase, because each cycle it takes longer to reach the threshold contractile density (Fig. S12). The result compares well with the experimental data reported in Fig. 2g,h, supporting our understanding that the wave period is primarily dependent on the characteristic time for network assembly.

In the presence of added Capping protein that limits filament growth, the filaments become shorter [10]. The discrete model suggests that there are local instabilities because connectivity is lower due to shorter

filaments, as seen experimentally (Fig. 4). Individual asters form and contract locally, delaying the development of a globally interconnected network. The larger the droplet, the more these local delays accumulate, likely accounting for the more prominent dependence of the period on the size of the droplet observed in experiments with Capping protein (Fig. S7).

Note on dimensional parameters and their dependence on biochemical conditions

Above, we discussed the non-dimensional model parameters. The corresponding dimensional parameters are as follows. The disassembly rate β was measured in our previous study [2]; it is on the order of inverse few minutes. The assembly rate α, same as characteristic network density $\rho \sim \alpha / \beta$, can only be measured in arbitrary units (see [2]), but their dimensional values do not affect the model behavior, assuming that the percolation and contractile thresholds are not too small and not too great fractions of the ratio α / β. The polymerization rate v_0, which agrees with the model predictions, is on the order of tenths of micron per second, which is the order of magnitude widely reported in the literature. Lastly, the contraction rate k which is experimentally measured, is on the order of inverse few minutes. The contraction rate is given by the ratio of the contractile stress and actin network viscosity. The contractile, myosin-powered, stress varies from $\sim$ 1 Pa to kPa [11].This would mean that effective viscosity is on the order of 0.01 to 10 Pa$\times$s, comparable to values reported in the literature [12, 13].

The contraction rate k, the transition length R_{tr}, and the wave period T can be directly measured, whereas the free boundary growth rate v_0 cannot. Based on the data for the four different biochemical conditions reported in Fig. 2, the most interesting conclusion is that if we calculate the product $R_{tr} \times k$, we find that this product is remarkably robust, barely changing between the conditions (Fig. 2e). According to the model, $v_0 \sim R_{tr} \times k$, thus we conclude that rate v_0 is insensitive to the biochemical perturbations, which makes sense because the polymerization rate depends on little else but actin and profilin concentrations, which were not varied. Thus, we just need to explain dependence of the contraction rate k on the biochemical conditions; the transition length R_{tr} is simply on the order of v_0 / k according to the model. The contraction rate k is the ratio between the contractile stress and network viscosity. The contractile stress depends on the actin architecture, but in a crude approximation, viscosity could be even more sensitive to the actin architecture. If so, the data can be understood as follows: network connectivity decreases with increasing Capping protein concentration, so lower viscosity explains much higher k in this case. Higher mDia concentration likely means longer, more overlapping, filaments, as formin compete with Capping protein, and so the viscosity goes up and k goes down in this case. Finally, adding ActA increases the actin nucleation rate and generates branched structures, increasing entanglement and viscosity, which leads to a dramatic slowing down of the contraction rate k.

Contractile ring model

One distinct possibility suggested in [10] is that a cortex-like actomyosin shell assembles near the boundary of the droplet and when the shell becomes contractile, it shrinks centripetally like a contractile ring in dividing cells. Here, we consider a radially symmetric 2D model that shows this contractile ring behavior. This model (we refer to it in this section as the contraction ring model), is exactly the same as the model outlined above and used to produce the simulations for the main text

(which we refer to in this section as the main model), apart from one different boundary condition. Specifically, the model equations in both models are identical, describing a contracting network that experiences both tangential and radial stresses, which arise from a combination of viscous and contractile stresses, and undergoes turnover. However, we use a different boundary condition at the interface between the contractile and interconnected/non-contractile network (for brevity, in this section we refer to the latter as simply interconnected). This interface normally appears at the inner boundary of the contractile band, and as detailed below, this different boundary condition leads to a different physical behavior in the two cases. In the main model, we use the velocity continuity condition. This boundary condition effectively means that the interconnected network resists both compression and stretch by the contractile network. This, for example, will drastically slow down the contraction of a ring enveloping the interconnected network in 2D and 3D. However, exactly the same condition allows for the convergence of a flat contractile band to the center in 1D. In the contractile ring model, we explore a different boundary condition: zero radial stress at the inner and outer surfaces of the contractile ring. This means that the interconnected network does not resist either compression or stretch by the contractile ring. In particular, when contractile ring moves centripetally, it sweeps the interconnected network in its way and incorporates it into the contractile network inside the ring. Note, however, that such boundary condition in 1D would not allow the contractile band to contract toward the contraction center, without interacting with the interconnected network, which would preclude periodic contraction in 1D. Below, we analyze the stresses in the contractile ring, then compute the density, width and velocity of the ring, and lastly predict its dynamics over time.

Stresses: Our force balance equation is $\nabla \cdot \boldsymbol{\sigma} = 0$ where the stress tensor $\boldsymbol{\sigma}$ is, $\boldsymbol{\sigma} = \mu(\nabla u + \nabla u^T) - (2\mu/3 - \lambda)\nabla \cdot \mathbf{u}\,\mathbf{I} + \sigma_{contr}\,\mathbf{I}$. In 2D cylindrical coordinates with radial symmetry, the non-diagonal components of the stress tensor are zero, $\sigma_{\theta r} = \sigma_{r\theta} = 0$, while the diagonal components are:

$\sigma_{rr} = 2\mu(\partial u/\partial r) - (2\mu/3 - \lambda)(1/r)\partial/\partial r(ru) + \sigma_{contr}$, $\sigma_{\theta\theta} = 2\mu(u/r) - (2\mu/3 - \lambda)(1/r)\partial/\partial r(ru) + \sigma_{contr}$.

In this case, the force balance equation $\nabla \cdot \sigma = 0$ becomes:

$(4\mu/3 + \lambda)(\partial^2 u/\partial r^2) + (4\mu/3 + \lambda)[(1/r)\partial u/\partial r - u/r^2] + \partial\,\sigma_{contr}/\partial r = 0$,

where the second term is the contribution from the tangential part of the stress. This equation has the following general solution for the velocity: $u = ar+b/r$, and corresponding radial and tangential stresses become: $\sigma_{rr}(r) = (2\mu/3 + 2\lambda)a - 2\mu b/r^2 + \sigma_0$, $\sigma_{\theta\theta} = (2\mu/3 + 2\lambda)a + 2\mu b/r^2 + \sigma_0$. We found that in the case of a contractile ring: $u(r) = (2\mu/3 + 2\lambda)^{-1}(\sigma_0 r)$. As a result, the radial and tangential components *of the total stress* are both zero: $\sigma_{rr} = \sigma_{\theta\theta} = 0$. (Since $b = 0$, there is no difference between σ_{rr} and $\sigma_{\theta\theta}$). In this case, the contractile stresses in the tangential and radial directions are both equal to σ_0 and the viscous stresses in both directions are equal to σ_0. We plot the stresses in (Figs. S13).

Velocity and width of the contractile ring: We use zero radial stress boundary condition at both inner and outer boundaries of the contractile ring. Physically, this means that the contractile band, moving centripetally, effortlessly "consumes", or "collects" all the interconnected network on its way, without any resistance. In this case, the formulas for the radial stresses at the inner and outer boundaries of the ring (R_1 and R_2, respectively), for the general velocity distribution inside the ring, $u = ar+b/r$, have the form: $\sigma_{rr}(R_1) = Aa - Bb/R_1^2 + \sigma_0 = 0$, $\sigma_{rr}(R_2) = Aa - Bb/R_2^2 + \sigma_0 = 0$, where A and B are constants. The only way both expressions for the stress can be true, regardless of the width of the peak, is if $B = 0$. Then, the specific solution for the velocity inside the contractile ring is: $u(r) = [\sigma_0/(2\mu/3 + 2\lambda)]r$ for $R_1 < r < R_2$. Thus, we established that the contractile ring moves centripetally with velocity linearly proportional to its radius, $u = -kr$.

Kinetics of the interconnected network inside the contractile ring: Because of this centripetal velocity character, movement of the outer boundary of the contractile ring is described by the equation d R_2/dt = -k R_2, and assuming the wave starts from the droplet's boundary, $R_2(t)$ = Rexp(-kt). Now we can determine the density profile of the network behind the wave, with simplifying assumptions that the assembly rate is constant and that the interconnected network is stationary. Then, the equation for the density, $\partial\rho / \partial t = \alpha - \beta\rho$, has the solution: $\rho(t,r) = (\alpha/\beta)\left[1 - exp\left(\beta\left(T(r) - t\right)\right)\right]$. Here $T(r)$ is the time when the density at radius r is zero. $T(r)$ is determined by the time when the outer boundary of the previous wave was at this location, i.e. r = $R_2(t)$, which yields: $T = (1/k)\log(R/r)$. Then, we have the profile for density behind the wave: $\rho(t,r) = (\alpha/\beta)\left[1 - exp\left(-\beta\left((1/k)\log(R/r) + t\right)\right)\right]$.

As the network behind the wave reassembles, it eventually reaches a critical density ρ_{cr} (we adopt this notation for the threshold density at which the contraction starts, ρ_{12}), which necessarily happens first at the outer boundary r = R of the droplet. The question is as follows: is the centripetal movement of the contractile outer boundary of the ring faster or slower than the rate at which the assembling network at the front of the ring reaches the critical density? As our calculations show, the movement of the ring due to contraction, which has velocity v = - kr, is identical to the rate at which the reassembling interconnected network's density reaches the critical density. If one plots the curve Rexp(-kt), which is the solution for the wave boundary motion due to contraction, against (r, t) where the reassembled network density reaches the critical density, one finds that the two are the same.

Width of the contractile ring: Suppose we have a ring with initial width δ_0 with inner boundary $R_1(t)$ and outer boundary $R_2(t)$, which at time t = 0 are located at R - δ_0 and R, respectively. Since both the inner and outer boundaries have velocities v = - kr, we can easily solve for their trajectories: $R_1(t)$ = (R - δ_0) exp (-kt), $R_2(t)$ = R exp (-kt). Then, the width of the ring is $\delta(t) = \delta_0$ exp (-kt), so the ring narrows over time.

Density of the contractile ring: The density profile within the peak (wave crest) can be calculated when the assembly rate is constant. The peak density changes due to advection and turnover, as well as from "collecting" the non-contractile network in front of the centripetally moving peak. The network that is being collected has just reached the critical density ρ_{cr}. Over a small time Δt, $\rho_{cr}\Delta x$ amount of the network is added to the peak. The distance the peak traveled is entirely determined by the motion of the leading edge of the wave crest. As the peak is very narrow, and the precise density distribution within it is not important, we spread out the collected network uniformly over the peak. Then, this contribution to the density within the peak becomes:

$$\left[k\left(R - \delta_0\right)\exp\left(-kt\right)\rho_{cr} / \delta_0 \exp\left(-kt\right)\right]\Delta t = \left[\left(R - \delta_0\right)/\delta_0\right]k\rho_{cr}\Delta t\,.$$

at each point within the peak, where $\delta(t)$ is the current width of the peak. Then, taking this additional contribution into account, the evolution equation for the density within the peak is given as:

$$\frac{\partial\rho}{\partial t} = \frac{\left(R - \delta_0\right)k\rho_{cr}}{\delta_0} + \alpha - \beta\rho - \nabla\cdot\left(u(r)\rho\right) = \frac{\left(R - \delta_0\right)k\rho_{cr}}{\delta_0} + \alpha + \left(2k - \beta\right)\rho + kr\frac{\partial\rho}{\partial r}\,.$$

The solution to this PDE is:

$$\rho(t,r) = \left[\frac{\alpha}{\beta - 2k} + \frac{\left(R - \delta_0\right)k\rho_{cr}}{\left(\beta - 2k\right)\delta_0}\right]\times\left[1 - e^{(2k-\beta)t}\right] + e^{(2k-\beta)t}P_0\left(re^{kt}\right),$$

assuming that the initial density $P_0 = \rho_{cr}$ within the peak which is at r = R at t = 0. We plot the resulting density peak of the contractile ring and its centripetal movement in Fig. S14. Note that all these calculations are based on the boundary condition stating that the non-contracting network does not respond to deformations of the contracting network nearby. Small changes in this boundary condition will generate some deformations, drift and rapid density changes of the non-contracting network in front of the ingressing ring. However, respective variation of the boundary condition will not change the model's solution qualitatively – the ring will still stay narrow as it ingresses; its density will be high; and its centripetal velocity will remain telescopic.

To plot the kymograph and velocity of the resulting waves, we examine the case when the interconnected network is slowly advected to the center (due to slow contraction at the center of the droplet) with a small velocity *w*. In 2D, the equation for the density of the interconnected network is then: $\partial\rho/\partial t = \alpha - \beta\rho - w\left(\partial\rho/\partial r + \rho/r\right)$. The solution of this equation is:

$$\rho(t,r) = (\alpha/\beta)\left[1-exp(-\beta t)\right] - \left(\alpha w/\beta^2 r\right)\left[1-exp(-\beta t)\right] + \left(\alpha w t/\beta r\right)exp(-\beta t) +$$

$$\frac{r-wt}{r}exp(-\beta t)\,\rho_0(r-wt)$$

where $\rho_0(r) = (\alpha/\beta)\left[1-\left(1-\left(\beta\rho_{cr}/\alpha\right)\right)(r/R)^{-\beta/k}\right]$.

The slow advection of the interconnected network impacts the width of the contractile ring and the rate at which the front boundary of the next contractile wave moves inward. It is intuitive that the inner boundary of the contractile wave $R_1(t)$ must move faster than $u = -kR_1$, because as the regrown interconnected network slowly flows inward, its density should cross the critical density at least as fast as $u = -kR_1$ (just due to assembly), plus *w*. Moreover, we expect the speed of the ring's inner boundary to be higher than (kR_1+ *w*) in 2D due to the geometry. We plot the computed kymograph and velocity of the resulting waves in Fig. S14.

One quantitative feature of the observed waves that the contractile ring model predicts better than the main model is the shape of the wave front. The simulation results (Figs. S13, S14) predict that the wave crest is narrow and does not widen as it moves centripetally, as observed experimentally (Fig. S1). Lastly, both main and contractile ring models predict that the centripetal velocity of the peak is almost perfectly telescopic (the speed grows linearly with radial distance), which agrees with the data well (Fig. S1f). Note, however, that in the super-large droplets (Supplementary Video 6), the temporal coordination usually assumed in the contractile shell/ring-type model (i.e. the simultaneous onset of contractility at all points along the periphery) is not observed. In particular, the ingressing wavefront sometimes exhibits lobes (Supplementary Video 6), where different regions of the wavefront are out-of-phase. This argues against the contractile ring model, suggesting that the main model provides a more likely explanation of the data.

Note about fluid vs solid network

In the model, we assumed that the actomyosin network is a highly viscous fluid. This is well supported by multiple biophysical experiments that suggest that, on temporal scales longer than ten seconds, the actin networks behave as a fluid. The reason is that filaments' turnover and dynamic crosslinking dissipate all elastic stresses on scales of several seconds. Nevertheless, it is useful to consider the question: can a solid, elastic network explain our observations. The short answer is in quasi-1D, it can, in

2D – it cannot. Note that the network can be quasi-1D in higher dimensions, if it flows along one direction only, so the other perpendicular directions can be ignored. This is the case, for example, for a 2D cortical surface in a cylindrical geometry where the flow is directed along the cylinder's axis (as in [9]). However, the cortical network will become effectively 2D if its flow velocity depends nontrivially on both x- and y-coordinates.

In 1D, if a large segment of the network is pulled at its boundary, then this segment drifts without any deformations, regardless of whether the network is solid or fluid. Note, that the equations for a viscous fluid (assuming a certain class of network rheologies) predict a constant velocity in space, anywhere where the contractile stress is absent, which is exactly the same as for a solid network. Therefore, whether we assume fluid or solid rheology, in a large part of the space, the network's behavior will be the same in the quasi-1D model.

The situation is dramatically different in 2D or 3D. Let us focus on 2D. If the network is viscous, the viscous stress in the axisymmetric case depends on the velocity gradient (Eq. 11) for the rheology that we assumed. The centripetal drift can be stress-free for an indefinitely long time simply if the velocity is distributed as in Eq. 14 (of course, the density could increase inward, then).

If the network is elastic, however, in the axisymmetric case, let us consider a hollow disc (annulus) geometry between r_0 and R ($r_0 << R$) . Let us denote by $U\left(r\right)$ the radial displacement of the network. Then, according to elasticity theory, the radial and tangential strains are defined as $\varepsilon_{rr} = \frac{\partial U}{\partial r}, \varepsilon_{\theta\theta} = \frac{U}{r}$ (i). The mechanical equilibrium across the network requires that the stresses satisfy: $\frac{\partial \sigma_{rr}}{\partial r} + \frac{1}{r}\left(\sigma_{rr} - \sigma_{\theta\theta}\right) = 0$ (ii). The strain-stress relations are given by Hooke's Law:

$$\varepsilon_{rr} = \frac{1+\nu}{E}\left(\left(1-\nu\right)\sigma_{rr} - \nu\sigma_{\theta\theta}\right), \varepsilon_{\theta\theta} = \frac{1+\nu}{E}\left(\left(1-\nu\right)\sigma_{\theta\theta} - \nu\sigma_{rr}\right) \quad \text{(iii)}$$

where E is the Young modulus and ν is the Poisson ratio. Substituting (i) into (iii), and then the result into (ii), we arrive at the equation for the displacement: $\frac{d^2U}{dr^2} + \frac{1}{r}\frac{dU}{dr} - \frac{1}{r^2}U = 0$ (iv). This is the so-called Euler's equation, and it has the exact solution: $U = C_1 r + \frac{C_2}{r}$ (v) where C_1 and C_2 are constants. Respective formulas for the stresses are: $\sigma_{rr} = \frac{E}{1-\nu}C_1 - \frac{E}{1+\nu}C_2\frac{1}{r^2}, \sigma_{\theta\theta} = \frac{E}{1-\nu}C_1 + \frac{E}{1+\nu}C_2\frac{1}{r^2}$ (vi).

Let us now consider the following problem: we want to apply a contractile stress, p, to the inner boundary of the hollow disc, so that this boundary moves centripetally inward toward the central axis. Thus, $U\left(r_0\right) = -r_0$ (vii). We will use the free radial stress condition at the outer surface: $\sigma_{rr}\left(R\right) = 0$ (viii). Using (vii,viii), we can find constants C_1 and C_2. Substituting those into (v,vi) and using the condition $r_0 << R$, we can find the necessary contractile stress: $p \approx \frac{E}{1-\nu}$ and the centripetal displacement of the outer surface: $U\left(R\right) \approx \frac{2}{1-\nu}\left(\frac{r_0}{R}\right)r_0$.

The following conclusion can be made from these arguments: the contractile stress would have to be too great, on the order of the Young modulus of the solid elastic network, for even a minuscule (much smaller than the inner radius r_0) displacement of the outer surface. Thus, the centripetal movement of the 2D elastic solid network would be very ineffective. The centripetal drift of a multidimensional elastic network would thus require enormous contractile stresses. For a 2D network to contract effectively, it has to fluidize under stress. The network, of course, does not have to be a simple elasto-viscous medium to support the observed mechanics and transport in 2D; it can be a 'cable' network [14], or elasto-plastic one [15], but the point is that it should resist stretch but be easily compressed.

The effectively 1D cortical network undergoing retrograde flow observed in elongated cylindrical blebs investigated in [9] was found to be characterized by solid mechanics. This rheology benefits the hypothesized mechanism of cell propulsion through the extracellular matrix, in which a solid interconnected network assembles within the pores of the extracellular matrix allowing the cell to pull itself through the matrix. However, if the cell uses several protrusions in different direction, fluidizing the intracellular network becomes a must for the cell to move consistently; this is also essential at the cell rear. It seems that an optimal network mechanics would have a hybrid character – solid-like for extensile deformations and fluid-like for contractile deformations. Then, if the network is pulled at one end and is undergoing resulting 1D drift through a matrix or on a sticky substrate, the network behaves as a solid, maintaining its geometry and generating the necessary traction for locomotion. On the other hand, if the network must flow centripetally in 2D or 3D, then even small contractile stresses fluidize the network allowing it to contract. Note that fluidization due to the stress is sufficient for such mechanics, because the stress can simply result from internal forces (e.g., due to myosin), but the fluidization can also depend on the geometry of the system, i.e., being triggered by the convergence of the flow in 2D or 3D. To summarize, percolation and interconnectedness of the intracellular network is the common requirement for global cellular movements, while mechanical properties of the network (solid, fluid, or other rheologies) are probably adapting to specific geometry and mechanics of the environment.

Finally, note that we only posit that purely elastic networks, with a significant stiffness, are incompatible with our data. There are likely many cases, both *in vitro* and *in vivo*, when the networks are elasto-plastic, or even elastic with very small Young moduli, and such networks would be able to undergo very significant flows in 3D geometry.

Discrete stochastic model

The continuous model provides physical insight, yet some aspects of pulsatile contraction are easier to address with a discrete model. The reason is that when contraction is too strong, short-range instabilities in the network emerge. To illustrate this, let us consider the system of force balance and transport equations in 1D in the contractile regime, assuming for simplicity that the contractile stress and viscosity are proportional to the network density:

$$\frac{\partial}{\partial x}\left(\eta_0\rho\frac{\partial u}{\partial x}+\sigma_0\rho\right)=0,\frac{\partial\rho}{\partial t}=\bar{\alpha}-\beta\rho-\frac{\partial}{\partial x}(u\rho).$$

Using the same scaling as above, respective dimensionless equations are:

$\frac{\partial}{\partial x}\left(\rho\frac{\partial u}{\partial x}\right)+\left(\frac{\sigma_0}{\eta_0\beta}\right)\frac{\partial\rho}{\partial x}=0,\frac{\partial\rho}{\partial t}=1-\rho-\frac{\partial}{\partial x}(u\rho)$. Mechanical equilibrium of this system,

$\rho = 1, u = 0$, is destabilized if small perturbations of this equilibrium, $\rho = 1 + p, u = 0 + v$, starts to grow. Not far from the equilibrium, the linearized equations for the perturbations, $\frac{\partial^2 v}{\partial x^2} + k\frac{\partial p}{\partial x}, \frac{\partial p}{\partial t} = -p - \frac{\partial v}{\partial x}$, have the solution $v = v_0 e^{\lambda t} e^{iqx}$, $p = p_0 e^{\lambda t} e^{iqx}$, if $q^2\left(\lambda + 1 - k\right) = 0$. Thus, the perturbation growth rate λ is positive even at very short wavelengths ($q >> 1$) if the contraction rate k is too high. In such case, the short-range instabilities lead to numerical instabilities in the continuous model.

We therefore introduce a discrete stochastic model, in which instead of considering a continuous density, the network is described by a collection of points corresponding to material nodes of the network. The best way to think about these nodes is to assume that they are focal points of microscopic contractile actomyosin units. We will only consider the 1D non-dimensional model on the interval $0 < x < 1$, the left and right ends of which correspond to the center and periphery of the droplet, respectively. The kinetics of the model involve a combination of assembly and disassembly processes. Assembly is realized by introducing a node with a constant rate a at random locations. Specifically, on each small-time interval Δt, a node is introduced with probability $a \times \Delta t$. We choose Δt small enough to keep $a \times \Delta t << 1$; the node appears at location r which is a uniformly distributed random number. Disassembly occurs by having each existent node disappear with a constant rate b.

The nodes interact with their two nearest neighbors to the left and to the right. The leftmost node interacts with the left boundary as if the boundary is a stable permanent node. The rightmost node does not interact with the boundary (stress-free boundary). The nearest neighbor distances between the nodes correspond roughly to the inverted density in the continuous model. Thus, the density-dependent network properties in the continuous model are replaced by interaction rules that depend on the nearest neighbor distance as follows:

1. If the inter-node distance x (for each pair of the neighboring nodes) is smaller than the contractility threshold δ_{contr} ($x < \delta_{contr}$) (corresponding to the interconnected and contractile high density region, $\rho > \rho_{23}$) then there is a contraction event. In such event, the nodes converge with a constant speed equal to kx where k is a constant contraction rate (on each small-time interval Δt, $\Delta x = -kx\Delta t$).
2. If the inter-node distance x is between the contractility threshold δ_{contr} and the connectivity threshold $\delta_{connect}$ ($\delta_{contr} < x < \delta_{connect}$) (corresponding to the interconnected, but not contractile, medium density region, $\rho_{12} < \rho < \rho_{23}$) then the inter-node distance does not change.
3. If the inter-node distance x is above the connectivity threshold $\delta_{connect}$ ($x > \delta_{connect}$) (corresponding to the unconnected low density region, $\rho < \rho_{12}$), then the node pair does not interact.
4. At each time step, the node coordinates are $\{x_1, x_2, ..., x_{N-1}, x_N\}$, in ascending order. We find all inter-neighbor-node distances greater than $\delta_{connect}$; these distances separate clusters of nodes, such that inside each cluster all neighboring node pairs interact, while neighboring clusters do not interact with each other. After the neighboring distances between the nodes in the cluster are updated according to rules 1-2, the center-of-mass of the cluster is shifted so that it does

not move relative to the time moment before the interaction, which ensures frictionless telescopic actomyosin contraction of network segments with stress free boundary conditions.

5. Rule 4 works for all interacting clusters except the leftmost one. If the leftmost node of this leftmost cluster is closer to the left boundary than $\delta_{connect}$, then after the neighboring distances are changed, the absolute positions of the nodes are shifted so that the boundary (which is a permanent node 0 in the model) does not shift. If the leftmost node of this leftmost cluster is farther from the left boundary than $\delta_{connect}$, then we apply rule 4 for this cluster.

This discrete stochastic model is a close analogue of the continuous deterministic model. In both models, the local network behavior is separated into three distinct regimes: 1) no drift at low densities, in the unconnected regime, 2) drift without spatial convergence at medium densities, in the connected but non-contractile regime, and 3) drift with convergence at high densities, in the contractile regime. We found that in the discrete model we do not need to make the boundary of the interconnected network grow with a small constant rate to generate pulsatile contractions. The reason is that the global connectedness occurs when all nearest neighbor distances between the nodes are smaller than the threshold, which can be the case even when the innermost contracting cluster has a moving boundary, due to the discrete character of the model.

Discrete model shows how continuous contraction, irregular pulsatile (coarsening) contraction and local contractile asters emerge: Here we use the discrete model to demonstrate the influence of the interconnected density threshold on the character of the contractile behavior (Fig. S15). We illustrate the results of the discrete model by fixing the contraction rate k, the domain size (in the non-dimensional model, the spatial domain always has the domain length equal to unity), the assembly and disassembly rates (a and b, respectively), and the parameter δ_{contr} responsible for the threshold contractile density. In the simulations, we varied the parameter $\delta_{connect}$, responsible for the threshold density at which the network becomes interconnected. The simulations shown in Fig. S15a correspond to large values of the parameter $\delta_{connect}$. This case is equivalent to a very low interconnection threshold density, so even at low densities the network at the periphery (right) is connected to the center (left). In this case, a continuous steady contraction develops. Similar results are observed in the continuous model's simulations (Fig. 3b, Supplementary Video 13). Fig. S15b shows that as the interconnection threshold becomes closer to the contraction threshold, contractile pulses develop, starting near the periphery. When the density in the middle of the spatial domain reaches the interconnected threshold, the contraction rapidly moves the network inward, and then it takes a finite time to rebuild the density at the periphery. In this regime, which is similar to the periodic wavy contraction in the continuous model (Fig. 3c,d, Supplementary Video 13), each global contractile event starts with one or a few local contractions at the periphery, and after a characteristic random time, these contractions get connected to the continuously contracting central (left end) core of the network, the whole network globally converges to the center (left end), and the cycle repeats.

One significant drawback of the discrete model is that there is no true periodicity in such model, for a fundamental reason. When material nodes appear according to a uniform random distribution, the distances between them are distributed exponentially, so even when the average node density is low, there are always a few pairs of nodes with very small distances between them. Thus, the local contractions at random places *always* occur. These individual contractions are short ranged, but they accumulate over time, shifting the growing interconnected clusters randomly. Ultimately, global

contraction still develops over a characteristic time scale, but the contraction is not strictly periodic, because the time for bridging over the last unconnected gap in the 1D chain of nodes is variable. Nevertheless, the discrete model qualitatively reproduces the continuous steady contraction and the pulsatile global contractions.

Fig. S15c shows a simulation of the discrete model for the case when the connectivity threshold is even closer to the contractility threshold. As the two thresholds get closer together, the discrete model predicts coarsening behavior of the network: local contractions merge into larger aggregates, which eventually, at irregular random time intervals and locations, connect to the droplet's center (left end of the interval) and converge there. This predicted behavior resembles the observed contractile pattern with intermediate amounts of Capping Protein or when myosin action is strengthened by Calyculin (Fig. 4). Lastly, Fig. S15d shows a simulation of the discrete model in the case when the connectivity threshold is very close to the contractility threshold. In this case, the local contractions become autonomous and never get connected to the center of the droplet (left end). These contractions randomly emerge and disappear, with clusters occasionally fusing with each other, and closely correspond to the contractile local asters observed in samples containing high concentrations of Capping Protein (Fig. 4b). Physically, these asters originate from local contractile instabilities: as soon as there is a patch of contractile density, the contraction leaves gaps at both sides of the patch. These gaps are not filled with nascent network fast enough, and so the contractions appear at random places transiently creating 'asters'.

Possible alternative models and arguments against them

To reiterate the principal physical problem arising from our experimental observations: the actomyosin network exhibits global periodic contraction, but given that the network does not contract everywhere all the time – how does this contraction become global, if it is initiated by local contractile events? The model we proposed above is as follows: even when the contractile network rapidly retracts from the boundary in the beginning of the periodic cycle, the assembly is still, however slow, sufficient to leave a low-density but interconnected network behind the contracting dense network. Thus, when the network reassembles to the threshold contractile density at the periphery, the peripheral contraction does not become autonomous, retracting locally to the droplet's boundary. Instead, the network becomes mechanically interconnected throughout the whole volume, making the contraction global. We favor this model because of its conceptual simplicity and because the predictions it makes explain the data well. Another possible model that could explain contraction in droplets, but not in flat capillaries, is the contractile ring model, discussed above. Theoretically, there are other possible mechanisms that can interconnect local contractions and make the global contractions robust. Below, we consider such alternative possibilities and arguments against them.

Variant of the model with global interconnected network: One possibility is that there is not one but two interpenetrative networks – one is contractile, and another is a globally interconnected non-contractile network, with a low density, that always permeates the droplet. These networks could interact by friction and steric forces, as in theories of multiphase fluids [16]. The globally interconnected non-contractile network has mechanical properties of the so-called cable networks [14] – it can be compressed almost without resistance but has a very high resistance to stretching (it is basically a net made of ropes that can be easily coiled but cannot be stretched). Then, we expect a behavior identical to that predicted by our model. In fact, physically, the two models are very similar. Mathematically

though, introducing the second network has the disadvantage of an additional complexity, which we wanted to avoid considering lack of data to discriminate between the two models.

Model with significant friction at low network densities: Another option for keeping the contraction global is to slow down the retraction of the network from the low-density region in the middle into two adjacent high-density contractile centers, to allow the density in the low-density region to grow faster than the outflow. In principle, this could interconnect the local contractions throughout the whole volume. The simplest mathematical way to implement this idea is to add the Darcy friction between the network and the solute in the force balance equation (in 1D): $\frac{\partial}{\partial x}\left(\eta\frac{\partial u}{\partial x}\right)+\frac{\partial \sigma_{contr}}{\partial x}=\zeta u$. Note, that the added Darcy friction term appears on the right-hand-side. Such a term could also come from frictional interaction with the membrane/substrate in cortical networks. In the model that we explored, the friction coefficient, viscosity and contractile stress are all functions of density:

$$\eta(\rho)=\begin{cases}\eta_0, & \rho<\rho_{12}\\ \eta_1, & \rho>\rho_{12}\end{cases}, \sigma_{contr}(\rho)=\begin{cases}0, & \rho<\rho_{23}\\ \sigma_1, & \rho>\rho_{23}\end{cases}, \zeta(\rho)=\begin{cases}\zeta_0, & \rho<\rho_{12}\\ \zeta_1, & \rho>\rho_{12}\end{cases}.$$

Here $\eta_0 << \eta_1, \zeta_0 >> \zeta_1$. In other words, the network is interconnected, viscous and non-contractile for intermediate densities, between ρ_{12} and ρ_{23}, contractile for greater densities, above ρ_{23}, and barely connected but experiencing great resistance from the solute at low densities, below ρ_{12}.
Simulations of this model showed that in small droplets there are steady distributions of density and velocity evolving, while for larger droplets, periodic waves develop (data not shown). The model works because in small droplets the absolute values of the velocity are smaller, and friction term is negligible; the network everywhere is interconnected and contracting. In large droplet, even though the new contraction starts at the periphery, the high friction at low densities prevents the contraction from depleting the low-density regions so that the reassembling network there can mechanically connects the contractile regions fast enough to make the contraction global. The problem with this model is that it is very hard to justify why the network friction would be larger at low network densities.

Mechanosensitive attachment to the boundary: Several models of the actin-adhesion clutch, supported by some experimental data, predict oscillatory periodic retrograde flow of the actin network in protrusive cell appendages [17]. The models are based on the mechanosensitive property of the actin network's adhesion to the substrate: the detachment rate is a rapidly increasing function of the pulling force. The model works as follows: there is a constant myosin-powered pulling from the rear of the protrusive cell appendage resisted initially by many firm adhesions. All adhesions are transient, and as several adhesions detach, the total myosin force per remaining adhesion increases, breaking more adhesions, and so on. As a result, an avalanche of breaking adhesions creates the so-called slipping state with rapid retrograde actin flow. Then, however, adhesions start to reattach, slowing the flow. The more the flow slows down, the smaller the force per adhesion, the more adhesions attach, eventually switching the system into the so-called gripping state, and the cycle starts again. It is possible, in principle, that such oscillations would emerge due to mechanosensitive adhesion between the network in the droplet and the droplet's boundary. The period of such oscillations would also be on the order of the network turnover time, simply because this is the characteristic time required to rebuild the retracted network, which could be the limiting step for the adhesive cycle. However, if this was the case, then the force of adhesion would be of the same order of magnitude or greater than the centering

hydrodynamic force [3], and we would see pulsatile movements of the centered aggregate around the droplet. This is not the case, and so this model is unlikely.

Diffusion-based models: A simple possible explanation for the waves would be the following: the advection process brings the actomyosin network to the center, then the network's elements must disassemble, *diffuse to the periphery* and reassemble there for the new contraction event to start. It could be that the time to diffuse to the periphery is the limiting step determining the wave period. There are two arguments against this scenario: 1) characteristic diffusion coefficient for many cytoskeletal subunits (actin oligomers, crosslinking proteins etc) is $D \sim 1\ \mu m^2 / s$. The characteristic diffusion time across the droplet then is $\sim R^2 / D \sim (100\mu m)^2 / 1\mu m^2 / s \sim 10^4 s$, which is two orders of magnitude longer than the observed period of ~ 100 *s*. It is thus likely that the recycling of the cytoskeleton is local rather than global in the system. Indeed, actin recycling are normally buffered by complex biochemical pathways keeping most of the diffusing actin in non-polymerizable form, which makes the network turnover local, while keeping the transport global even on centimeter scale, as is evident from the experiments with the super-large droplets (Supplementary Video 6). 2) The wave period would increase as square of the droplet's radius, $\sim R^2 / D$ according to this model, which is not the case. This said, global diffusion of cytoskeletal molecules may have some impact on the contractile behavior, because we do see evidence for gradual reduction in network assembly in the periphery of larger droplets which manifests itself in a gradual decrease in the intensity of consecutive wave fronts. This appears to be accompanied by an accumulation of filamentous actin around the contraction center, indicating that eventually disassembly and/or transport become limiting.

The centrifugal fluid flow could potentially become a dominant mode of actin subunit transport and explain actin delivery to the periphery. To explain the observed wave period, the centrifugal velocity of the solute must be $\sim R / T \sim 300\mu m / 100 s \sim 3\mu m / s$. While such flow is not out of question, our observations of tracer beads (Fig. S4) show that the beads move centrifugally only locally, in the vicinity of centripetally moving wave crests, and so it is unlikely that there is a global centrifugal fluid flow.

There is also a more sophisticated possibility: there are many examples of periodic waves in mathematical biology models [18]. Such waves emerge when spatial diffusion is added to complex temporal dynamics that have either oscillatory or excitable, or, in general, multi-equilibrium behavior. Note that several models of actin waves on cells adhering to surfaces are based on these mathematical concepts [19]. In these cases, periodic modulation of network activity is generated by biochemical modulation of components of the actin machinery. There are two arguments against this type of model for the contractile waves: 1) There is no indication for the temporal, global complex oscillatory, excitable or multi-equilibrium behavior in the droplets (usually, complex interactions with either NPFs, or Rho GTPases, and/or adhesive complexes on the solid surface are necessary for such dynamics). Moreover, our results in droplets in which the contraction center is localized asymmetrically which show both continuous and periodic contraction further argue against the presence of global oscillatory changes in the system. 2) The wavelength in such models is $\sim \sqrt{DT}$, where *D* is the characteristic diffusion coefficient, and *T* is the characteristic time scale. However, $T \sim 100\ s$ and $D \sim 1\ \mu m^2 / s$, and so $\sqrt{DT} \sim 10\mu m$ (observed in adhering cell cortex), which is orders of magnitude smaller than what is observed in our system.

Treadmilling polar filament array model: Lastly, waves were predicted in a *1D mix of treadmilling actin filaments and myosin motors* [20] and observed in vitro [21]. Those are based on an intricate polarity sorting

of the filaments and positive feedback between aggregation of the myosin clusters to the treadmilling actin plus ends and focusing of the plus ends in space. The characteristic length scale in this phenomenon is the filament's length, thus such phenomenon is highly unlikely on the scale of tens and hundreds of microns.

Interpretation of the beads' tracking experiments

To summarize the results of the beads' tracking experiments (Fig. S4; Supplementary Video 7), we observe: a) many centripetally moving beads colocalize with the ingressing wave crests; b) smaller numbers of centripetally moving beads between the consecutive wave crests; c) centrifugally moving beads that colocalize with the ingressing wave crests, but never between the consecutive wave crests. Here is the explanation of how these observations support both the interconnectedness of the low-density network, and the existence of a centrifugal fluid flow. It is likely that some beads are trapped in smaller pores of the actin mesh and therefore drift with the network, while other beads float in the fluid cytosol. Thus, we posit that we observe two sub-populations of beads – one that drifts with the network, and another which drifts with and diffuses in the fluid permeating the network (Individual beads can, of course, switch between these two sub-populations).

The fluid fraction of the extract undergoes the so-called Darcy flow, in which a combination of the conservation of the volume fractions of fluid and network with the mechanical law, according to which the relative velocity of the fluid relative to the network is proportional to the hydrostatic pressure gradient, determines the fluid velocity. In our case, the fluid velocity distribution can be predicted qualitatively without explicitly solving Darcy equations, if one analyzes the physics of the dense, yet porous, contractile network of the wave crest periodically ingressing to the center of the droplet. If we assume for simplicity that the low density of the network between the center and wave crest is constant, the fluid between the center and wave crest cannot drift at all because of the conservation of the volume fractions of fluid and network, even though the low-density network slowly moves centripetally. This is because a hydrostatic pressure gradient is generated by the network centripetal movement pushing the fluid centrifugally relative to the network to keep the fluid static in the lab coordinate system. However, when the wave crest ingresses, the physics becomes more complex: as the network is dense in the wave crest, when the wave crest shifts inward, some fluid volume must shift from the space near the inner boundary of the wave crest to the space near its outer boundary. Thus, the fluid velocity inside the wave crest must be centrifugal. (This flow is generated by a higher-pressure gradient induced by the centripetal movement of the higher-density network of the wave crest.) The bottom line of this analysis is: the fluid fraction in the droplet is stationary between the wave crests and is centrifugal in the wave crests.

This allows the simple explanation of our three observations: in between wave crests, if a bead move centripetally, it is likely bound to the network, and because we observe such beads, this provides an indirect indication for the presence of a low-density network that moves centripetally between the wave crease and hence that the network is interconnected (Otherwise, the network fragments would diffuse non-directionally). Many beads in between wave crests float in the fluid, but they do not drift directionally, because the fluid flow there is negligible. In the wave crests, many beads are trapped in the high-density network and move centripetally, but some beads float in the fluid, and as the analysis above predicts, they drift centrifugally. This intermittent centrifugal flow could be a principal part of recycling of actin monomers and binding proteins to the periphery.

References:

1. Kruse, K., Joanny, J.-F.c., Julicher, F., Prost, J. & Sekimoto, K. Asters, vortices, and rotating spirals in active gels of polar filaments. *Physical Review Letters* **92**, 078101 (2004).
2. Malik-Garbi, M. *et al.* Scaling behaviour in steady-state contracting actomyosin networks. *Nature Physics* **15**, 509-516 (2019).
3. Ierushalmi, N. *et al.* Centering and symmetry breaking in confined contracting actomyosin networks. *eLife* **9**, e55368 (2020).
4. Recho, P., Putelat, T. & Truskinovsky, L. Contraction-driven cell motility. *Physical Review Letters* **111**, 108102 (2013).
5. Landau, L.D. & Lifshitz, E.M. *Fluid Mechanics: Landau and Lifshitz: Course of Theoretical Physics, Volume 6*, Vol. 6. (Elsevier, 2013).
6. Alvarado, J., Sheinman, M., Sharma, A., MacKintosh, F.C. & Koenderink, G.H. Force percolation of contractile active gels. *Soft Matter* **13**, 5624-5644 (2017).
7. Weichsel, J., Baczynski, K. & Schwarz, U.S. Unifying autocatalytic and zeroth-order branching models for growing actin networks. *Physical Review E* **87**, 040701 (2013).
8. Garcia, A.L. *Numerical methods for physics*, Vol. 423. (Prentice Hall Englewood Cliffs, NJ, 2000).
9. García-Arcos, J.M. *et al.* Advected percolation in the actomyosin cortex drives amoeboid cell motility. *bioArxiv* (2022).
10. Sakamoto, R. *et al.* Tug-of-war between actomyosin-driven antagonistic forces determines the positioning symmetry in cell-sized confinement. *Nature Communications* **11**, 1-13 (2020).
11. Oakes, P.W., Banerjee, S., Marchetti, M.C. & Gardel, M.L. Geometry regulates traction stresses in adherent cells. *Biophysical journal* **107**, 825-833 (2014).
12. Lieleg, O., Claessens, M.M.A.E., Luan, Y. & Bausch, A.R. Transient binding and dissipation in cross-linked actin networks. *Physical review letters* **101**, 108101 (2008).
13. Maxian, O., Peláez, R.P., Mogilner, A. & Donev, A. Simulations of dynamically cross-linked actin networks: morphology, rheology, and hydrodynamic interactions. *PLoS computational biology* **17**, e1009240 (2021).
14. Paul, R., Heil, P., Spatz, J.P. & Schwarz, U.S. Propagation of mechanical stress through the actin cytoskeleton toward focal adhesions: model and experiment. *Biophysical journal* **94**, 1470-1482 (2008).
15. D'Antonio, G., Macklin, P. & Preziosi, L. An agent-based model for elasto-plastic mechanical interactions between cells, basement membrane and extracellular matrix. *Mathematical biosciences and engineering: MBE* **10**, 75 (2013).
16. Cogan, N.G. & Guy, R.D. Multiphase flow models of biogels from crawling cells to bacterial biofilms. *HFSP journal* **4**, 11-25 (2010).
17. Chan, C.E. & Odde, D.J. Traction dynamics of filopodia on compliant substrates. *Science* **322**, 1687-1691 (2008).
18. Murray, J.D. *Mathematical biology II: spatial models and biomedical applications*, Vol. 3. (Springer New York, 2001).
19. Allard, J. & Mogilner, A. Traveling waves in actin dynamics and cell motility. *Current Opinion in Cell Biology* **25**, 107-115 (2013).
20. Oelz, D. & Mogilner, A. Actomyosin contraction, aggregation and traveling waves in a treadmilling actin array. *Physica D: Nonlinear Phenomena* **318**, 70-83 (2016).
21. Reymann, A.-C. *et al.* Actin network architecture can determine myosin motor activity. *Science* **336**, 1310-1314 (2012).

Supplementary Figures

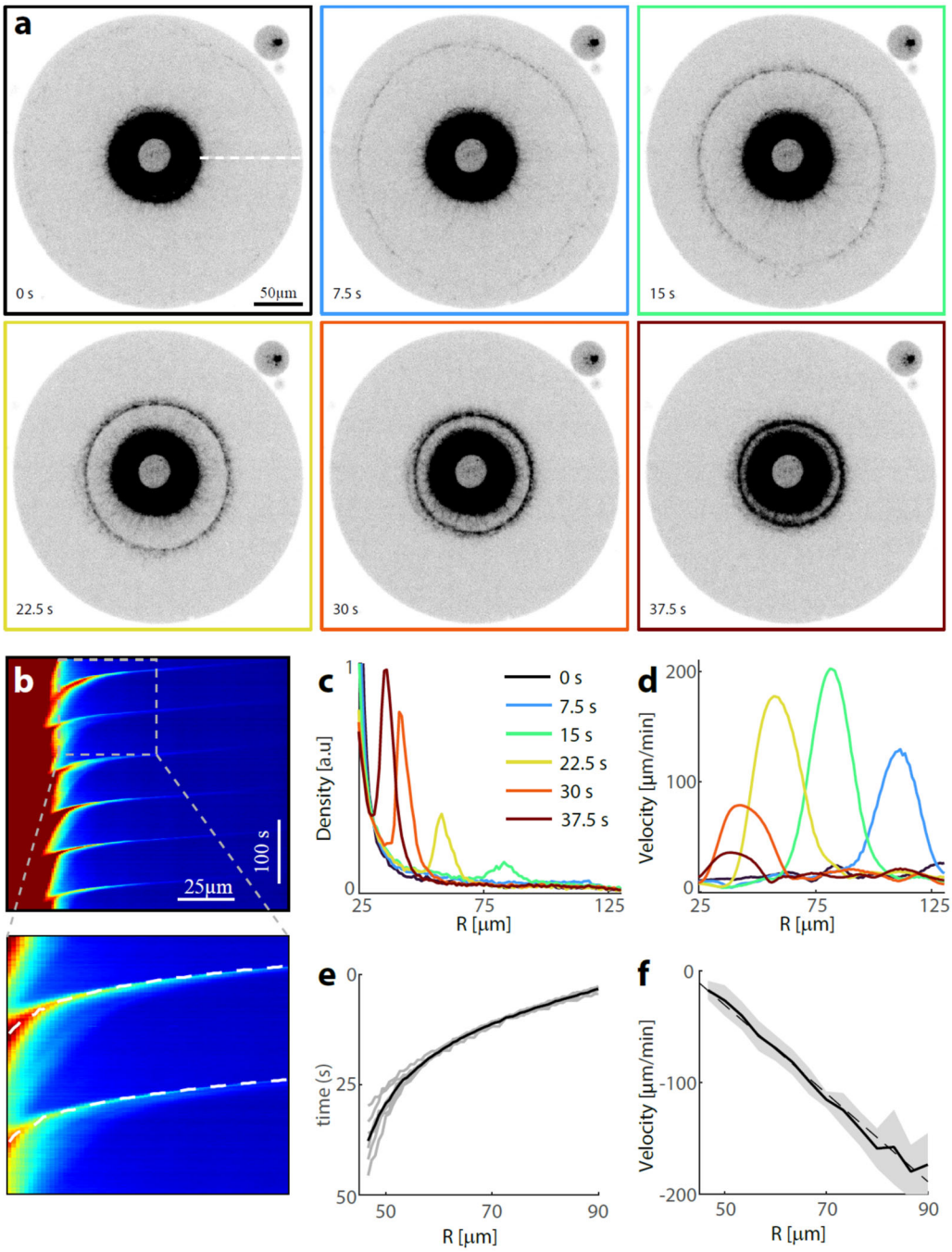

Figure S1. Wave front propagation in a droplet with periodic contraction. (a) Spinning disk confocal images (inverted contrast) of a water-in-oil droplet containing 98% *Xenopus* cell extract exhibiting periodic contraction (see Fig. 1b; Supplementary Video 3). Subsequent images show different stages of wave front propagation as a function of time. (b) Radial kymograph (top) and a zoomed view (bottom) showing the network density over time for the droplet shown in (a). The crest of the wave fronts is identified from the kymograph (bottom; dashed lines). (c,d) Radial cross-sections (along the dashed line in (a)) of the network density (c) and velocity (d) as a function of distance from the contraction center at

the different time points depicted in (a). (e) The time-dependent radial position of the wave crest is depicted for 6 consecutive wave fronts (grey lines), together with the mean wave crest position (black line). The wave crest was identified from the kymograph as in (b). (f) The inward radial velocity of the wave crest as a function of distance from the contraction center averaged over 6 consecutive wave fronts (mean-black line; std- shaded region), with a linear fit (dashed line) showing that the velocity of the wave crest is essentially telescopic.

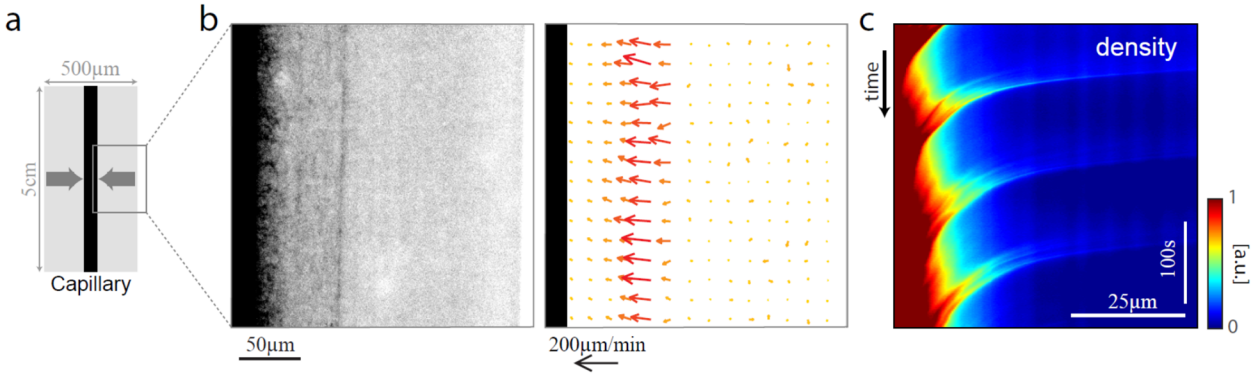

Figure S2. Periodic contraction in an elongated capillary. (a) Schematic illustration of contraction toward the center of a 5 cm long, 50x500 µm rectangular capillary. (b) Spinning disk confocal image (left; inverted contrast) and the corresponding velocity field (right) of a contracting wave front parallel to the wall of the capillary, that is moving inward (Supplementary Video 4). The capillary was filled with 80% *Xenopus* cell extract and supplemented with lifeact-GFP to visualize the actin network. (c) Kymograph showing the density variation along a horizontal cross-section of the capillary over time. The periodic wave fronts that contract toward the center of the capillary are evident.

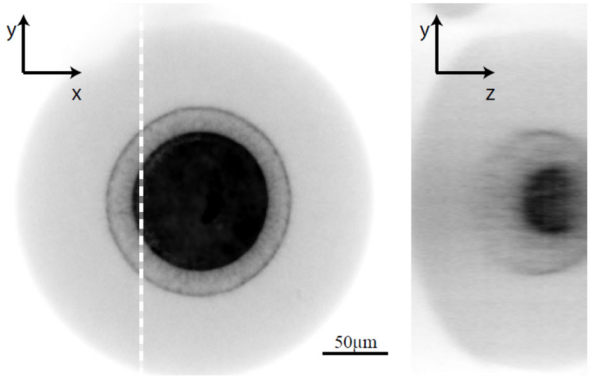

Figure S3. Periodic contraction in a spherical droplet. Spinning disk confocal images of a spherical water-in-oil droplet containing 95% *Xenopus* cell extract exhibiting periodic contraction (Supplementary Video 5). 2D cross-sections of the deconvolved 3D image stack (Methods) are depicted along the equatorial x-y plane (left), and along an orthogonal view parallel to the y-z plane (right; dashed line on left image). The wave front forms a concentric spherical shell.

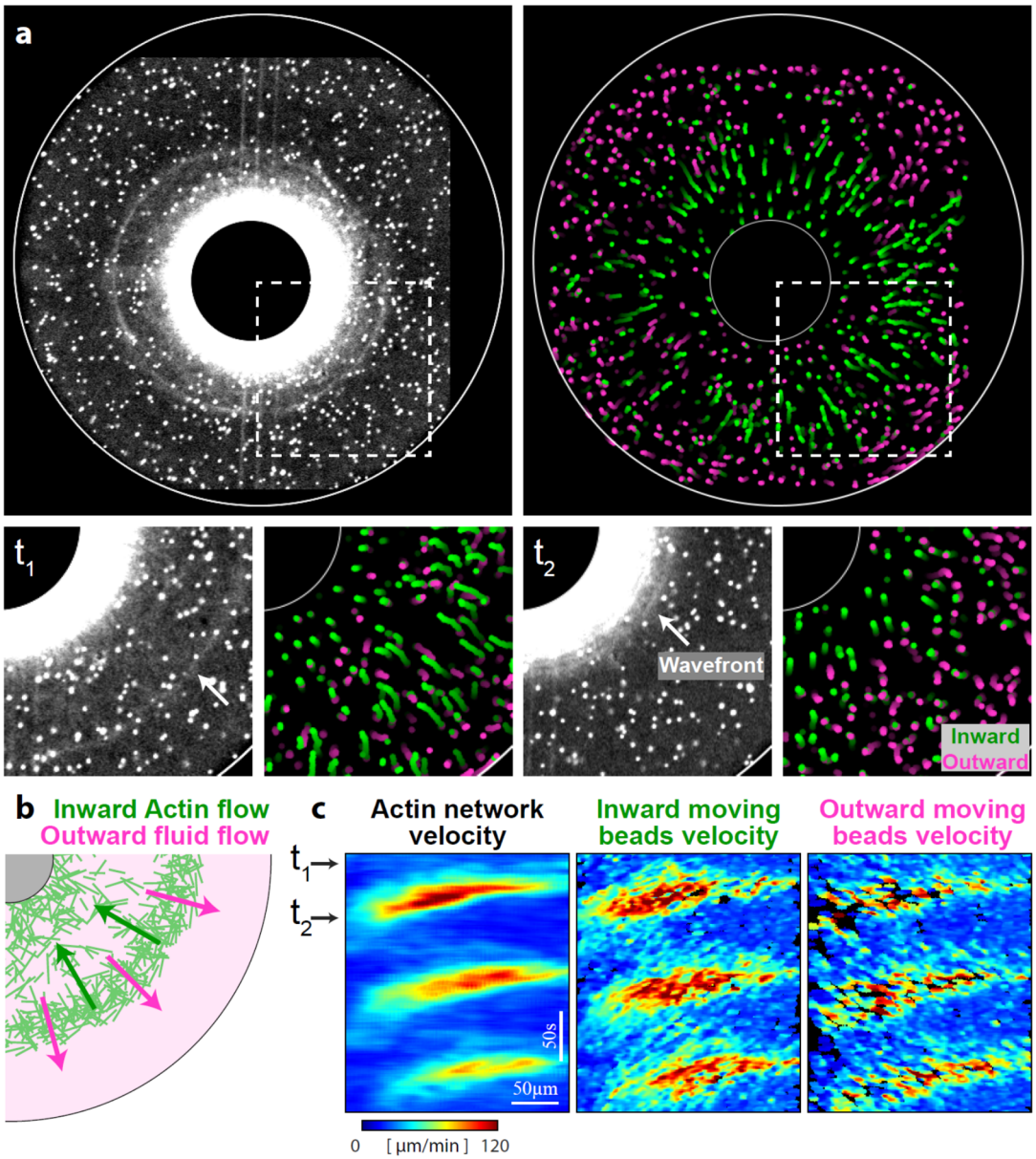

Figure S4. The movement of tracer beads in a droplet exhibiting periodic contraction. (a) Left: Spinning disc confocal image from a movie of a water-in-oil droplet containing 90% extract labeled with Lifeact-GFP, and supplemented with 0.5µm-diameter fluorescent beads (Supplementary Video 7). Right: An overlay of the trajectories of tracked beads over a time interval of 30s, classified according to their movement as inward-moving (green) or outward-moving (magenta; see Methods). Bottom: zoomed images depicting the actin network wave front and the pattern of bead movements at two consecutive time points (indicated by arrows in (c)). (b) Schematic illustration showing the inward movement of the contracting actin network together with the outward movement of the fluid. (c) Radial kymographs showing the periodic variation in the radial speed of the contracting actin network (left), the inward-moving beads (middle) and the outward moving beads (right) over time for the droplet shown in (a).

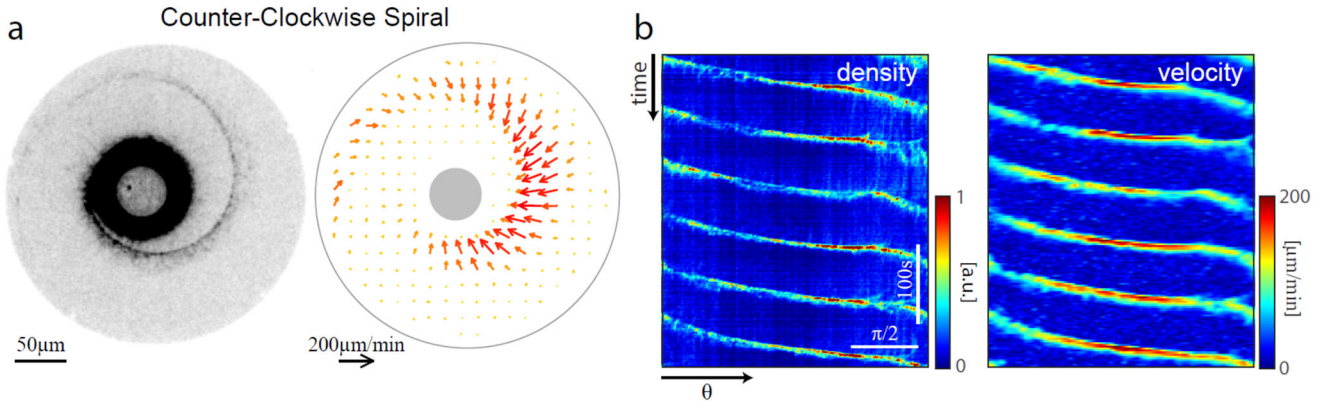

Figure S5. Example of periodic contraction in the form of a spiral rotating counter-clockwise (CCW). (a) Spinning disk confocal image (left) and the corresponding velocity field (right) of a water-in-oil droplet containing 98% *Xenopus* cell extract exhibiting periodic contraction in the form of a CCW spiral. (b) Kymographs showing the angular variation in the network density and velocity over time for the droplet shown in (a). The linearly-varying phase of the spiral wave front as a function of angle generates periodically-spaced parallel diagonal lines (as in Fig. 1e, but in the opposite orientation for a CCW spiral). Overall, out of 18 stable spirals observed, 10 rotated CW and 8 rotated CCW.

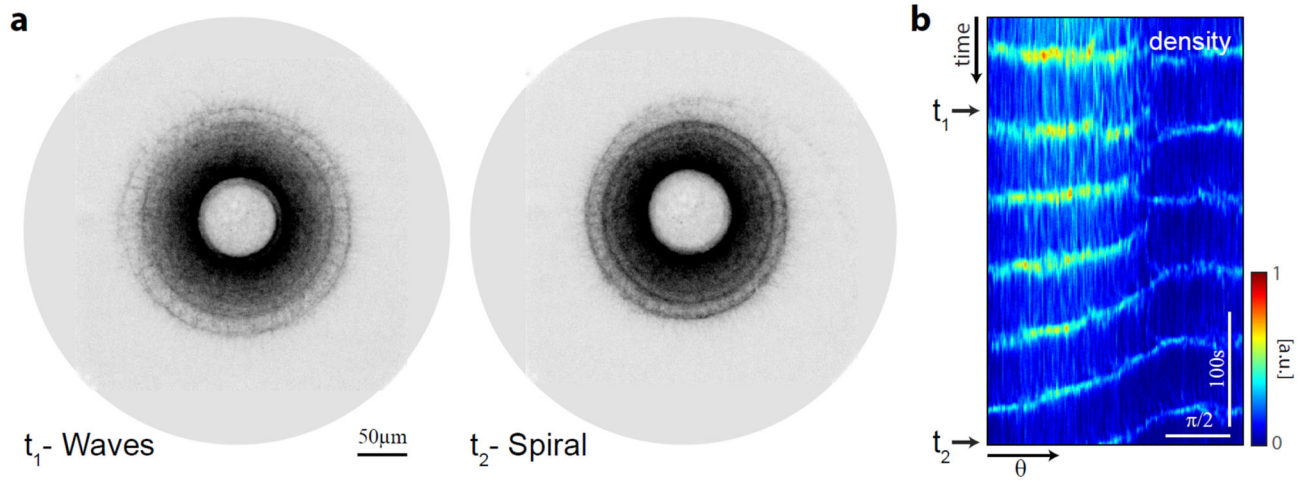

Figure S6. Transition from concentric waves to spiral. (a) Spinning disk confocal time-lapse images of a droplet containing 98% *Xenopus* cell extract that transitions from periodic contraction in the form of concentric waves (left) to a CW spiral (right). (b) Kymograph showing the angular variation in the network density over time for the droplet shown in (a). The transition from waves to spiral is apparent as the horizontal lines (waves) develop into diagonal lines (spiral) at a fixed angle. An angular asymmetry in the network density is present from the beginning of the movie.

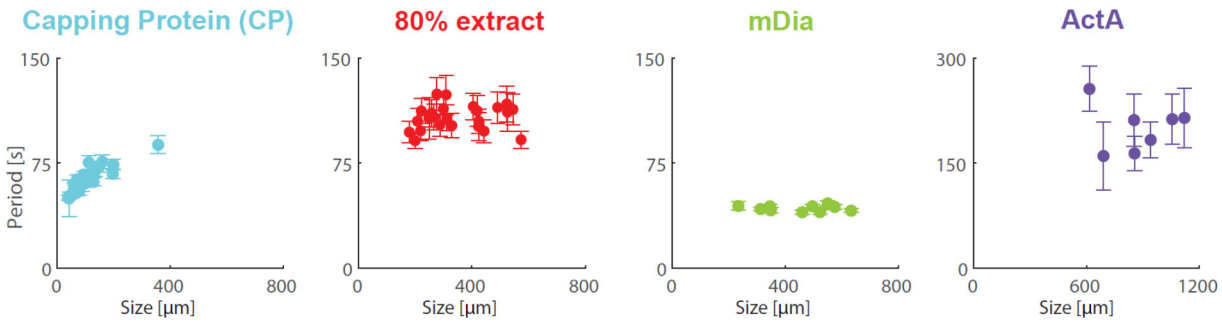

Figure S7. Periodicity of network contraction with actin associated proteins. Graphs depicting the wave period as a function of size for droplets above the transition length, which exhibit periodic contraction. Data is shown for populations of droplets containing 80% *Xenopus* cell extract supplemented with auxiliary proteins as indicated (1µM Capping Protein, none, 0.5µM mDia, or 1.5µM ActA). The error bars indicate the uncertainty in determining the period (see Methods). The period of the waves is largely independent of droplet size for unsupplemented extract or extract with added mDia or ActA, but appears to increase as a function of droplet size for extracts supplemented with Capping Protein.

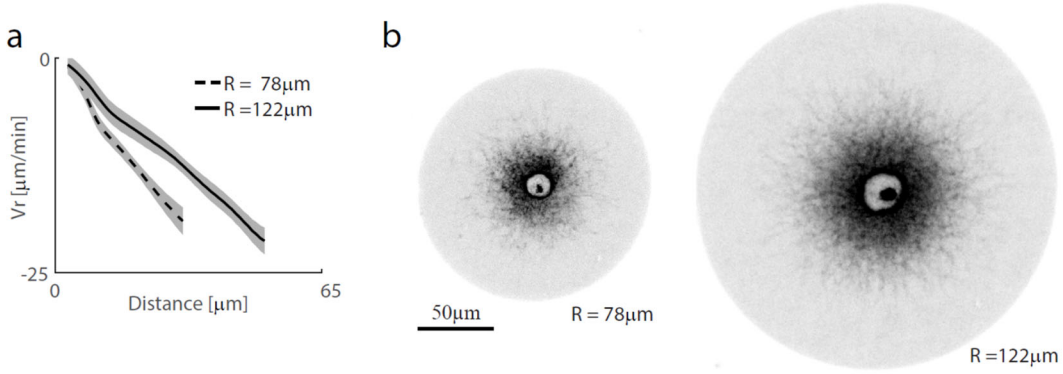

Figure S8. Contraction rate depends on droplet size. (a) Examples of the radial velocity profiles as a function of distance from the contraction center for two droplets of different sizes containing 80% *Xenopus* cell extract. The radial velocity increases nearly linearly in both droplets, which is a signature of homogenous density-independent contraction, but the contraction is slower in the larger droplet. (b) Spinning disk confocal images showing the actomyosin network distribution for the two droplets for which the radial velocity profiles are depicted in (a). The origin of the observed size-dependent contraction rate is not clear.

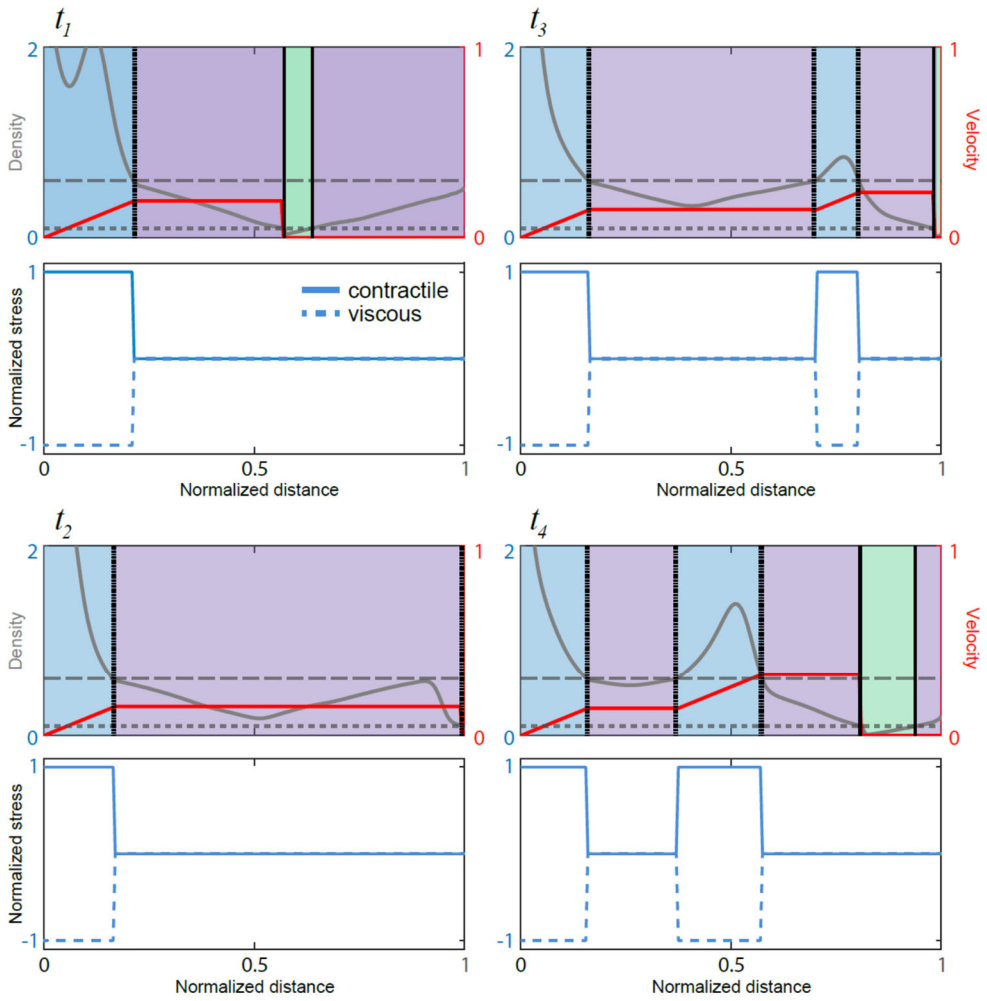

Figure S9. Numerical solution of the 1D model. A 1D model, identical to the 2D model in the main text, makes similar qualitative predictions. In particular, the model predicts a transition from continuous contraction to periodic contraction as the system size is increased. The results of a 1D simulation in the periodic regime are shown. Four consecutive snapshots of the wave cycle are depicted (top left, bottom left, top right, bottom right). The graphs in the upper panels show the simulated density (grey) and velocity (red) distributions as a function of distance from the contraction center (the results are shown for the non-dimensional variables). The dotted and dashed horizontal lines indicate the percolation and contraction density thresholds, respectively. The background colors indicate the local regions with unconnected (green), percolated (purple) and contractile (blue) network densities; the vertical dotted lines show the percolated-contractile region boundaries and vertical solid lines show the unconnected-percolation region boundaries. The lower panels depict the contractile and viscous stresses, which balance each other, corresponding to the density-velocity plot above them. The non-dimensional parameters used in the simulation are: $\rho_{23}=0.6$; $\rho_{12}=0.1$; $v_0=0.17$; $k=0.9$. The stresses are normalized by the constant contractile stress magnitude, σ_0.

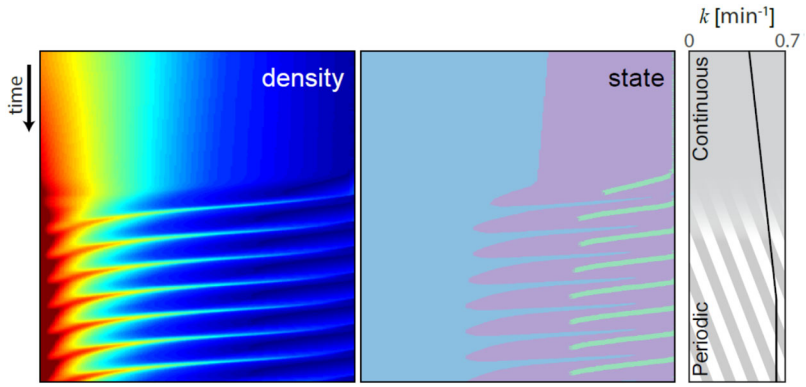

Figure S10. Modeling the transition from continuous contraction to waves in a system characterized by a contraction rate that increases over time. Kymographs showing the evolution of the network density (left) and the corresponding local network state (center) along a radial cross-section as a function of time, determined from 2D simulations of the model (Supplementary Video 14). The value of the contraction rate, *k*, was gradually increased over time from 0.45 to 0.65/min and then kept constant, as indicated in the graph on the right. The contraction dynamics transition from continuous contraction to periodic contraction. The simulation was run taking $\rho_{12} = 0.1$, $\rho_{23} = 0.6$, and $\alpha(\rho) = 0.1 + 0.9\left(1 - \exp\left(-\rho / 0.5\right)\right)$ and the following dimensional parameters: $v_0 = 30\ \mu\text{m/min}$, $\beta = 1/\text{min}$, $R = 170\ \mu\text{m}$, over a total time of 50 min. This simulation recapitulates the initiation of periodic contraction in a droplet that is close to the transition length where the contraction rate is observed to increase over time (Fig. 2i,j). The values of k and R were chosen to match the droplet shown in Fig. 2i.

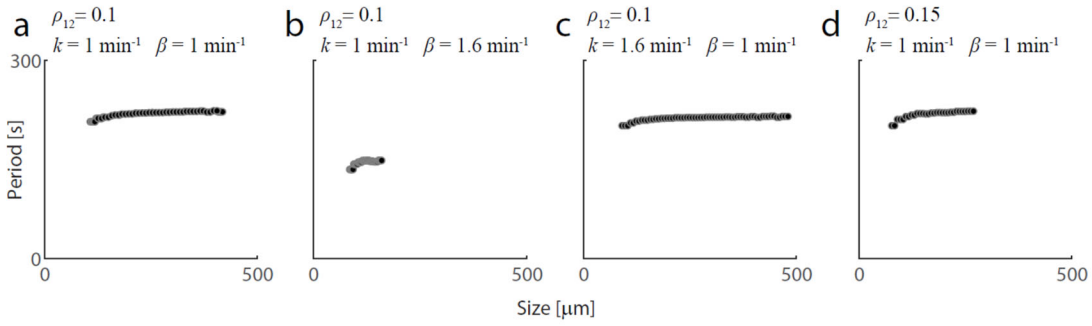

Figure S11. Predicted wave period as a function of system size. The period of waves in the 2D continuous model as a function of system size was determined from simulations for different values of the model parameters. The following parameters were used: $v_0 = 30\ \mu\text{m/min}$, $r_0 = 0.1R$, $\rho_{23} = 0.6$, $\alpha(\rho) = 0.1 + 0.9\left(1 - \exp\left(-\rho / 0.5\right)\right)$. The other parameters varied between the four simulations as indicated in each panel. The results show that the period is not sensitive to the system size, connectivity threshold or the contraction rate, and is inversely proportional to the disassembly rate.

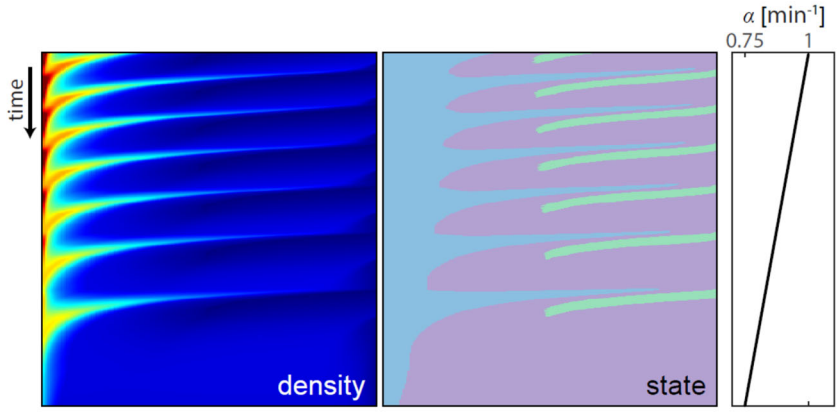

Figure S12. Modeling the increase in wave period with decreasing actin assembly. Kymographs showing the evolution of the network density (left) and the corresponding local network state (center) along a radial cross-section as a function of time, determined from 2D simulations of the model. The value of the maximal actin assembly rate α_∞ was linearly decreased over time from 1 to 0.75/min, as indicated in the graph on the right. The time interval between successive wave fronts increases until the contraction ceases. The simulation was run taking $\rho_{12} = 0.1$, $\rho_{23} = 0.6$, and $\alpha(\rho) = \alpha_\infty\left(0.1 + 0.9\left(1 - \exp\left(-\rho / 0.5\right)\right)\right)$ and the following dimensional parameters: $\mathrm{k} = 0.8\ /\mathrm{min}$, $v_0 = 30\ \mu\mathrm{m/min}$, $\beta = 1/\mathrm{min}$, $\mathrm{R} = 214\ \mu\mathrm{m}$, over a total time of 40 min. The results of this simulation recapitulate our experimental observations in droplets where phalloidin was added to the extract mix (Fig. 2g,h). Phalloidin binds actin filaments and inhibit their disassembly, effectively sequestering actin subunits and reducing actin assembly rates. The values of k and R in the simulation were chosen to match the droplet shown in Fig. 2g.

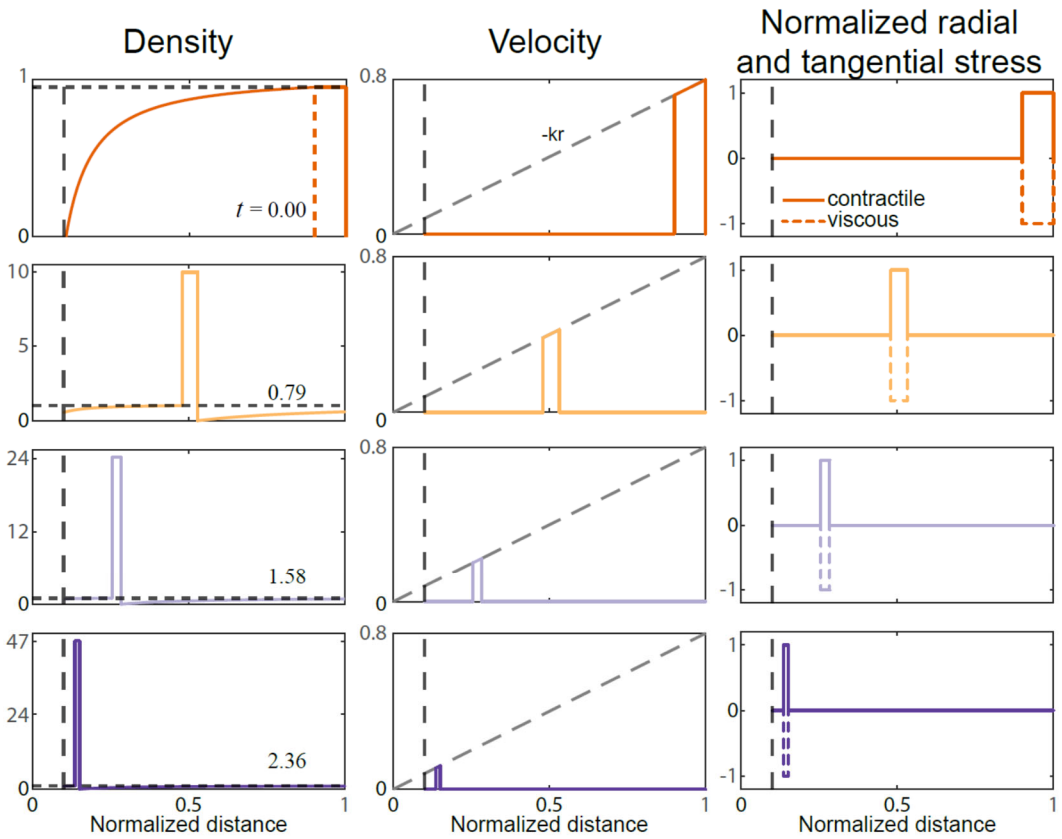

Figure S13. Solution of the 2D contractile ring model. Density profile (left), velocity distribution (middle), and radial/tangential stresses (right) are shown. The density plots show the assembling density in front of the contractile ring, the density within the contractile ring, and the density behind the contractile ring at consecutive time points, from the emergence of the contractile ring at the periphery to the moment before the ring reaches the boundary of the central zone. The density is shown in units of the contractility threshold; time is in units of inverted disassembly rate. Note that we assume that as the ring moves inward, it absorbs the assembling noncontractile network, which is then uniformly distributed within the ring. The density within the contractile ring follows the same reaction-advection dynamics otherwise. Note that the predicted velocity scales precisely linearly with the radial distance. The radial and tangential stresses are *the same* in this case, and both are normalized by σ_0, the contractile stress constant. Within the ring, the contractile and viscous stresses are exactly balanced. The non-dimensional parameters are: $r_0 = 0.1$; $R = 1$; initial size of contractile ring at edge, $\delta_0 = 0.1$; threshold for the connected to contractile density, $\rho_{cr} = 1$; assembly and disassembly rates, α=1.075 and β=1 , respectively; contractile rate, $k = 0.8$.

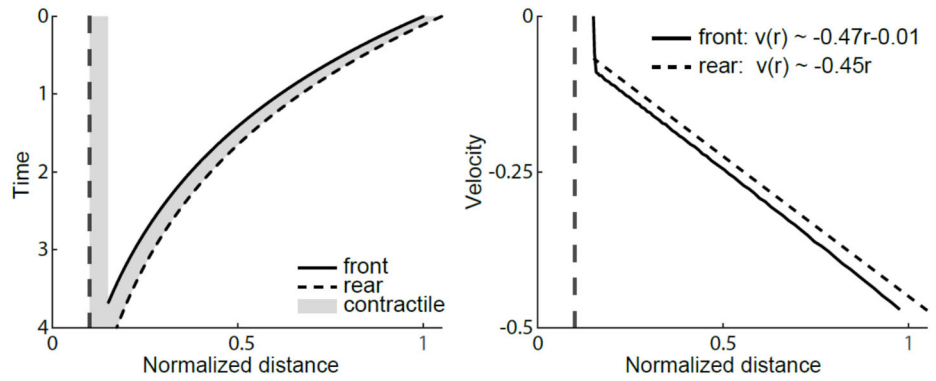

Figure S14. Kymograph of the 2D contractile ring. The numerical solutions of the 2D contractile ring model predict the dynamics of the wave front. Left: A kymograph of the contractile part of the density is shown (left, shaded in gray), also denoting the front and rear boundaries of the centripetal wave in the 2D contractile ring case. Right: The velocities of these front and rear boundaries of the centripetal wave are shown as functions of the radial distance, revealing telescopic character of the velocity. Note that the width of the contractile ring in this case is approximately constant. In the plots, the vertical dashed line is the boundary of the central contractile region. The radial distance is in the units of the droplet's radius; time is in the units of inverted disassembly rate; velocity is in the units of the product of the disassembly rate and droplet's radius. The non-dimensional parameters are: $r_0 = 0.1$; $R = 1$; initial size of contractile ring at edge, $\delta_0 = 0.05$; threshold for the connected to contractile density, $\rho_{cr} = 0.95$; assembly and disassembly rates, $\alpha = 1, \beta = 1$, respectively; contractile rate, $k = 0.45$; centripetal flow rate of the interconnected network between the exclusion zone and contractile ring, $w = 0.004$.

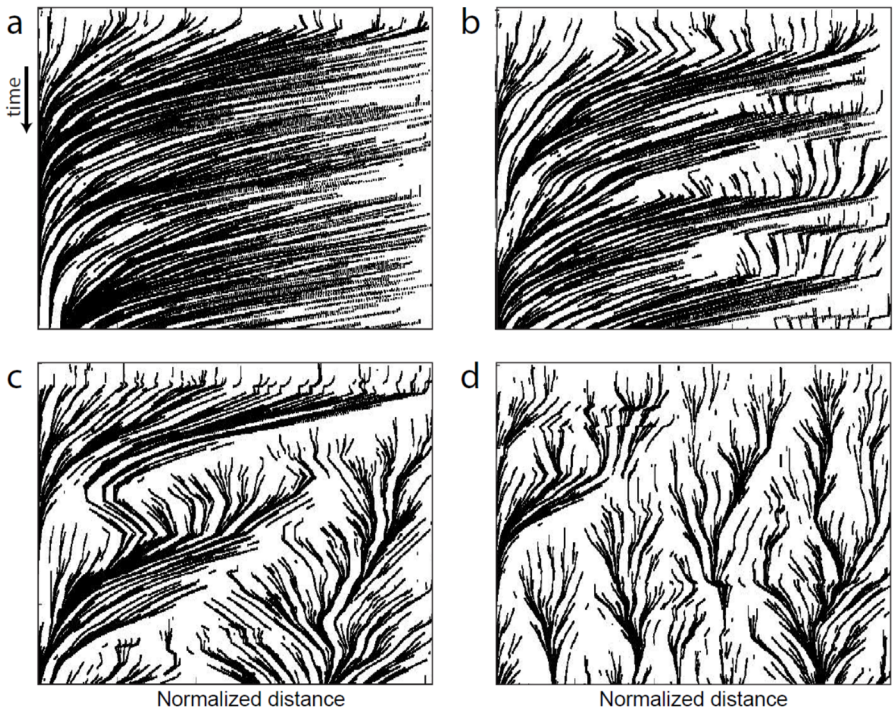

Figure S15. Different contractile behaviors obtained from simulations of a discrete agent-based model for different parameter values. The time evolution of the network was simulated using a discrete 1D model for different values of the connectivity threshold, $\delta_{connect}$ (see SI). Kymographs showing the location of network elements over time depict the different dynamic behaviors obtained including: (a) continuous contraction, $\delta_{connect} = 0.14$; (b) contraction waves, $\delta_{connect} = 0.08$; (c) irregular contraction, $\delta_{connect} = 0.06$, or (d) local cluster formation, $\delta_{connect} = 0.04$. All other non-dimensional model parameters were kept fixed for all simulations: contraction rate $k = 0.2$, domain size $L = 1$, assembly and disassembly rates $a = 10/$ unit time, and $b = 0.1/$ unit time, respectively (so on average there are 100 material points with an average distance of 0.01, and a turnover time equal to 10 time units), and contractility threshold $\delta_{contr} = 0.02$. The connectivity threshold, $\delta_{connect}$, was changed between simulations as indicated, and each simulation was run for a total time equal to 80 time units.